PL-TR-94-2288

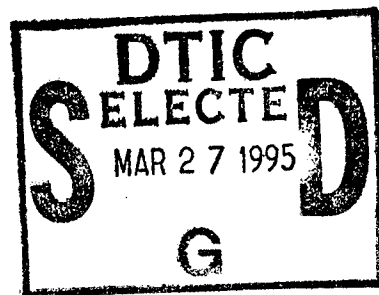# ADVANCED WAVEFORM RESEARCH METHODS FOR GERESS RECORDINGS

MONITORING NUCLEAR TEST SITES WITH GERESS

H. P. Harjes
M. Jost
J. Schweitzer
G. Bokelmann

Ruhr University - Bochum
D-44780 Bochum
FEDERAL REPUBLIC OF GERMANY

DTIC
SELECTED
MAR 2 7 1995
G

15 June 1994

Scientific Report No. 1

Approved for public release; distribution unlimited

PHILLIPS LABORATORY
Directorate of Geophysics
AIR FORCE MATERIEL COMMAND
HANSCOM AIR FORCE BASE, MA 01731-3010

19950323 049

SPONSORED BY
Advanced Research Projects Agency (DoD)
Nuclear Monitoring Research Office
ARPA ORDER No. A128

MONITORED BY
Phillips Laboratory
GRANT No. MDA 972-93-1-0022

REPORT DOCUMENTATION PAGE

Form Approved
OMB No. 0704-0188

Public reporting burden for this collection of information is estimated to average 1 hour per response, including the time for reviewing instructions, searching existing data sources, gathering and maintaining the data needed, and completing and reviewing the collection of information. Send comments regarding this burden estimate or any other aspect of this collection of information, including suggestions for reducing this burden, to Washington Headquarters Services, Directorate for Information Operations and Reports, 1215 Jefferson Davis Highway, Suite 1204, Arlington, VA 22202-4302, and to the Office of Management and Budget, Paperwork Reduction Project (0704-0188), Washington, DC 20503.

1. AGENCY USE ONLY (Leave blank)	2. REPORT DATE 15 June 1994	3. REPORT TYPE AND DATES COVERED Scientific Report No. 1

4. TITLE AND SUBTITLE
Advanced Waveform Research Methods for GERESS Recordings
Monitoring Nuclear Test Sites With GERESS

5. FUNDING NUMBERS
Grant MDA 972-93-1-0022
Proj NM93
TA GM
WU 88

6. AUTHOR(S)
H. P. Harjes   J. Schweitzer
M. Jost   G. Bokelmann

7. PERFORMING ORGANIZATION NAME(S) AND ADDRESS(ES)
Ruhr University – Bochum
D-44780 Bochum
FEDERAL REPUBLIC OF GERMANY

8. PERFORMING ORGANIZATION REPORT NUMBER

9. SPONSORING / MONITORING AGENCY NAME(S) AND ADDRESS(ES)
Phillips Laboratory
29 Randolph Road
Hanscom AFB, MA 01731-3010

Advanced Research Projects Agency
3701 North Fairfax Drive
Arlington, VA 22203-1714

Contract Manager: James Lewkowicz/GPEH

10. SPONSORING / MONITORING AGENCY REPORT NUMBER
PL-TR-94-2288

11. SUPPLEMENTARY NOTES

12a. DISTRIBUTION / AVAILABILITY STATEMENT

Approved for public release; distribution unlimited

12b. DISTRIBUTION CODE

13. ABSTRACT (Maximum 200 words)

This report summarizes research activities with GERESS data carried out at the Institute of Geophysics in Bochum during the second semiannual period (December 1993 - May 1994) of the current grant. GERESS data are continuously transmitted from the array hub in Bavaria to Bochum and analyzed by an on-line processing system, based on RONAPP, to detect and locate seismic events in near real-time. The GERESS data centre in Bochum continued to be responsible for maintenance of the array. The average uptime which includes the Bochum data centre has increased to 99.65 % during the first 5 months of 1994. For comparison, GERESS uptimes were 97.2 % in 1993, 96.9 % in 1992, and 91.5 % in 1991.

In Bochum, extensive parameter data for 54 regional and teleseismic phases have been interactively reviewed each day on average. From December 1993 to May 1994, 20 regional events have been automatically located each day on average.

GERESS data have also been transmitted to NORSAR continuously. The GERESS data centre Bochum has aided the CSS to test the experimental GSETT-3 International Data Centre (IDC V0, since May 1993). Within this concept, GERESS served as an alpha-station and acted as a node to access beta-stations in Germany.

Two major research projects were finished and separated papers are included in this report. The first paper (Jost et al)

14. SUBJECT TERMS
Arrays   Regional Wave Propagation
Calibration   GERESS

15. NUMBER OF PAGES
102

16. PRICE CODE

17. SECURITY CLASSIFICATION OF REPORT	18. SECURITY CLASSIFICATION OF THIS PAGE	19. SECURITY CLASSIFICATION OF ABSTRACT	20. LIMITATION OF ABSTRACT
Unclassified	Unclassified	Unclassified	SAR

NSN 7540-01-280-5500

Standard Form 298 (Rev. 2-89)
Prescribed by ANSI Std. 739-18

summarizes the GERESS recordings of underground nuclear explosions. Path-specific detection thresholds at GERESS are derived for NTS, Tuamotu Archipelago, Kazakhstan, Novaya Zemlya, and Lop Nor. These empirical detection thresholds substantially deviate from those calculated from global amplitude-distance relations (i.e. Gutenberg-Richter). This case history again casts some doubts on theoretical network capability estimates unless these are based on careful station calibration.

The second paper (Bokelmann) uses three-component and conventional vertical-component array data from GERESS to separately measure polarization and slowness vectors. This data set allows to distinguish the effect of anisotropy from lateral heterogeneity. Apart from interesting geophysical conclusions about the origin of this anisotropy, the study has also implications on the combined use of directional data from arrays and three-component stations in a global monitoring network. As local anisotropy in the vicinity of the receivers influences P-wave polarization, there may result a systematic bias between slowness parameters, measured with arrays and directional data, derived from three-component stations.

TABLE OF CONTENTS

page

Accesion For		
NTIS CRA&I	☒	
DTIC TAB	☐	
Unannounced	☐	
Justification		
By		
Distribution /		
Availability Codes		
Dist	Avail and / or Special	
A-1		

1. GERESS STATUS REPORT

December 1993 - May 1994

Michael L. Jost

1.1 General

The German Experimental Seismic System (GERESS) has been operated by Ruhr-University Bochum. The GERESS array is located in southeastern Germany (Bavarian Forest) near the border to Austria and the Czech Republic. The array consists of 25 stations with vertical-component short-period Teledyne Geotech GS-13 instruments sampled at 40 Hz. Four of the sites include horizontal component instruments. At the key station of the array, GEC2 (48.84511 N, 13.70156 E, 1132 m), a STS-2 is sampled at 80 Hz (broad-band element). The geometry of the array is based on concentric rings providing an overall aperture of about 4 km (Harjes, 1990). GERESS was installed in 1990 and the number of recording elements increased gradually over that year. The array became fully operational in January 1991. Data from the array have been continuously transmitted to the NORSAR data center in Kjeller and to the Institute of Geophysics, Ruhr-University Bochum via 64-kbit lines.

This report summarizes the technical performance of GERESS and the Bochum data center, and continues similar descriptions given previously (Jost, 1991a; 1992a; 1993a,b). This summary is based on monthly status reports that are available upon request.

1.2 GERESS Data Center at Ruhr-University Bochum

The Institute of Geophysics of Ruhr-University Bochum has operated an experimental on-line processing system for GERESS data (Jost 1992b; Harjes et al., 1993). This system uses software developed at NORSAR data center (Mykkeltveit and Bungum, 1984; Fyen, 1987). The automatic analysis has worked very stable and results are available for all GERESS data in this reporting period.

The on-line processing consists of 3 steps: detection, fk-analysis, and location. The first stage of the on-line processing accesses data in 30 second segments and runs a STA/LTA detector. The detector presently recognizes an

onset if the STA/LTA ratio for a filtered trial-beam exceeds a given threshold ranging between 3.5-4.0. Since September 1993, horizontal beams have been included to improve on S-type detections. The next step of the on-line processing is the transformation of a filtered data segment at each onset time (derived from the detection time) into the frequency-wavenumber domain. As a result, the slowness and back-azimuth of the phase is determined. From the slowness information, seismic phases are identified. The final step of the on-line data processing is the location of events. The seismic phases as identified in the fk-analysis are associated to events in this step. From the arrival time difference of regional phases, the distance to the epicenter is determined from the Jeffreys - Bullen travel time tables for regional seismic phases. Together with a mean back-azimuth, the epicenter locations of local and regional events are determined. Correcting for outages, 20 events have been automatically located each day on average (Table 1-1). Figure 1-1 shows the automatic event locations for Dec. 1993 - May 1994. Local magnitudes automatically determined at Bochum (e. g. Jost, 1993b) appeared low by at least 0.5 magnitude units compared to values published by other European observatories. A new amplitude-distance curve has been implemented on March 1, 1994. A detailed description will be given elsewhere.

Alert messages for strong teleseismic and regional events have been automatically sent to NEIC (Golden, CO) and other interested institutions in near real-time. 44 times, a GERESS alert message for a teleseismic onset has been used in the NEIC alerts in the reporting period; and 19 times by the EMSC. For regional events, a fast earthquake information system (FEIS) has been developed (Schweitzer, Schulte-Theis, Jost) and operated at Bochum. Starting from a GERESS automatic detection above a certain threshold, the routine automatically accesses the detection logs of the German Regional Seismic Network (GRSN). Using all available detections from this network, the routine proceeds to calculate a new location which is subsequently e-mailed to interested institutions. The time difference between origin time and transmission of an alert message was 42 minutes for more than 84 % of all FEIS alerts (Jul 93 - Oct 93). The shortest time was 24 minutes, the longest 1 hour. This time delay was mainly determined by the availability of communication lines.

The specific project of re-locating regional events by a human analyst was limited to 1993. From January 1994, analysts have routinely reviewed regional first arrivals together with teleseismic events. For this reporting period, parameter data (onset time, amplitude, period, azimuth, and slowness) for 9783 phases (i.e., 54 phases per day) have been sent to NEIC (Golden, CO), ISC, EMSC, and other institutions.

GERESS is an open station and results of the on-line processing have been sent to interested institutions via e-mail (e.g. Bundesanstalt für Geowissenschaften und Rohstoffe (BGR), EMSC, Frankfurt University, Geoforschungszentrum Potsdam (GFZ), Gräfenberg Array, ING, KTB array, LDG, Leipzig University, Stuttgart University, NORSAR, Oklahoma Geol. Survey, ORFEUS, and seismological institutes in Austria, CZ, Hungary, Slovenija, Switzerland; YKA). In addition, the On-line Processing Display Manager (Jost,

1991b) has been upgraded several times to make the diverse local data-bases available for near real time information on parameter data (Fig. 1-2). The Data Request Manager (DRM) by Krake Inc. (under contract from BGR, Hannover) has been operated in trial mode. Its performance has remained insufficient and a frequently announced upgrade has been waited for. Eventually, the DRM should enable the transmission of data (GSE, SEED) and interface to the German Regional Network of Broad-Band Stations.

Table 1-1

Statistics on the GERESS Bochum On-line Processing for Dec 1993-May 1994

	number	number/day
detections	63608	349
f-k analyses	50531	278
locations	3690	20

1.3 GERESS Array Hub

The GERESS array has shown stable operation from Dec. 1993 - May 1994. Table 1-2 shows the uptime of the system including the Bochum data center (uptimes directly correspond to the data archived in Bochum). The average uptime was 98.9 %, i.e., the total outage amounts to 1 day 23 hours. The highest uptime (99.99 %) was observed in March 1994; the lowest uptime (95.3 %) occurred in Dec. 1993 due to the sluggish response of the German Telekom in replacing a data modem damaged by thunderstorm. Table 1-3 further specifies the causes of the observed outages. The technical status of GERESS is summarized in chronological order in Appendix 1-1. Results of a recent instrument calibration are given in Appendix 1-2.

Table 1-2

GERESS uptime Dec. 1993 - May 1994 (incl. Bochum data center)

Month	uptime %
Dec	95.30
Jan	99.95
Feb	99.96
Mar	99.99
Apr	99.96
May	98.42

Table 1-3

Causes of GERESS downtimes Dec. 1993 - May 1994 (incl. Bochum data center)
(The total downtime was 171922 sec = 1d 23h 45m 22 sec)

cause	downtime [sec]	downtime [%]
Bochum data acq. software	17075	9.9
Bochum data acq. software (maintenance)	0	0
Bochum data acq. workstation	5	0
Bochum CIM	0	0
Bochum power outage	41726	24.3
total outage Bochum	58806	34.2
Communication line	75685	44.0
HUB IAC crashes (1)	98	0.1
HUB thunderstorm damage	19774	11.5
HUB maintenance	3659	2.1
HUB power outage	13769	8.0
total outage HUB	37300	21.7
other causes	131	0.1

GERESS has used data acquisition equipment from Teledyne-Geotech (i.e. RDAS-200, IAC) which is no longer in production. GERESS is a prototype installation and inherent problems have remained (e.g., Golden et al, 1991). Due to the severity of these problems, we will continue to list them to remind the community of possible problems inherent in GERESS data.

- The RDAS-200 occasionally sends electronic noise instead of seismic data after power up or self-reset. This state can be cleared only by manual intervention (reset).

- If the 1pps timing-signal is bad (optical modems, fiber optic link), or the clock-board in the RDAS-200 deteriorates before completely failing, or after any self-reset, or after any power cycle, data can be desynchronized by one second or by less than a second (mostly 0.2 seconds). Only an array installation of RDAS-200's has the chance to detect this. Each day, a careful inspection of GERESS records has been performed to insure proper synchronization. After a desynchronization has been detected, one or several manual power cycles usually synchronizes the station.

- The RDAS-200 is very sensitive to spikes in input voltage (thunderstorms) causing outages or self-resets.

- The RDAS-200 occasionally sends data with corrupted time stamps in the future.

- Meteorological data are not available for GERESS.

- GERESS runs on DCF-77.

At Bochum data center, we have continued to keep GERESS operational to provide the community with useful data. We hope to gather sufficient spare parts to keep the current hardware running as long as practical. For general scientific purposes, this situation appears acceptable. But for the special requirements in a treaty situation, we recommend an upgrade of the present hardware to a more robust system.

1.4 Conclusion

GERESS is the most sensitive seismological station in Central Europe for regional events. The teleseismic detection threshold of GERESS ranges globally between m_b 4.0 - 4.5 (this report).

At the GERESS data center Bochum, the observatory routine has included data archival and automatic on-line analysis. From Dec. 1993 to May 1994, 20 regional events have been automatically located each day on average. The GERESS data center Bochum is the only German station that provides NEIC and interested institutions with alert messages (teleseismic and regional).

In Bochum, extensive parameter data for 54 regional and teleseismic phases have been interactively reviewed each day on average. Results of this re-analysis of GERESS data have been used by NEIC, ISC, EMSC, and other interested institutions. The Bochum data center is an open station similar to the German Regional Network of Broad-Band Stations (GRSN). In addition, Bochum serves as data center where various bulletins (e.g., alerts from NEIC, EMSC, NORSAR, SED, and ING; onset lists from GRSN, Austrian stations, Czech stations, and YKA; locations from NEIC (QED, PDE (weekly), PDE (monthly)), IDC (GSETT-3), IGN, IMS, LDG, and SED; fast CMT's from Harvard, USGS, and Tokyo University) are available for the interested user.

The GERESS data center Bochum has aided the CSS to test the experimental GSETT-3 International Data Center (IDC V0, since May 1993). Within this concept, GERESS served as α-station and acted as a node to access data from the GRSN, serving as β-stations.

The GERESS data center Bochum has been responsible for GERESS maintenance. The average GERESS uptime which includes the Bochum data center has increased to 99.65 % during the first 5 months of 1994. For comparison, GERESS uptimes were 97.2 % in 1993, 96.9 % in 1992, and 91.5 % in 1991. This again demonstrates the high level of reliability of the installation, its successful maintenance, and the high motivation of key personnel.

Acknowledgements

Literature

Fyen, J. (1987). Improvements and Modifications, Semiannual Technical Summary, 1 October 1986 - 31 March 1987, *NORSAR Sci. Rep. No. 2-86/87*, Kjeller, Norway.

Golden, P., E. T. Herrin, and C. Hayward (1991). Development of an intelligent seismic facility and preparation for participation in the conference on disarmament group of scientific experts technical test. Results of the GERESS verification test, *Quarterly Technical Report SMU-R-91-152*, Southern Methodist University, Dallas, Texas, 64 pp.

Harjes, H.-P. (1990). Design and siting of a new regional array in Central Europe, *Bull. Seism. Soc. Am.* **80**, 1801-1817.

Harjes, H.-P., M. L. Jost, J. Schweitzer, and N. Gestermann (1993). Automatic seismogram analysis at GERESS, *Computers & Geosciences* **19**, 157-166.

Jost, M. L. (1991a). GERESS status report January 1990 - March 1991, in *Advanced Waveform Research Methods for GERESS Recordings*, DARPA Annual Report No. AFOSR-90-0189, 28-37.

Jost, M. L. (1991b). The Bochum on-line processing display manager, in *Advanced Waveform Research Methods for GERESS Recordings*, DARPA Annual Report No. AFOSR-90-0189, 38-43. PL-TR-91-2134, ADA239199

Jost, M. L. (1992a). GERESS status report April 1991 - February 1992, in *Advanced Waveform Research Methods for GERESS Recordings*, DARPA Annual Report No. PL-TR-92-2142, 1-12. ADA253686

Jost, M. L. (1992b). Current status and results of the GERESS data center in Bochum, in *Proceedings of the GERESS Symposium Waldkirchen June 22-24, 1992*, 93-102.

Jost, M. L. (1993a). GERESS status report January 1992 - December 1992, in *Advanced Waveform Research Methods for GERESS Recordings*, ARPA Annual Report No. PL-TR-93-2172, 1-17. ADA270105

Jost, M. L. (1993b). GERESS status report January 1993 - November 1993, in *Advanced Waveform Research Methods for GERESS Recordings*, ARPA Semi-annual Report (submitted).

Mykkeltveit, S. and H. Bungum (1984). Processing of regional seismic events using data from small-aperture arrays, *Bull. Seism. Soc. Am.* **74**, 2313-2333.

Appendix 1-1: Chronological Status List GERESS

Dec. 1993:
- outage HUB (Telekom data modem damaged by thunderstorm)
- power outage HUB (power line damaged during storm)
- power outage on UPS university (fuse blown by short elsewhere)
- 2 min data gap possibly due to power outage and defective USV (HUB)
- Dec. 13 - 14, Dec. 27 - Jan 1, maintenance visits at HUB.
- data link GERESS - Kjeller and GERESS - Bochum switched from land-lines (German Telekom) to satellite (Spaceline Inc.).

Jan. 1994:
- 2 min data gap possibly due to power outage and defective USV (HUB)
- 2 thunderstorms at HUB (3 times 2 min outages array, station outages)

Feb. 1994:
- temporary malfunction of STS-2 broad-band instrument

Mar. 1994:
- 2 min data gaps due to power outage and defective USV (HUB)
- implementation of new amplitude-distance curve for magnitude calculation
- modification of system kernel on data acquisition workstation

Apr 1994:
- 2 min data gaps due to power outage and defective USV (HUB)
- defective preamplifier C2 (broad-band element)
- 5 thunderstorms at HUB (station outages)
- Apr. 10-14 maintenance visit at HUB.
- implementation of German 3. level seismotectonic names of IASPEI regionalization (Leydecker 1994)

May. 1994:
- 3 thunderstorms at HUB (array and station outages)
- power outage HUB (maintenance by electricity company)
- May 2-6 maintenance visit at HUB (preamplifier C2 exchanged, calibration problems fixed on B3, C7, D6, D7, D8, D9, replacement of defective USV)
- spontaneous desynchronization on D7
- temporary malfunction of STS-2 broad-band instrument
- new USV defective (manual intervention required after surge or extended power outage)

Appendix 1-2: GERESS Instrument Calibration

Each day, the GS-13's of GERESS are calibrated using a 1 Hz sinusoidal input voltage (GS-13 4500 mV) fed to the calibration coil.

cal. time	channel
3:00 - 3:00:50	A0, A-ring (verticals), C2-sz
3:00 - 3:01:00	D6
3:01 - 3:01:50	A2-sn
3:02 - 3:02:50	A2-se, B - ring
3:04 - 3:04:50	C1, C3
3:06 - 3:06:50	D1-sz, D2, D3
3:07 - 3:07:50	D1-sn, D4-sn, D7-sn
3:08 - 3:08:50	D1-se, D4-se, D7-se, C4, C5, C6, C7
3:10 - 3:10:50	D4-sz, D5
3:12 - 3:12:50	D7-sz, D8, D9

Calibration on May 26, 1994 (for D6 from May 8;   318273 cnts are expected)

| channel	cnt	deviation in %
GEA0_sz	317123	-0.361
GEA1_sz	319254	0.308
GEA2_sz	311215	-2.22
GEA3_sz	316905	-0.430
GEB1_sz	319442	0.367
GEB2_sz	316260	-0.632
GEB3_sz	380812	19.65
GEB4_sz	320425	0.676
GEB5_sz	308851	-2.96
GEC1_sz	314933	-1.05
GEC2_sz	312405	-1.84
GEC3_sz	315325	-0.926
GEC4_sz	311943	-1.99
GEC5_sz	312094	-1.94
GEC6_sz	315217	-0.960
GEC7_sz	309905	-2.63
GED1_sz	297258	-6.60
GED2_sz	324986	2.11
GED3_sz	318497	0.070
GED4_sz	300922	-5.45
GED6_sz	317980	-0.09
GED5_sz	312444	-1.83
GED7_sz	289007	-9.20
GED8_sz	316283	-0.625
GED9_sz	320454	0.685
GEA2_sn	318844	0.179
GEA2_se	315890	-0.749
GED1_sn	324707	2.02
GED1_se	314142	-1.30
GED4_sn	312861	-1.70
GED4_se	313429	-1.52
GED7_sn	309456	-2.77
GED7_se	308842	-2.96

Figure 1-1:

GERESS BOCHUM: AUTOMATIC LOCATIONS DEC. 1993 - MAY 1994
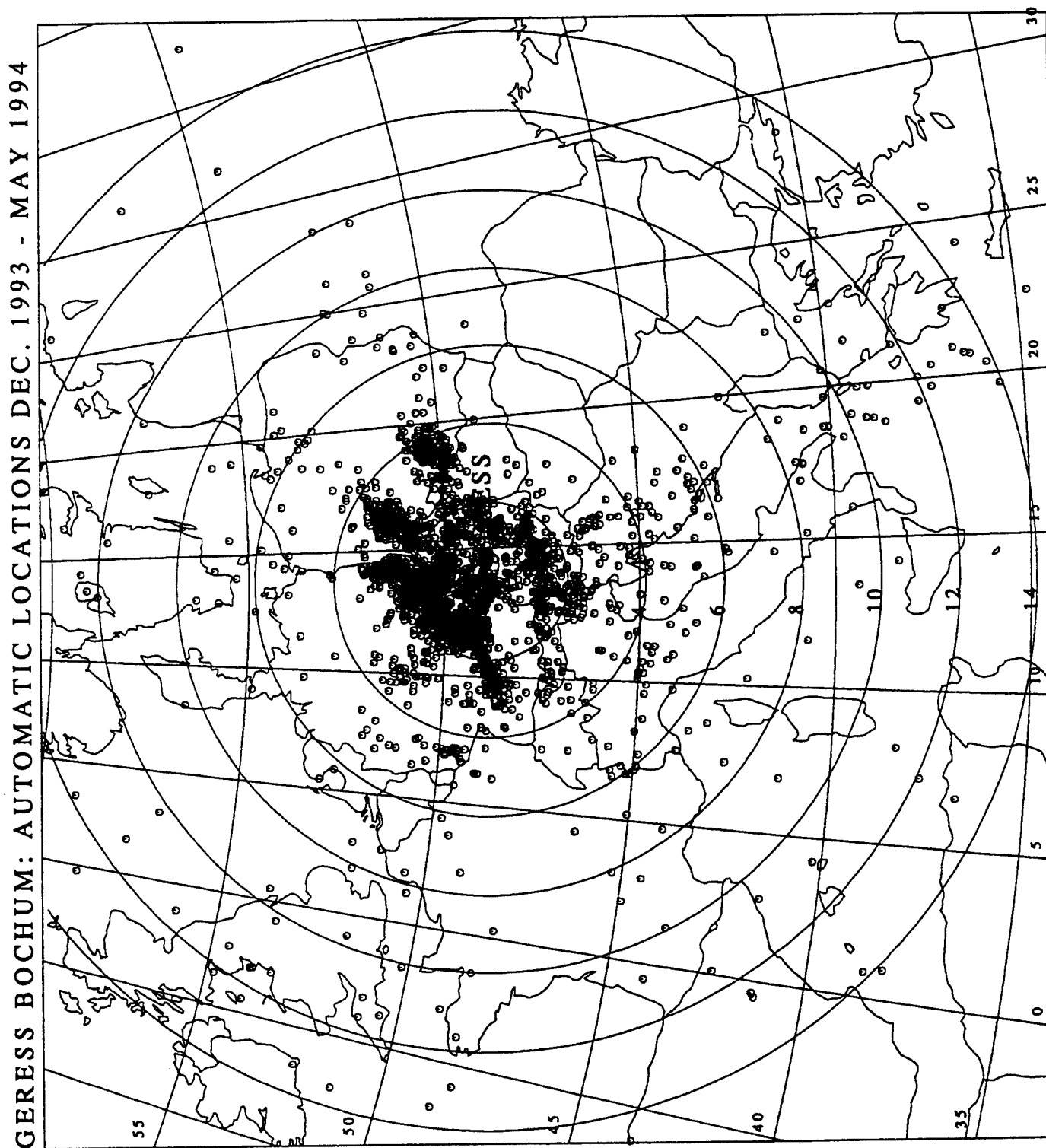
Figure 1-2: The basic menu of the On-line Processing Display Manager at the GERESS data center Bochum

```
******************************************************************
*                                                                *
*          WELCOME TO THE GERESS ARRAY DATA CENTER AT            *
*                  Ruhr-University Bochum                        *
*                                                                *
*            ON-LINE PROCESSING DISPLAY MANAGER                  *
*            (Version 3.4,  8. Jun 94; Dr. M. L. Jost)           *
*                                                                *
******************************************************************


+++++++++++++++++++++++++++++++++++++++++++++++++++++++++++++++++
+ Lists of the GERESS on-line processing (extended epi) can be +
+ sent daily to you. Please give us your e-mail address       +
+++++++++++++++++++++++++++++++++++++++++++++++++++++++++++++++++

TODAYs DATE: 94159

GERESS ##########################################################
Cmds: det   GERESS detections        deti  info on GERESS detector
      fk    GERESS f-k results       down  info on GERESS downtimes
      epi   GERESS unrev. locations  bull  GERESS automat. Bulletin
      loc   GERESS rev. locations
      tel   GERESS rev. teles. onsets  plot  TEKTRONIX plot module

ALERTS ##########################################################
      nau   NEIC auto. locations     fei   FEIS alerts
      nar   NEIC rew. auto. locations  sal   SED alerts
      ale   NEIC alerts              ing   ING alerts
      ems   EMSC alerts
      nor   NORSAR alerts

ONSETS ##########################################################
      grn   GRSN onsets              yka   YKA onsets
      aus   Austrian Net onsets      vra   VRAC onsets
                                     csd   KHC PRU onsets

BULLETINS #######################################################
      qed   QEDs from NEIC           ldr   LDG reg. bull. (France)
      pde   weekly  EDRs from NEIC   ldt   LDG tel. bull. (France)
      edr   monthly EDRs from NEIC   sed   SED bulletin (Switzerl)
      idc   GSETT-3 EIDC Bulletin    igr   IGN reg. bull. (Spain)
      ims   IMS Bulletin             igt   IGN tel. bull. (Spain)
      gol   German events 823-1989   sol   Swiss events 80-87
      mur   Mururoa events           isr   Israel events 07-93

MOMENT TENSORS ##################################################
      cmt   CMTs from Harvard        sip   MTs from USGS (Sipkin)
      eri   CMTs from Tokyo-Univ.

SERVICE #########################################################
      on        IASPEI onset times for YOUR station
      sr        Seismotectonic region in Central Europe for given event
      fle       Flinn-Engdahl region for given event
      doy       list of days in year
      help, h   list of commands
      info      short info on display manager
      mess      short message to GERESS/DISPLAY manager
      exit, x   logout, end session
#######################################################v3.4## 8.Jun.94#jost#
```

2. MONITORING NUCLEAR TEST SITES

WITH GERESS

M. L. Jost, J. Schweitzer, and H.-P. Harjes

2.0 ABSTRACT

The GERESS array in south-eastern Germany has been proposed to participate as an α-station during the upcoming GSETT-3 test. With the aim of monitoring a comprehensive test ban treaty, special interest has emerged to asses the capability of this new array to monitor the known nuclear test sites. During the GERESS site survey (1988-1989) and 4 1/2 years of GERESS operation (Jan. 1990 - June 1994), 44 presumed nuclear events have been recorded: 18 from Nevada, 14 from the Tuamotu Archipelago, 6 from eastern Kazakhstan, 5 from Lop Nor, and 1 from Novaya Zemlya. The detection thresholds at GERESS are $m_b = 4.3$ for Nevada, $m_b = 4.0$ for Tuamotu Archipelago, $m_b = 4.6$ for Lop Nor, $m_b = 4.3$ for Novaya Zemlya, and $m_b = 4.5$ for eastern Kazakhstan. For Nevada and the Tuamotu Archipelago, these detection thresholds at GERESS correspond to a yield estimate in the order of 1 kt at each site. These path specific detection thresholds deviate substantially from those derived from global amplitude-distance relations (i.e., Gutenberg-Richter). Based on a cross-correlation method and a cluster analysis, GERESS records can be used to identify specific test sites.

2.1 INTRODUCTION

The Group of Scientific Experts (GSE) of the Conference of Disarmament (CD) in Geneva has started developing a final concept for an international seismic data exchange system (CD/1211, 1993) providing technical support for monitoring a comprehensive nuclear test ban treaty (CTBT). The near real time system includes a three-tiered global network of seismic stations where the first tier, the alpha-network, consists about half of arrays and half of three-component stations. These alpha-stations are designed to provide not only the required detection threshold throughout the world but also to achieve a preliminary event location which is then improved by the supplementary data of the beta and gamma networks. In this respect, the α-network of about 60 globally distributed stations is regarded as a teleseismic monitoring system.

Recently, the GERman Experimental Seismic System (GERESS) has been proposed to participate in the upcoming GSE Technical Test 3 (GSETT-3) as an α-station. Hence, the capabilities of the GERESS array to monitor the presently known nuclear test sites has become of interest.

Based on 4 1/2 years of GERESS data (Jan. 1990 - June 1994), this paper addresses the detection capabilities for presumed nuclear events. We also added 10 events from the GERESS site surveying phase (1988-1989) to include data from the joint verification experiments (JVE) and from the Kazakhstan test site. Due to the amount of data, we focus on events at the Nevada Test site (NTS) and events in the Tuamotu Archipelago.

2.2 THE GERESS ARRAY

Since the establishment of the Gräfenberg array (GRF) in 1975, considerable efforts have been made in Germany to use array data for monitoring underground nuclear explosions (Harjes and Hanka, 1986). After it became clear that high frequency signals play an important role for detection and identification of small underground nuclear tests at regional distances (e.g., Mykkeltveit et al., 1990; Ringdal, 1990), a 25-element short period, small aperture array in south-eastern Germany was planned. This array complements the broad-band, large aperture Gräfenberg array which had not been designed for detection purposes. The design goals of GERESS included the lowering of the global detection threshold in addition to monitoring local and regional seismicity in Central Europe and the Mediterranean earthquake zone.

The siting survey for this new array began in 1987 (Harjes, 1989). During this survey, single stations were set up near the localities Gross-Lichtenberg (GRLB 48.838 N, 13.720 E), Haidmuehle (HAID 48.800 N, 13.786 E), and Sulzberg (SULZ) at the present GERESS C2 location. These single stations operated event triggered from April-September 1988. From December 1988 to April 1989, a 9-element test-array was in operation at the present GERESS site (Harjes, 1990a). The 25-element GERESS array was installed in cooperation with Southern Methodist University (Dallas, Texas) and Ruhr-University Bochum and records are available from Apr. 1990 (Harjes, 1990b).

GERESS is located in the Bohemian Forest in south-eastern Germany near the border to Austria and the Czech Republic (Fig. 2-1). The array consists of 25 stations with vertical-component short-period Teledyne Geotech GS-13 instruments sampled at 40 Hz. In addition, four of the sites include horizontal component instruments. At the key station of the array, GEC2 (48.84511 N, 13.70156 E, 1132 m), a STS-2 broad-band instrument is sampled at 80 Hz. The geometry of the array is based on concentric rings providing an overall aperture of about 4 km (Fig. 2-2). Data from the array are continuously transmitted to the NORSAR data center in Kjeller and to the Institute of Geophysics, Ruhr-University Bochum.

The GERESS data center at Bochum is operating an experimental on-line processing system (Jost 1992b), which uses software developed at NORSAR (Mykkeltveit and Bungum, 1984; Fyen, 1987) and modified in Bochum. The automatic system detects teleseismic phases in addition to locating regional events (Harjes et al., 1993; Jost, 1993). Recently, Harjes et al. (1994) evaluated the contribution of GERESS to global seismicity using the NEIC bulletin as reference and concluded that GERESS has excellent teleseismic detection capabilities.

GERESS is located in the teleseismic distance range with respect to all nuclear test sites that were active 1988 - June 1994 (Fig. 2-3). Table 2-1 indicates the mean locations of these test sites, the epicentral distances to GERESS, and the back-azimuths. This distance range may actually be no drawback for the task of monitoring a low-yield test ban treaty. For example, GERESS automatically detected a P-wave signal from a chemical calibration experiment of 1 kt charge at NTS (sometimes called non-proliferation test (NPT)) whereas Lg waves were barely visible at the low noise station LTX at regional distance (13°, Lawson, pers. comm.).

2.3 NEVADA TEST SITE

From the total of 24 underground nuclear explosions conducted during the investigated time period, 18 waveforms are available at GERESS in addition to the aforementioned chemical NPT. 4 of the 24 events (1990/9/20 9:15 local, 1990/9/27 11:02 local, 1992/4/30 9:30 local, and 1992/6/19 VICTORIA) were too small to produce any observable signal at stations in Central Europe. During 2 tests (METROPOLIS and DISTANT ZENITH), GERESS was out. Table 2-2 shows parameters of events at NTS from 1988-1993. The two 1988 events COMSTOCK and KEARSARGE (JVE) were recorded during the site survey of GERESS at station GRLB.

Figure 2-4 shows the waveforms of all observed events from Nevada, sorted according to magnitude determined at GERESS (Table 2-2). All traces start 10 seconds before the theoretical onset time calculated from the published Department of Energy (DOE) parameters as given in NEIC using the IASP91 (Kennett and Engdahl, 1991) travel time tables. For the 2 events in 1988, single traces are shown. For the events in 1990-1993, the optimum GERESS beam is displayed. In Figures 2-4 - 2-6, we filtered all available vertical traces with a third order butterworth band-pass filter from 0.5 Hz - 2.5 Hz, 0.7 Hz - 2.0 Hz, and 1.0 Hz - 3.0 Hz, respectively, before forming the displayed optimum beam. Only forward filtering is used throughout this paper. The parameters (back-azimuth and slowness) to calculate the optimum GERESS beam were obtained from fk analysis using all available vertical traces at GERESS.

In Figures 2-4 - 2-6, we clearly see a scatter of +/- 1 sec for the observed onset times at GERESS. A first explanation would be that the absolute timing

of the GERESS array was not stable and produced these deviations. But this conclusion could be rejected because all GERESS onset times show a constant travel time difference of 7.5 - 7.8 sec with respect to published onset times of these events at the Gräfenberg array. It is obvious that the same absolute time scatter could not occur at two different arrays. In addition, we verified the relative onset times of MONTELLO and HOUSTON at stations Berggiesshübel (BRG), Collmberg (CLL), and Kaspersk'e Hory (KHC). The observed scatter of onset times can be caused in part by the velocity structure at NTS (McLaughlin et al., 1987; Ferguson et al., 1989). Because a time dependent travel time between NTS and the two arrays in Germany is not realistic our preferred hypothesis is that the published source times are not correct.

For the events in 1990-1993, we measured arrival-times, amplitudes, signal to noise ratios (SNR), and periods on the beam traces (Table 2-2). It is not surprising, that very small slowness values (the theoretical value from IASP91 is 5.13 sec/deg) were determined, since the GERESS aperture of about 4 km limits the resolution of slowness measurements in the teleseismic distance range.

The nuclear tests AUSTIN, FLOYDATA, GALENA, and DIVIDER were not detected by the automatic STA/LTA detector at GERESS but show weak signals at their expected onset times in Figures 2-4 - 2-6. The measured parameters (Table 2-2) indicate an upper limit for these events. In the filter-band 0.7 - 2.0 Hz (Fig. 2-5), weak onsets of AUSTIN, GALENA, and DIVIDER seem to be present. Parameters were measured on these beams (theoretical beam parameters). Using the optimum detection filter-band for GERESS (Jost 1992a), i.e., 1.0 - 3.0 Hz, a weak onset for FLOYDATA is visible (Fig. 2-6). Parameters of FLOYDATA were measured on the corresponding theoretical beam. For all 4 events, the fk analyses produced less reliable results due to the low SNR.

A detection threshold of m_b (NEIC) = 4.3 is estimated using 16 NTS-events recorded at GERESS in 1990-1993. This is done by comparing the measured SNR values (Table 2-2) with the threshold of the GERESS STA/LTA detector of 3.8 on a test-beam (e. g., indirect estimation method; Ringdal, 1975). The calculated GERESS m_b-values are in good agreement with the network magnitudes published by NEIC. GERESS did not detect COSO with m_b = 4.2 (GERESS). Also GALENA m_b = 4.0 (GERESS) was only detected after reprocessing at a SNR of 2.1. On the other hand, HUNTERS TROPHY with m_b = 4.2 (GERESS) and also the NPT with m_b = 4.0 (GERESS) were clearly detected with a SNR above 5. The influence of noise (day / night; wind) as well as station outages affect the SNR and can explain this variability.

In order to obtain a rough estimate on the yield from the single site GERESS, we fit a straight line through the 2 known yields: The NPT (m_b (GERESS) = 4.0) had an equivalent yield of 1 kt following Denny and Zucca (1993). The JVE (KEARSARGE) had a yield close to 150 kt but produced a body wave magnitude of only 5.4 (GERESS). On the other hand, explosions like JORNADA produced a magnitude of 5.9 at a comparable yield (Gupta et al., 1989). JORNADA was detonated below the water table and

KEARSARGE above, causing less coupling for the latter. Gupta et al. (1989) found that teleseismic m_b values for shots below the water table are 0.3 - 0.5 magnitude units larger than for shots above the water table at a fixed yield. Following these authors, we assumed that the water table influence is about 0.4 magnitude units, scaling our observed m_b = 5.4 (GERESS) for KEARSARGE to 5.8 for a regular 150 kt NTS shot below the water table. We obtained

$$\log_{10} \text{(yield)} = 1.21 \, m_b \text{ (GERESS)} - 4.84 \, . \qquad (1)$$

The resulting yield estimates from GERESS are given in Table 2-3. For comparison, magnitudes and yields determined at GRF by Schlittenhardt (1988b-1992) are included. Using Nuttli's (1986, 1987) linear relation between m_b (Lg) and yield and taking proper care of the magnitude bias between P-wave and Lg-wave magnitudes, we obtained further yield estimates from GERESS P-wave magnitudes (Table 2-3). Recently, Goldstein et al. (1994) estimated the yield for BRISTOL as 10 kt. They argued that their value could be 30 % lower due to differences in coupling. We estimated for BRISTOL 7 kt from (1), and 8 kt using Nuttli's relation. Essentially, the yield estimates from (1), Nuttli's relation, and GRF are not significantly different considering the lack of detailed shot information (e.g., water table, spall). In addition, effects of local geology can affect teleseismic P-wave magnitudes introducing uncertainty to the yield estimate (McLaughlin et al., 1987; Cormier, 1987). In Table 2-3, a yield estimation was calculated for all events. This estimation together with the automatic detection of the NPT suggest that GERESS can detect events in the order of 1 kt at NTS.

Furthermore, Table 2-3 suggests that GERESS can observe nuclear tests at NTS clearly below a yield estimate of 1 kt. Although small events like FLOYDATA or GALENA were not automatically detected, their visible waveforms can be used to confirm a location hypothesis within the framework of GSETT-3.

In order to identify subgroups of the Nevada data set, we performed cross-correlations of the optimum beams. Figure 2-7 shows the correlation matrix obtained by using the maximum cross-correlation value for the filter-band 0.5-2.5 Hz and the event numbers from Table 2-3. We clearly see that the small events (mb < 4.3; events # 1 - # 7) do not have a correlation larger than 0.54, possibly due to the small SNR. On the other hand, the cross-correlation sequences for FLOYDATA, AUSTIN, DIVIDER, and GALENA indicate that the observed waveforms are from the corresponding events at NTS. For the larger events (mb > 4.6; events # 8 - # 19), the correlation reaches values of up to 0.91.

We further performed a single linkage clustering analysis (Everitt, 1993). Figure 2-8 shows the corresponding dendrogram. We see that JUNCTION (# 17), MONTELLO (# 10), HOUSTON (# 14), and COMSTOCK (# 13) form a cluster. Also KEARSARGE (# 12) and BEXAR (# 15) form a subgroup. An explanation for the latter could be the nearly identical shot-locations (Fig. 2-9). Also HUNTERS TROPHY (# 6) and the NPT (# 5) appear somewhat related, although the significance level is rather low. Obviously, the shots at Pahute

15

Mesa and Yucca Flat do not form independent clusters. This result agrees with previous observations by Murphy et al. (1989) who found that the seismic source characteristics of both testing areas are identical for tests below the water table. In general, we observe large correlation coefficients for events at Pahute Mesa (Fig. 2-9). There the depth of burial is larger compared to events at Yucca Flat implying a larger yield. The lower correlation values for most of the shots at Yucca Flat are probably due to their small size and hence the small SNR of the beams entering the correlation analysis. Another reason may be the variability of the geologic structure at Yucca Flat (e.g., McLaughlin et al., 1987; Cormier, 1987; Ferguson, 1988).

2.4 TUAMOTU ARCHIPELAGO

In the epicentral distance range between 143° and 147°, the structure of the Earth's core amplifies - like a focusing lens - seismic waves which travel through the Earth's core as PKP-phases. The comparison of the daily detection lists of GERESS with bulletins of international seismic data centers shows that GERESS is therefore very sensitive for the seismicity in the southern Pacific. The two French nuclear test sites Mururoa and Fangataufa are located very close to each other in the Tuamotu Archipelago (Table 2-1). They have an epicentral distance to GERESS of about 145.5°, right where the maximum of the PKP-caustic is observed. Therefore, we expect a low detection level for seismic events at these test sites.

The waveforms of 14 presumed French nuclear tests in 1988-1991 are shown in Figure 2-10 (optimum beams, single traces for events in 1988, all filtered 0.5 - 2.5 Hz). The events are ordered with respect to increasing yield estimate (Table 2-4). Table 2-4 gives the corresponding parameters measured on the optimum beams (events in 1990 and 1991) or on the single traces for the events in 1988 (recorded at station HAID). The French authorities have not yet published any parameters of their tests. Therefore, the start time of the waveform for the event on Nov. 14, 1990 was chosen to 10 seconds before the measured onset time. The other traces were aligned to its first minimum. In 1991, one of the presumed explosions was not detected by GERESS (Jul 5, 1991; 18:00). This event was very small and was only detected by a T-phase observation at Raratonga (RAR). The yield was estimated by DSIR (Smith, pers. communication) as less than 0.3 kt. Figure 2-10 also displays the GERESS theoretical beam at the expected onset time for this event, but no conclusive signal could be identified.

The body wave magnitude m_b is not defined for events with an epicentral distance of more than about 100° and no direct m_b determination is possible for these events from GERESS. Schlittenhardt (1988a) introduced a body wave magnitude for PKP-observations of the French explosions at the Gräfenberg array. Although the distance between the reference station A1 of GRF and

16

GERESS is only about 200 km, we cannot use his results to estimate m_b-values because the site conditions differ substantially. The amplitude-distance behavior of the PKP-phases varies drastically in the distance range near 145.5° (e. g., Houard et al., 1993), and we corrected the observed log (A/T) values with the attenuation curve of Blandford and Sweetser (1973) for PKP-phases. With the correction value of 3.50 for an epicentral distance of 145.5°, we determined the m_b(PKP)-values for the presumed French tests. For 11 of these events, our m_b(PKP)-values can be compared with m_b-determinations by NEIC. Although our m_b values are slightly smaller than the network magnitudes by NEIC, the general agreement between the m_b-values calculated with different methods confirms the proposed usage of PKP-phases for regular world-wide monitoring (Harjes, 1985).

Figure 2-11 shows the estimated m_b(PKP)-values for GERESS plotted against the yields estimated by DSIR (Table 2-5, Smith, pers. communication). The line follows the linear relationship (least squares fit) between log(yield) and m_b (PKP)-values:

$$\log_{10} (\text{yield}) = 1.24 \, m_b \, (\text{PKP}) - 4.88 \, . \qquad (2)$$

This relation is very similar to the results of Schlittenhardt (1988a) who got for m_b(PKP) based on GRF measurements:

$$\log_{10} (\text{yield}) = 1.12 \, m_b \, (\text{PKP})_{GRF} - 4.58 \, . \qquad (3)$$

The two solid lines in Figure 2-11 give the upper limits for the smallest not observed explosion. On average, the GERESS detection threshold is about m_b(PKP) = 3.8 corresponding to a yield estimate of 0.7 kt. For the network (NEIC) magnitude, the GERESS detection threshold is 4.0.

Nuclear tests in the Tuamotu Archipelago have been reported to be detonated either on the island of Mururoa or on the island of Fangataufa with about 40 km in between. The corresponding variation in slowness and azimuth for PKP-onsets is so small that even large aperture arrays (e.g., GRF) are not able to discriminate between the 2 test sites. Therefore, we used a different approach and performed a cross-correlation of all recorded events (1988-1991). We used a 30 second time window of the optimum GERESS beams filtered between 0.5-2.5 Hz. Figure 2-12 shows a cross-correlation sequence of the event on Nov. 21, 1990 with all events in 1990-1991. Note that the cross-correlation coefficients of the three events on the bottom of the figure, reportedly placed on Fangataufa, are significantly different (very small) from those reportedly placed on Mururoa. The cross-correlation coefficients are also small for the first two events. The first event has been classified as not observed, and the second (yield in the order of 1 kt), although observed, is contaminated with too much noise. On the other hand, the cross-correlation sequence indicates that the observed waveform is from the corresponding event at Tuamotu. Figure 2-13 shows the cross-correlation matrix obtained by using the maximum cross-correlation value in the filter-band 0.5-2.5 Hz and the event numbers from Table 2-5. Table 2-6 lists the minimum and maximum correlation coefficients for each event with respect to the Mururoa and Fangataufa clusters. Repeating

the correlation analysis including all recorded events in 1988 shows that the difference of correlation coefficients between those two clusters decreases. We explain this by the larger noise level of the single station records (events in 1988). Other pass-bands (0.7-2.0 Hz, 1.0-3.0 Hz) generally support the present finding, although the observed grouping of correlation-coefficients is optimum for most events in the pass-band of 0.5-2.5 Hz. The cross-correlation sequence of the event on May 25, 1988 (# 11) which had the largest reported yield on Mururoa (83 kt) also agrees with the present finding, where an unexplained de-correlation with the event on June 2, 1990 (# 8) is observed (Fig. 2-13). Figure 2-14 shows the dendrogram based on a single linkage clustering analysis. We clearly see the different Fangataufa and Mururoa clusters. The event # 2 (07/05/1991; 1 kt) has a very small SNR which makes a reasonable analysis impossible. On the other hand, we see some variability in the Mururoa cluster; e.g. events # 4 (18/5/1991), # 10 (21/11/1990), and # 9 (15/07/1991) appear to form a subgroup and also the events # 6 (11/05/1988), # 5 (04/07/1990), and # 7 (14/06/1991). This observation may result from the observed local site effects (Crusem and Caristan, 1992).

Following Guille et al. (1993), the atoll of Mururoa (28 km by 10 km; age 11.8-10.6 My) is part of the volcanic chain from the hot-spot near the island of Pitcairn. Mururoa sits on top of a submarine plateau of 130 km by 30 km oriented N80E. The existence of this plateau is intimately linked to the Austral fracture zone which explains the atypical orientation of this plateau. Although the island of Fangataufa (10 km by 5 km; age 11.5-9.6 My) is situated only 40 km south-east of Mururoa, the influence of this fracture Zone is minor. The morphology of the basement is star shaped, quite different from the elongated plateau of Mururoa. Typical tectonic directions on Fangataufa follow those of the southern Pacific (NS, N80E, and N115E). The bathymetry also supports a generic difference between both islands: the strait separating both islands shows water-depths larger than 3 km for about 20 km. As a result, both islands exhibit different tectonic settings that can be responsible for the observed clustering.

We conclude that based on the limited data set (14 events), the optimum GERESS beams can be used in a correlation analysis (waveform matching) to successfully separate the Mururoa and Fangataufa clusters. French authorities have not yet published any information on their tests. Therefore we cannot know to which degree the above results reflect different device types.

18

2.5 LOP NOR

GERESS recorded 5 of the 6 presumed nuclear explosions at the Chinese test site Lop Nor in 1990-1994. Figure 2-15 displays the optimum beams filtered 0.5 - 2.5 Hz. Parameters measured on the optimum beams are given in Table 2-7. The observed body wave magnitudes are unexpected low compared to the network magnitudes (NEIC). This observed discrepancy suggests that GERESS has a significant station residual for Nop Lor events. However, GERESS generally shows a negative magnitude residual for events in western China and the Himalaya region of -0.51 +/- 0.26 magnitude units. With a STA/LTA detection threshold of 3.8 of the GERESS detector, this implies a detection threshold for events at Lop Nor of m_b (NEIC) = 4.6.

For 4 events, surface wave magnitudes could be measured at GERESS (Table 2-7). However for the events in 1990 and 1993, the magnitude values give an upper bound only since the traces were disturbed by interfering noise. The classical m_b / MS-ratios at GERESS clearly confirm the explosion source type for all 4 events. On the other hand, Lop Nor records show a comparatively strong Love-wave radiation towards European stations, which is not expected for an explosion type source. Note that the surface wave magnitude measured on the horizontal component instruments is significantly larger than the magnitude measured on the vertical instrument (Table 2-7) because the Love wave shows the largest amplitude in the surface wave group.

The test on May 21, 1992 was the largest underground explosion which has ever been observed with broad-band stations world-wide. To demonstrate the simple pulse form of relatively high frequency for this large event, Figure 2-16 shows the deconvolved P and PcP onsets. In both cases, a long periodic down swing after the first onset is seen which can be addressed as an effect of tectonic release related with this event (Gao and Wallace, 1992).

2.6 NOVAYA ZEMLYA

On October 24, 1990, the Soviet Union carried out its last nuclear test (Table 2-8). This test was conducted on Novaya Zemlya at a distance of 30.4° to GERESS. The records are dominated by the very prominent P-wave coda (Fig. 2-17, optimum beam, filtered 0.5 - 2.5 Hz), and a very complex pulse of the direct P-wave. This feature must be explained by contributions from the direct waves of the upper mantle triplications, by converted phases, multipathing, and by a lateral heterogeneous structure of crust and upper mantle in Europe. The observed magnitude m_b = 5.5 for this explosion is in agreement with NEIC (m_b = 5.7). The classical m_b / MS-ratio (5.5 / 4.4 = 1.3) at GERESS clearly confirms the explosion source. With the observed SNR of 90.3 the detection threshold at GERESS can be estimated at m_b (NEIC) = 4.3.

Using Nuttli's (1986, 1988) linear relation between m_b (Lg) and yield and taking proper care of the magnitude bias between P-wave and Lg-wave magnitudes, we obtained a yield estimate of 50 kt from the GERESS P-wave magnitude. Schlittenhardt (1988b-1992) determined the yield for the Novaya Zemlya test as 70 kt based on GRF records (m_b(GRF)=5.9). For GERESS, we estimated a detection threshold in the order of 3 kt. Note that this value is based on one single shot only.

2.7 EASTERN KAZAKHSTAN

During the site survey for GERESS, 6 events from the former Soviet test site near the city of Semipalatinsk were recorded. All tests were conducted at the Shagan River (Balapan) subsection of the testing area (e.g., Thurber et al., 1993). We recorded the event on May 4, 1988 at the temporary station HAID, and the tests on Jun 14 and Sep 14 (JVE), 1988 at the temporary station GRLB (Harjes, 1989). The three events in Dec. 1988, Jan. and Feb. 1989 were recorded with the temporary 9-element GERESS test array (Harjes 1990a). Figure 2-18 shows the single traces and the optimum beams, respectively, filtered between 0.5 Hz - 2.5 Hz. Except for the event on June 14, 1988, magnitudes measured at the GERESS site correlate well with the ISC network magnitudes (Table 2-9). Based on these 6 events, an average detection threshold of m_b (NEIC) = 4.7 has been determined. This estimate gives an upper bound only, since the 25-element GERESS array shows a significantly better SNR improvement by beamforming than a single station or the 9-element test array. Hence, the detection threshold for the 25-element GERESS array can be estimated to be lower than 4.5 for eastern Kazakhstan. This estimate is conservative because the comparison of the technical installation of GERESS and the temporary test array suggests a sensitivity surpassing the expected $\sqrt{N}$ SNR improvement. Ringdal (1990) determined the 50% detection threshold for NORESS as m_b = 2.7 - 3.3. The discrepancy to the estimate for GERESS is in part due to the well documented focusing effects in the upper mantle below the test site towards Scandinavia. Barker and Murphy (1992) determined station residuals in Europe which amount to more than 1 magnitude unit.

In Table 2-10, we compare various yield determinations for the 6 presumed tests. Using Nuttli's (1986, 1987) linear relation between m_b (Lg) and yield and taking proper care of the magnitude bias between P-wave and Lg-wave magnitudes, we obtained yield estimates from GERESS P-wave magnitudes. Included are also yield estimates by Schlittenhardt (1988b-1992) from GRF records. Based on the Lg wave at NORSAR, Hansen et al. (1990) calculated a yield of 110 kt for the JVE on Sep. 14, 1988. This value agrees with our estimate of 108 kt at GERESS. From hydrodynamic measurements, the yield was determined from US and USSR scientists at 115 kt and 122 kt, respectively (Sykes and Ekström, 1989). Ringdal et al. (1992) and also

20

Ekström and Richards (1994) estimated source parameters. Considering the variability in published yield determinations, our single station value can give a valid first order estimate on yield. Hence, for the 25-element GERESS array, a detection threshold in the order of 2 kt is estimated.

2.8 CONCLUSIONS

During the GERESS site survey (1988-1989) and 4 1/2 years of GERESS operation (Jan. 1990 - June 1994), 44 presumed nuclear tests have been recorded: 18 from Nevada, 14 from the Tuamotu Archipelago, 6 from eastern Kazakhstan, 5 from Lop Nor, and 1 from Novaya Zemlya. The detection thresholds at GERESS are estimated as m_b = 4.3 for Nevada, m_b = 4.0 for Tuamotu Archipelago, m_b = 4.6 for Lop Nor, m_b = 4.3 for Novaya Zemlya, and m_b = 4.5 for eastern Kazakhstan. These path specific detection thresholds deviate substantially from those derived from global amplitude-distance relations (i.e., Gutenberg-Richter). They can also not be explained with a simple station bias because GERESS generally shows a negative station residual of 0.6 magnitude units +/- 0.35 (Harjes et al., 1994). Based on 2 known yields, a magnitude yield relation was calculated for Nevada, indicating that events with a yield estimate in the order of 1 kt can be detected at GERESS. Based on yield estimates by DSIR (Smith, pers. comm.), a magnitude yield relation was determined for events in the Tuamotu Archipelago. The detection threshold of m_b = 4.0 would correspond to events with a yield estimate in the order of 0.7 kt. However, for Novaya Zemlya and the Kazakhstan test sites, yields have been determined by various authors. Although the data quantity and quality at GERESS for these test sites is not ideal, we estimated a detection threshold of 3 kt for Novaya Zemlya and 2 kt for Kazakhstan. Based on a cross-correlation method and a cluster analysis, GERESS records can be used to discriminate between the Tuamotu and Fangataufa events.

This case study also shows that caution should be exercised by using results of theoretical studies on network detection capabilities. Instead, path specific station detection thresholds should be used for a fixed station network to derive reliable network detection capabilities.

A reliable prediction of the performance of a future global monitoring network would greatly benefit from information about exact parameters of previous nuclear tests. In this respect, the Chinese and French authorities should be appealed to release the corresponding information even without exact yield information.

ACKNOWLEDGEMENTS

REFERENCES

Barker, B. W. and J. R. Murphy (1992). A lithospheric velocity anomaly beneath the Shagan River test site. Part 1. Detection and location with network magnitude residuals, *Bull. Seism. Soc. Am.* **82**, 980-998.

Blandford, R. R. and E. I. Sweetser (1973). Seismic distance-amplitude relation for short period P, P_{diff}, PP, and compressional core phases for delta > 90 deg. Teledyne-Geotech, SDAC-TR-73-9, Alexandria, VA.

Conference of Disarmament CD1211 (1993). Progress report of the Ad Hoc Group of Scientific Experts to the conference on disarmament on the 36. session to consider international cooperative measures to detect and identify seismic events.

Cormier, V. F. (1987). Focusing and defocusing of teleseismic P-waves by known three-dimensional structure beneath Pahute Mesa, Nevada test site, *Bull. Seism. Soc. Am.* **77**, 1688-1703.

Crusem, R. and Y. Caristan (1992). Moment tensor inversion, yield estimation, and seismic coupling variability at the French centre d'experimentation du Pacifique, *Bull. Seism. Soc. Am.* **82**, 1253-1274.

Denny, M. and J. Zucca (1993). DOE non-proliferation experiment includes seismic data, *EOS, Trans. Am. Geophys. Union* **74**, No. 45, 527.

Ekström, G. and P. G. Richards (1994). Empirical measurements of tectonic moment release in nuclear explosions from teleseismic surface waves and body waves, *Geophys. J. Int.* **117**, 120-140.

Everitt, B. S. (1993). *Cluster Analysis*, Edward Arnold, London.

Ferguson, J. F. (1988). Body-wave magnitude variation at Yucca Flat, Nevada, *Bull. Seism. Soc. Am.* **78**, 863-872.

Ferguson, J. F., A. H. Cogbill, R. G. Warren, and H. D. Axilrod (1989). A geophysical data base for NTS: a new interpretation for the shallow structure of Silent Canyon Caldera, Pahute Mesa, Nevada, in: *Proceedings of the 11th Annual DARPA/AFGL Seismic Research Symposium*, Arlington, VA., 505-514. GL-TR-90-0301, ADA229228

Fyen, J. (1987). Improvements and Modifications, Semiannual Technical

Summary, 1 October 1986 - 31 March 1987, *NORSAR Sci. Rep. No. 2-86/87*, Kjeller, Norway.

Gao, L. and T. C. Wallace (1992). Seismotectonics of the Lop Nor region, Northwest China (abstract). *EOS, Trans. Am. Geophys. Union* **73**, 359.

Goldstein, P., M. D. Denny, T. Hauk, and S. P. Jarpe (1994). On-site seismic yield (OSSY) estimates for BRISTOL based on nuclear to chemical explosion spectral ratios and yield scaling, *Bull. Seism. Soc. Am.* **84**, 343-349.

Guille, G., G. Goutiere, and J. F. Somein (1993). *Les Atolls de Mururoa and Fangataufa (Polynesie Francaise), I. Geologie, Petrologie, Hydrogeologie*, Louis-Jean, Gap.

Gupta, I. N., C. S. Lynnes, and R. A. Wagner (1989). A study of Soviet PNE's and spectral differences between below and above water table NTS shots, in: *Proceedings of the 11th Annual DARPA/AFGL Seismic Research Symposium*, Arlington, VA., 92-101. GL-TR-90-0301, ADA229228

Hansen, R. A., F. Ringdal, and P. G. Richards (1990). The stability of RMS Lg measurements and their potential for accurate estimation of the yields of Soviet underground nuclear explosions, *Bull. Seism. Soc. Am.* **80**, 2106-2126.

Harjes, H. P. (1985) : Global seismic network assessment for teleseismic detection of underground nuclear explosions. *J. Geophys.* **57**, 1-13.

Harjes, H. P. (1989) : Siting survey and configuration optimization of a new regional array in the Federal Republic of Germany, DARPA Annual Report No. AFGL-TR-89-0073. ADA209981

Harjes, H.-P. (1990a). Siting survey and configuration optimization of a new regional array in the Federal Republic of Germany, DARPA Annual Report No. GL-TR-90-0116. ADA223486

Harjes, H.-P. (1990b). Design and siting of a new regional array in Central Europe, *Bull. Seism. Soc. Am.* **80**, 1801-1817.

Harjes, H. P. and W. Hanka (1986) : The contribution of broad-band array seismology to seismic monitoring of underground nuclear explosions. Geolog. Jb. E **35**, 105-120.

Harjes, H.-P., M. L. Jost, J. Schweitzer, and N. Gestermann (1993). Automatic seismogram analysis at GERESS, *Computers & Geosciences* **19**, 157-166.

Harjes, H.-P., M. L. Jost, and J. Schweitzer (1994). Preliminary calibration of candidate alpha stations in the GSETT-3 network, (submitted to Annali di Geofisica).

Houard, S., J. L. Plantet, J. P. Massot, and H. C. Nataf (1993). Amplitudes of core waves near the PKP caustic, from nuclear explosions in the South Pacific recorded at the "Laboratoire de Detection et Geophysique" network, in France, *Bull. Seism. Soc. Am.* **83**, 1835-1854.

Jost, M. L. (1992a). GERESS P-wave detectability, in: *Advanced Waveform Research Methods for GERESS Recordings*, DARPA Annual Report No. PL-TR-92-2142, 13-24. ADA253686

Jost, M. L. (1992b). Current status and results of the GERESS data center in

23

Bochum, in: *Proceedings of the GERESS Symposium, Waldkirchen June 22-24, 1992*, Ruhr-University Bochum, 93-102.

Jost, M. L. (1993). GERESS status report January 1993 - December 1993, in *Advanced Waveform Research Methods for GERESS Recordings*, Semi-annual Report to ARPA, Ruhr-University Bochum.

Kennett, B. L. N. and E. R. Engdahl (1991). Traveltimes for global earthquake location and phase identification, *Geophys. J. Int.* 105, 429-465.

McLaughlin, K. L., L. M. Anderson, and A. C. Lees (1987). Effects of local geologic structure on Yucca Flats, Nevada test site, explosion waveforms: two dimensional linear finite difference simulations, *Bull. Seism. Soc. Am.* 77, 1211-1222.

Murphy, J. R., B. W. Barker, and A. O'Donnell (1989). Network-averaged teleseismic P-wave spectra for underground explosions. Part I. Definitions and examples, *Bull. Seism. Soc. Am.* 79, 141-155

Mykkeltveit, S. and H. Bungum (1984). Processing of regional seismic events using data from small-aperture arrays, *Bull. Seism. Soc. Am.* 74, 2313-2333.

Mykkeltveit, S., F. Ringdal, T. Kvaerna, and R. W. Alewine (1990). Application of regional arrays in seismic verification research, *Bull. Seism. Soc. Am.* 80, 1777-1800.

Nuttli, O. W. (1986). Lg magnitudes of selected East Kazakhstan underground explosions, *Bull. Seism. Soc. Am.* 76, 1241-1251.

Nuttli, O. W. (1987). Lg magnitudes of Degelen, East Kazakhstan, underground explosions, *Bull. Seism. Soc. Am.* 77, 679-681.

Nuttli, O. W. (1988). Lg magnitudes and yield estimates for underground Novaya Zemlya nuclear explosions, *Bull. Seism. Soc. Am.* 78, 873-884.

Ringdal, F. (1975). On the estimation of seismic detection thresholds, *Bull. Seism. Soc. Am.* 65, 1631-1642.

Ringdal, F. (1990). Teleseismic event detection using the NORESS array, with special reference to low-yield Semipalatinsk explosions, *Bull. Seism. Soc. Am.* 80, 2127-2142.

Ringdal, F., P. D. Marschall, and R. W. Alewine (1992). Seismic yield determination of Soviet underground nuclear explosions at the Shagan River test site, *Geophys. J. Int.* 109, 65-77.

Schlittenhardt, J. (1988a) : Seismic yield estimation using teleseismic P- and PKP-waves recorded at the GRF-(Gräfenberg) array. *Geophys. J.* 95, 163-179.

Schlittenhardt, J. (1988b-1992) : Kernexplosionen, in: *Seismische Verifikation* Annual reports of Bundesanstalt für Geowissenschaften und Rohstoffe (BGR) 1988-1992, Hannover.

Sykes, L. and G. Ekström (1989). Comparison of seismic and hydrodynamic yield determinations for the Soviet Joint Verification Experiment of 1988, *Proc. Natl. Acad. Sci. USA* 86, 3456-3460.

Thurber, C. H., H. R. Quin, and P. G. Richards (1993). Accurate locations of nuclear explosions in Balapan, Kazakhstan, 1987 to 1989, *Geophys. Res. Let.* 20, 399-402.

Table 2-1: Distances of Nuclear Test Sites to GERESS

Country	Test Site	Lat	Long	Δ [deg]	BAZ [deg]
China	Lop Nor	41.6 N	88.7 E	51.3	68
France	Fangataufa	22.2 S	138.8 W	145.6	311
France	Mururoa	21.9 S	139.0 W	145.4	311
Great Britain	Nevada	37.2 N	116.2 W	83.5	322
USA	Nevada	37.2 N	116.2 W	83.5	322
USSR	Kazakhstan	49.9 N	78.8 E	41.2	63
USSR	Novaya Zemlya	73.4 N	54.7 E	30.4	22

Table 2-2: Parameters of Events from Nevada Test Site Recorded at GERESS 1988-1993

Yr	Mo	Day	Name	Onset Time	Ampl [nm]	Period [sec]	SNR	m_b GERESS	m_b NEIC	ML BRK	BAZ [deg]	Slowness [sec/deg]	Cmt
1988	Jun	2	COMSTOCK	13:12:29.5	27.10	1.10	10.5	5.4	5.4	5.3			1
1988	Aug	17	KEARSARGE, JVE	17:12:29.5	27.03	1.17	18.6	5.4	5.5	5.4			1
1990	Mar	10	METROPOLIS						5.0	5.1			2
1990	Jun	13	BULLION	16:12:29.8	57.52	1.11	93.5	5.7	5.7	5.6	325.3	2.98	
1990	Jun	21	AUSTIN	18:27:30.8	<0.77	1.08	<1.5	<3.9	4.0	4.3			3
1990	Jul	25	MINERAL QUARRY	15:12:30.5	4.38	0.99	8.3	4.7	4.7		327.5	2.87	
1990	Oct	12	TENABO	17:42:30.1	31.07	1.07	55.9	5.5	5.6	5.4	319.9	3.60	
1990	Nov	14	HOUSTON	19:29:29.9	22.53	0.97	59.1	5.4	5.4	5.1	329.1	4.58	
1991	Mar	08	COSO	21:15:15.1	1.77	1.01	3.2	4.2	4.3	4.6	306.3	4.16	
1991	Apr	04	BEXAR	19:12:29.2	38.31	1.21	58.9	5.5	5.6	5.4	326.0	3.65	
1991	Apr	16	MONTELLO	15:42:29.5	18.57	0.99	48.1	5.3	5.4	5.4	331.8	3.64	
1991	Aug	15	FLOYDATA	16:12:30.5	<0.20	0.54	<1.5	<3.6	4.2	4.0			3, 4
1991	Sep	14	HOYA	18:12:29.9	42.35	1.19	121.7	5.6	5.5	5.3	330.5	3.36	
1991	Sep	19	DISTANT ZENITH						4.0	3.8			2
1991	Oct	18	LUBBOCK	19:24:29.9	14.99	1.02	19.3	5.4	5.2	5.0	322.6	3.28	
1991	Nov	26	BRISTOL	18:47:30.0	5.12	1.13	10.9	4.7	4.6	4.6	338.9	4.36	
1992	Mar	26	JUNCTION	16:42:29.0	45.20	1.29	42.0	5.6	5.5	5.4	332.9	3.53	
1992	Jun	23	GALENA	15:12:30.5	<1.40	1.38	<2.1	<4.0		3.9			3
1992	Sep	18	HUNTERS TROPHY	17:12:30.2	1.40	0.97	5.3	4.2	4.4		348.3	6.32	3
1992	Sep	23	DIVIDER	15:16:30.8	< 0.60	0.71	1.8	< 3.9	4.4	4.3	(282.4)	(5.63)	3
1993	Sep	22	NPT	07:13:29.2	1.30	0.97	5.4	4.0	4.1		335.0	5.73	

1: Single station of GERESS site investigation

2: GERESS out

3: Onset at GERESS very weak, parameters indicate upper threshold

4: Amplitude measured on trace filtered 1.0-3.0 Hz

26

Table 2-3: Magnitude Yield Relations for NTS

Yr	Mo	Day	Name / Site	m_b GRF	Yield GRF	m_b GERESS	Yield GERESS	Yield Nuttli	No.
1988	Jun	2	Comstock	5.4	60	5.4	49	68	13
1988	Aug	17	Kearsarge, JVE	5.5	75	5.4	150	68	12
1990	Jun	13	Bullion	5.8	150	5.7	114	150	19
1990	Jun	21	Austin			<3.9	<0.8		2
1990	Jul	25	Mineral Quarry	5.0	20	4.7	7	8	9
1990	Oct	12	Tenabo	5.6	90	5.5	65	92	16
1990	Nov	14	Houston	5.5	70	5.4	49	68	14
1991	Mar	08	Coso			4.2	2		7
1991	Apr	04	Bexar	5.7	110	5.5	65	92	15
1991	Apr	16	Montello	5.4	50	5.3	37	50	10
1991	Aug	15	Floydata			<3.6	<0.3		1
1991	Sep	14	Hoya	5.6	90	5.6	86	125	18
1991	Oct	18	Lubbock	5.2	30	5.4	49	68	11
1991	Nov	26	Bristol	4.9	10	4.7	7	8	8
1992	Mar	26	Junction	5.6	100	5.6	86	125	17
1992	Jun	23	Galena			<4.0	<1		4
1992	Sep	18	Hunters Trophy			4.2	2		6
1992	Sep	23	Divider			<3.9	<0.7		3
1993	Sep	22	NPT			4.0	1		5

The GERESS yields are from log y = 1.21 mb - 4.84. The Nuttli yields were calculated using his 1986 paper and GERESS magnitudes (see text).

The No. column indicates a sorting of the events according to mb(GERESS).

Table 2-4: Parameters of Events from Tuamotu Archipelago Recorded at GERESS 1988-1991

Yr	Mo	Day		Onset Time	Ampl [nm]	Period [sec]	SNR	m$_b$(PKP) GERESS	m$_b$ NEIC	DSIR-Yield [kt]	Cmt
1988	05	11	M	17:19:40.0	41.11	0.72	34.3	5.26	5.5	20	1
1988	05	25	M	17:20:39.9	71.76	1.12	18.5	5.31	5.6	83	1
1990	06	02	M	17:49:38.6	32.69	0.88	58.0	5.07	5.3	30	
1990	06	07	M	17:49:39.5	5.77	0.90	16.4	4.31	-	3	
1990	06	26	F	18:19:39.9	148.54	1.57	102.2	5.48	5.5	100	
1990	07	04	M	18:19:39.5	14.68	0.87	28.4	4.73	5.1	18	
1990	11	14	F	18:31:39.9	142.79	1.50	111.5	5.48	5.5	117	
1990	11	21	M	17:19:39.6	64.65	0.81	89.8	5.40	5.4	36	
1991	05	07	M	17:19:39.4	2.14	0.72	6.9	3.97	-	1	
1991	05	18	M	17:34:39.6	22.69	0.81	86.4	4.95	5.1	16	
1991	05	29	F	19:19:39.6	120.49	1.46	141.3	5.42	5.5	107	
1991	06	14	M	18:19:39.2	37.99	0.93	135.4	5.11	5.2	28	
1991	07	05	M	18:19:38.9	<0.80	1.30	-	<3.30	-	<0.3	
1991	07	15	M	18:29:39.4	42.65	0.81	91.8	5.22	5.3	34	2

M: event probably on Mururoa
F: event probably on Fangataufa
1: Single station of GERESS site investigation
2: event not observed, parameters measured on noise at theor. onset time

Table 2-5: Magnitude Yield Relations for Tuamotu Archipelago

Yr	Mo	Day	Name / Site	m_b GRF	Yield GRF	m_b GERESS	Yield DSIR	No.
1988	05	11	Mururoa		40	5.3	20	6
1988	05	25	Mururoa		65	5.3	83	11
1990	06	02	Mururoa	5.4	40	5.1	30	8
1990	06	07	Mururoa	4.8	10	4.3	3	3
1990	06	26	Fangataufa	5.7	100	5.5	100	12
1990	07	04	Mururoa	5.2	20	4.7	18	5
1990	11	14	Fangataufa	5.7	120	5.5	117	14
1990	11	21	Mururoa	5.7	35	5.4	36	10
1991	05	07	Mururoa	4.6	4	4.0	1	2
1991	05	18	Mururoa	5.4	30	5.0	16	4
1991	05	29	Fangataufa	5.8	90	5.4	107	13
1991	06	14	Mururoa	5.5	50	5.1	28	7
1991	07	05	Mururoa		<0.5	<3.3	<0.3	1
1991	07	15	Mururoa	5.6	70	5.2	34	9

The No. column indicates a sorting of the events according to yield estimate (DSIR).

Table 2-6: Results of Correlation Analysis of Events from Tuamotu Archipelago

Yr	Mo	Day	Cluster	cc of Mururoa Cluster		cc of Fangataufa Cluster		δcc	Rem.
				min cc	max cc	min cc	max cc		
1988	05	11	M	0.53	0.84	0.27	0.32	0.21	
1988	05	25	M	0.56	0.76	0.35	0.44	0.12	(1)
1990	06	02	M	0.64	0.76	0.30	0.31	0.33	
1990	06	07	M	0.62	0.74	0.31	0.38	0.24	
1990	06	26	F	0.30	0.49	0.82	0.94	0.33	
1990	07	04	M	0.74	0.83	0.46	0.52	0.22	
1990	11	14	F	0.30	0.58	0.82	0.90	0.24	
1990	11	21	M	0.72	0.91	0.45	0.48	0.24	
1991	05	07	M	0.44	0.51	0.25	0.28	0.12	
1991	05	18	M	0.62	0.91	0.44	0.47	0.15	
1991	05	29	F	0.31	0.48	0.90	0.94	0.42	
1991	06	14	M	0.64	0.83	0.49	0.58	0.06	
1991	07	05	M	0.18	0.40				(2)
1991	07	15	M	0.71	0.88	0.43	0.48	0.23	(3)

cc: correlation coefficient
(1): This event decorrelates with that one on June 2, 1990 (cc=0.40)
(2): Difference in correlation coefficients is 0.13 in pass-band 1.0-3.0 Hz
(3): Event not observed

Table 2-7: Parameters of Events from Lop Nor Recorded at GERESS 1990-1994.

Yr	Mo	Day	Onset Time	Ampl [nm]	Period [sec]	SNR	m_b GERESS	m_b NEIC	MSZ GERESS	MSH GERESS	BAZ [deg]	Slowness [sec/deg]
1990	May	26	08:09:07.4	6.5	0.90	10.0	4.6	5.4	3.51	4.14	68.0	7.84
1990	Aug	16						6.2				
1992	May	21	05:09:06.3	334.8	0.84	364.0	6.3	6.5	4.75	5.19	65.8	7.23
1992	Sep	25	08:09:04.4	6.2	1.33	5.3	4.4	5.0			61.8	7.69
1993	Oct	5	02:09:04.7	35.2	1.03	118.0	5.2	5.9	3.77	4.16	66.2	7.02
1994	Jun	10	06:35:06.8	18.2	0.63	95.4	5.2	5.7	3.30	3.84	67.9	7.25

GERESS was out for the event on Aug 16, 1990.

31

Table 2-8: Parameters of the Event from Novaya Zemlya Recorded at GERESS 1990

Yr	Mo	Day	Onset Time	Ampl [nm]	Period [sec]	SNR	m_b GERESS	m_b NEIC	MSZ GERESS	MSH GERESS	BAZ [deg]	Slowness [sec/deg]
1990	Oct	24	15:04:14.0	85.9	1.12	90.3	5.5	5.7	4.45	4.36	29.2	9.02

Table 2-9: Parameters of Events from Kazakhstan Test Site Recorded at the GERESS Site 1988-1989

Yr	Mo	Day	Onset Time	Ampl [nm]	Period [sec]	SNR	m_b GERESS	m_b ISC	MS ISC	BAZ [deg]	Slowness [sec/deg]	Cmt
1988	May	4	01:04:54.6	326.6	1.04	131.0	6.0	6.1	4.9			1
1988	Jun	14	02:34:55.2	4.2	0.51	5.9	4.4	5.1	4.1			1
1988	Sep	14	04:07:45.8	207.7	0.93	61.0	5.9	6.1	4.8			2
1988	Dec	17	04:25:55.8	215.9	1.11	40.9	5.8	5.9	4.7	60	7.47	3
1989	Jan	22	04:04:54.9	262.4	0.86	64.4	6.0	6.0	4.7	52	7.45	3
1989	Feb	12	04:22:54.7	276.1	0.99	83.1	6.0	5.8	4.8	50	7.60	3

1: Single station of GERESS site investigation
2: Single station of GERESS site investigation; Joint Verification Experiment: yield 150 kT
3: GERESS test array (9 stations)

Table 2-10: Magnitude Yield Relations for Kazakhstan from
6 Events Recorded at the GERESS Site 1988-1989

Yr	Mo	Day	Rem	m_b GRF	Yield GRF	m_b GERESS	Yield Nuttli	Yield Ringdal	Yield Ekström
1988	May	4		6.0	150	6.0	147	132	127
1988	Jun	14		4.6	10	4.4		4	7
1988	Sep	14	JVE	6.0	149	5.9	108	108	119
1988	Dec	17		5.7	71	5.8	80	68	131
1989	Jan	22		6.0	120	6.0	147	118	111
1989	Feb	12		5.8	90	6.0	147	63	88

The yields of column Nuttli were calculated using his 1986 paper and GERESS magnitudes. Yields in columns Ringdal are from Ringdal et al. (1992), and Ekström from Ekström and Richards (1994).
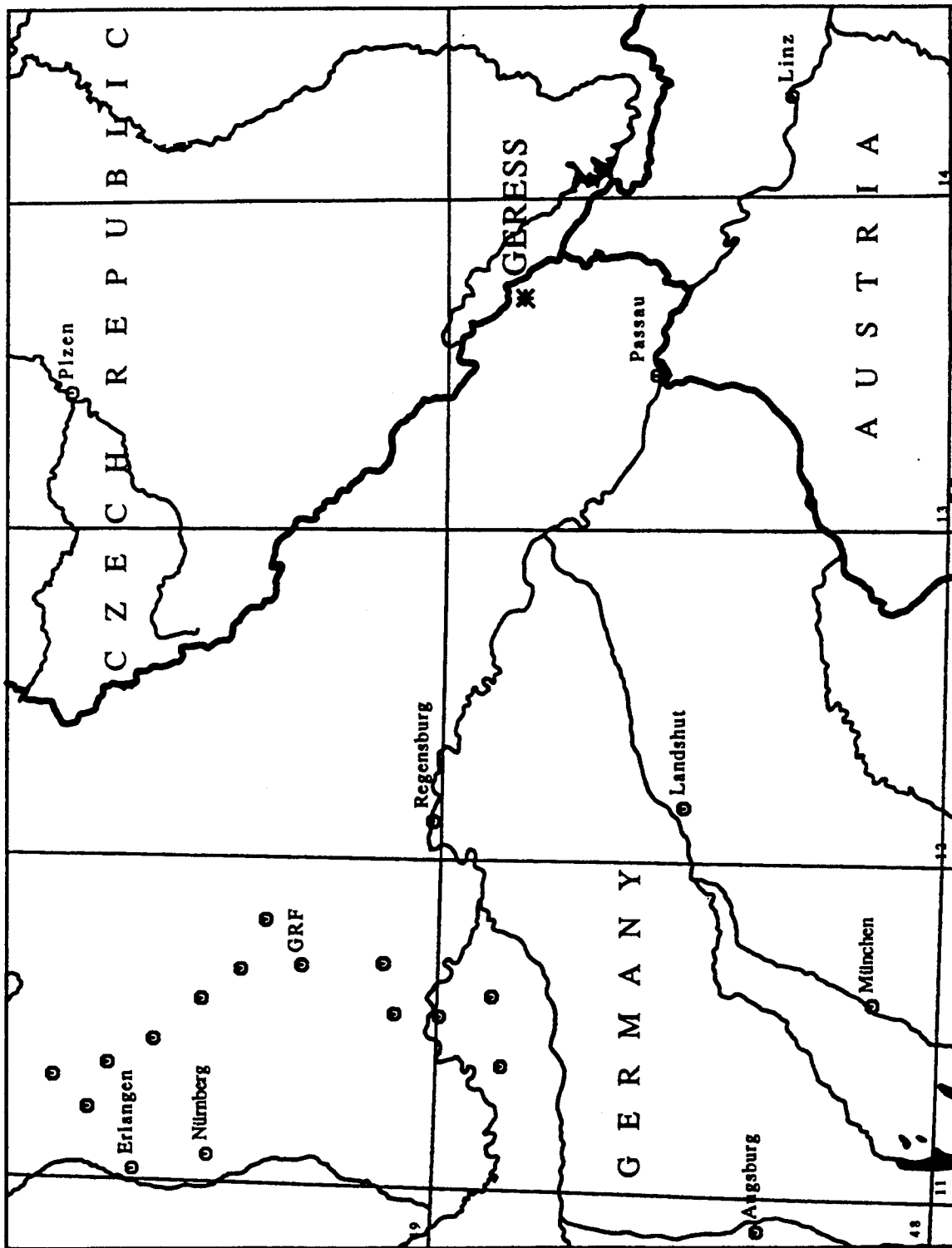
Figure 2-1: Location of the GERESS array.
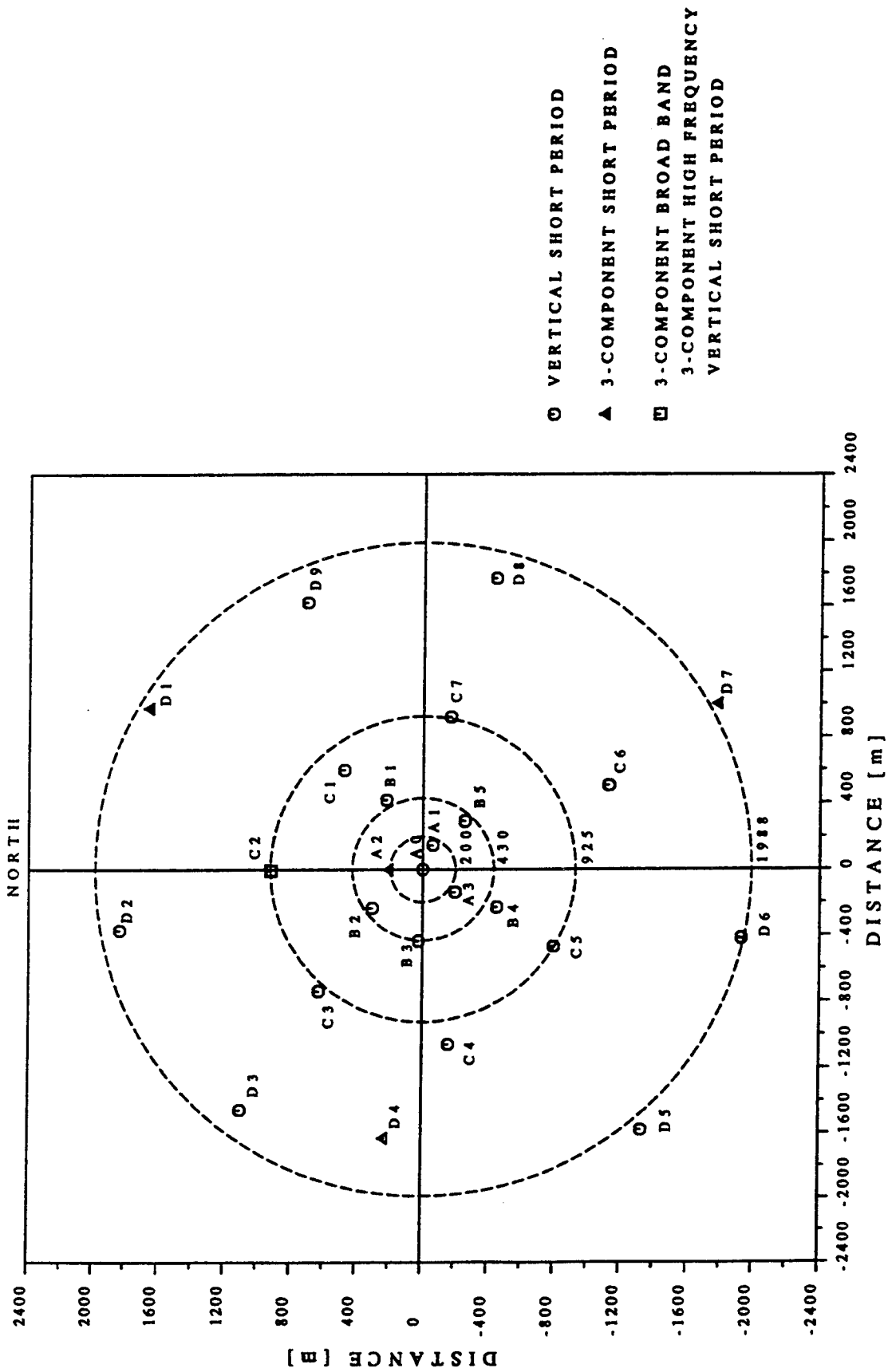
Figure 2-2: Geometry of the GERESS array.

⊕ VERTICAL SHORT PERIOD

▲ 3-COMPONENT SHORT PERIOD

⊡ 3-COMPONENT BROAD BAND
3-COMPONENT HIGH FREQUENCY
VERTICAL SHORT PERIOD
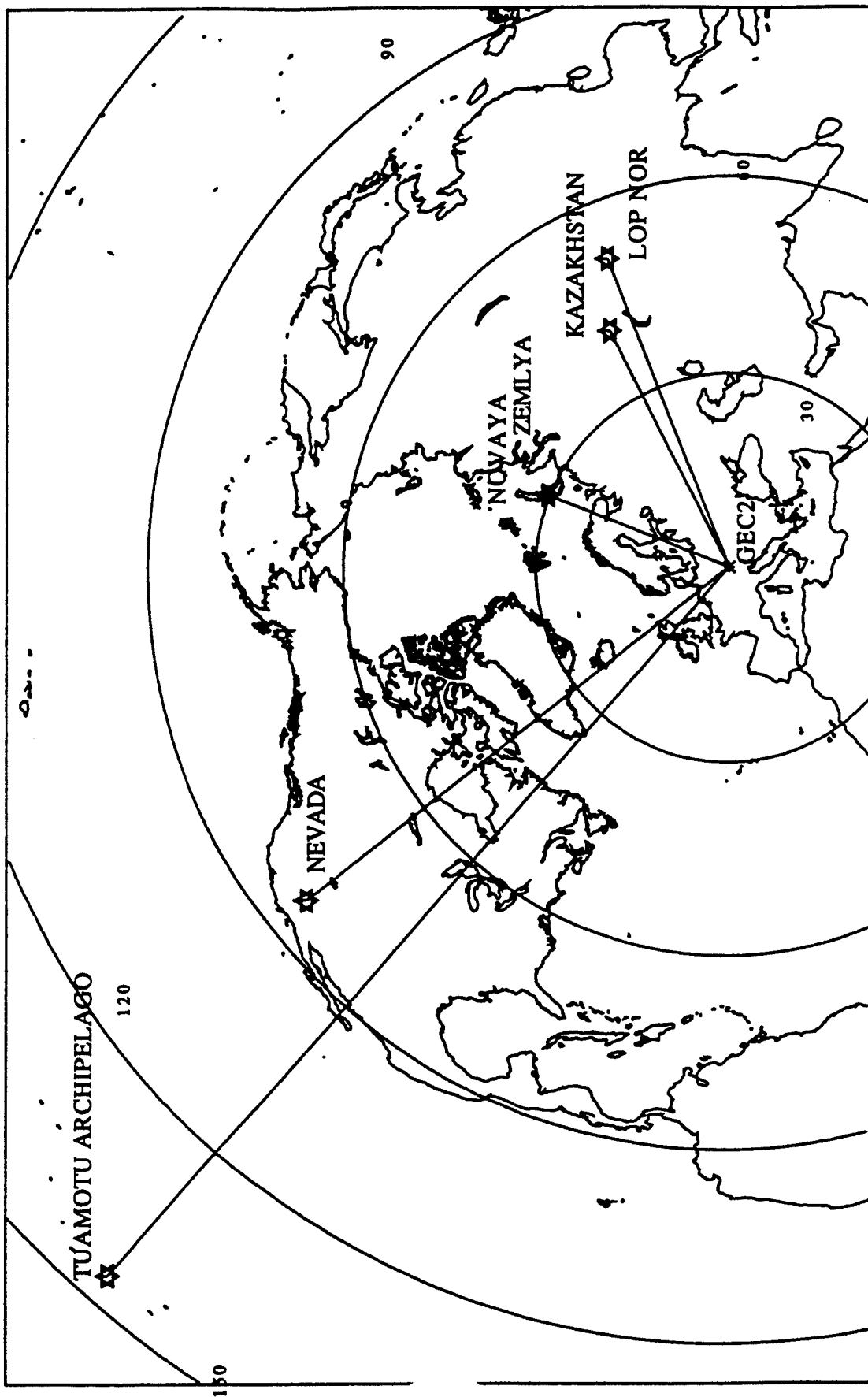
Figure 2-3: Location of the nuclear test sites monitored at GERESS (1988 - June 1994).
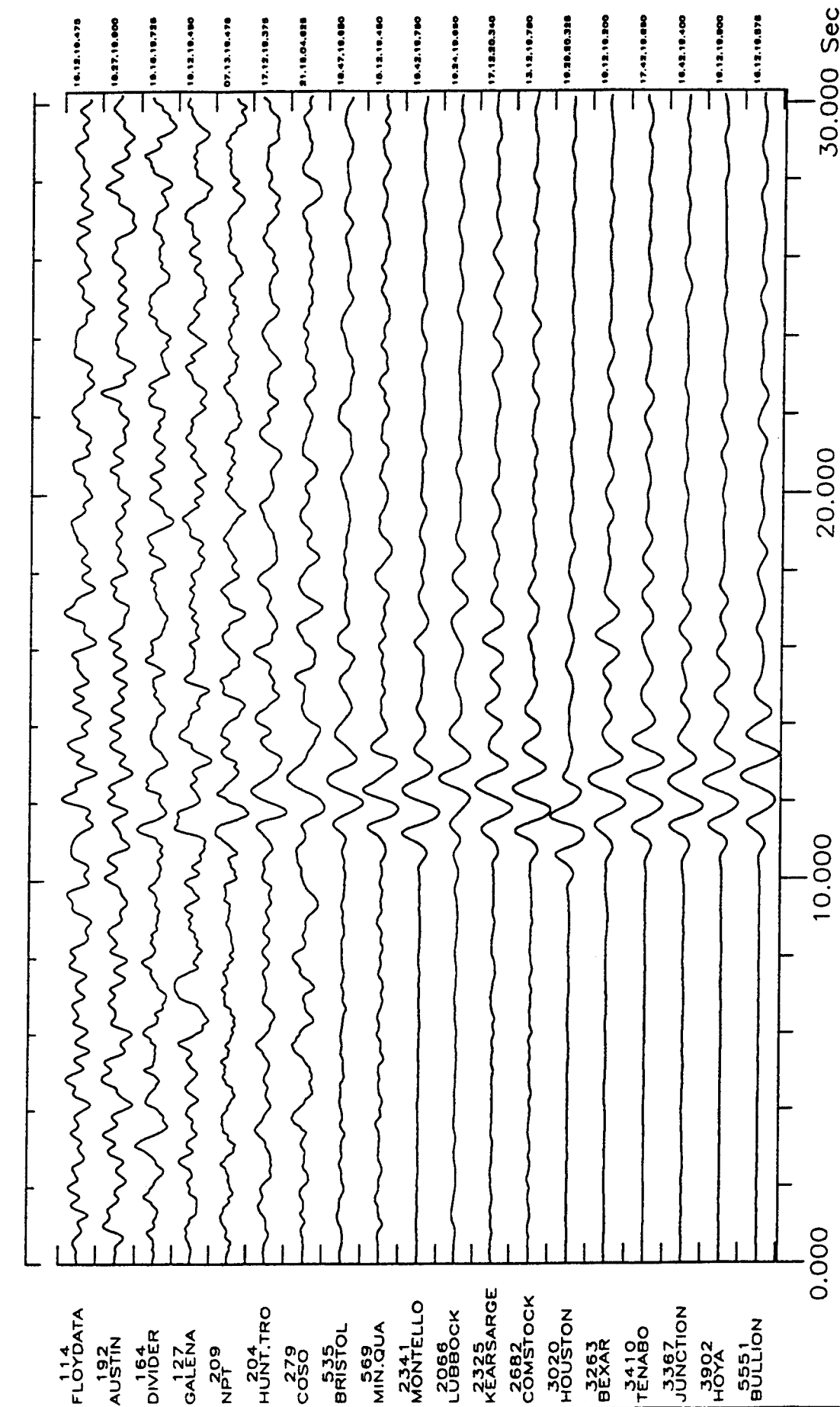
Figure 2-4: Optimum GERESS beams (filtered 0.5 - 2.5 Hz) of events at Nevada test site (1990-1993), sorted according to magnitude determined at GERESS (Table 2-2). For the 2 events in 1988, single traces are shown. All traces start 10 seconds before the theoretical onset time calculated from the published DOE parameters and the IASP91 travel time tables.

38

80.3 FLOYDATA
108 AUSTIN
124 DIVIDER
96.9 GALENA
167 NPT
175 HUNT.TRO
174 COSO
415 BRISTOL
519 MIN.QUA
2052 MONTELLO
1669 LUBBOCK
2025 KEARSARGE
2420 COMSTOCK
2630 HOUSTON
2811 BEXAR
3212 TENABO
2771 JUNCTION
3361 HOYA
5201 BULLION

0.000   10.000   20.000   30.000 Sec
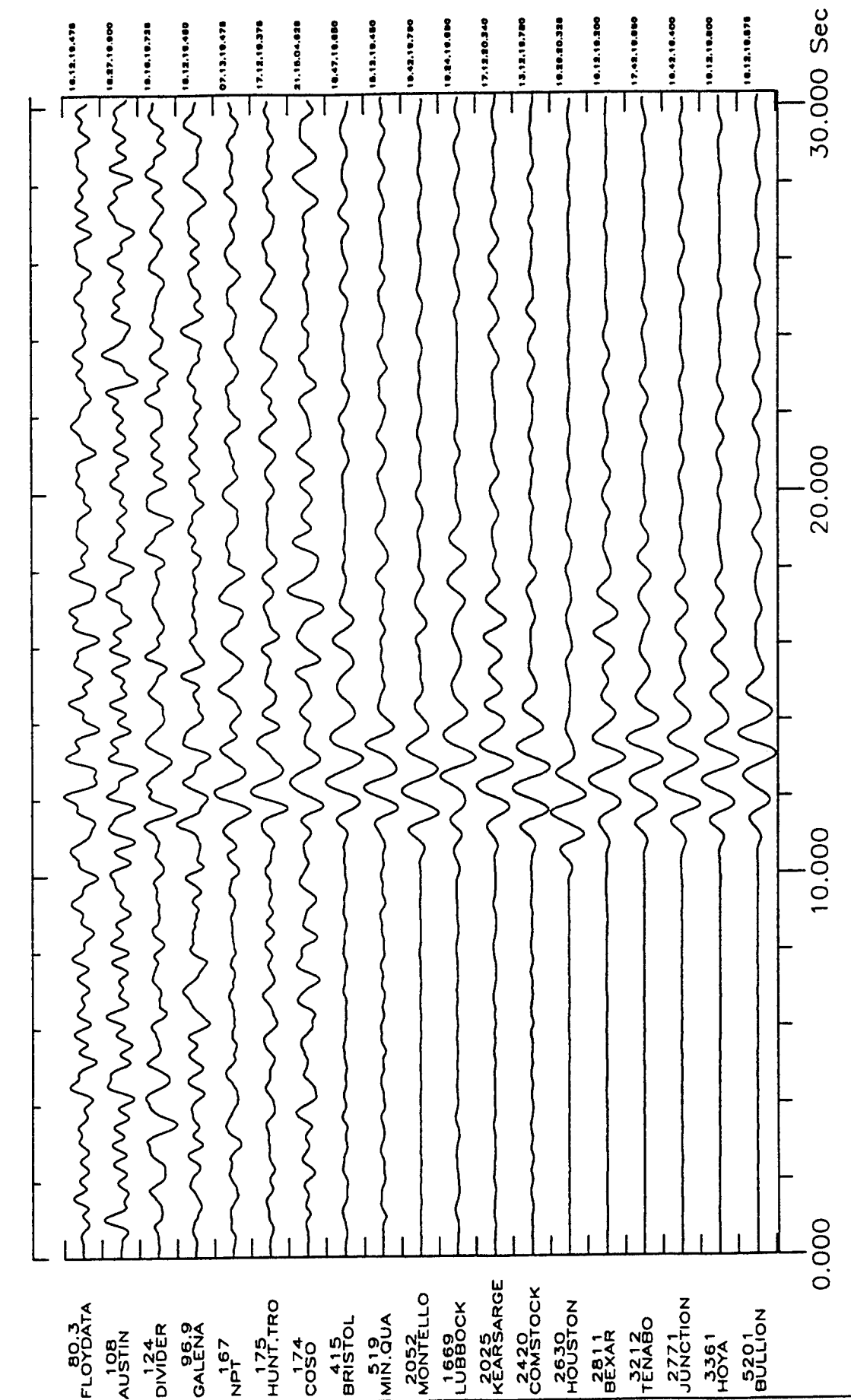
Figure 2-5: Same as Fig. 2-4, except filter: 0.7 - 2.0 Hz.
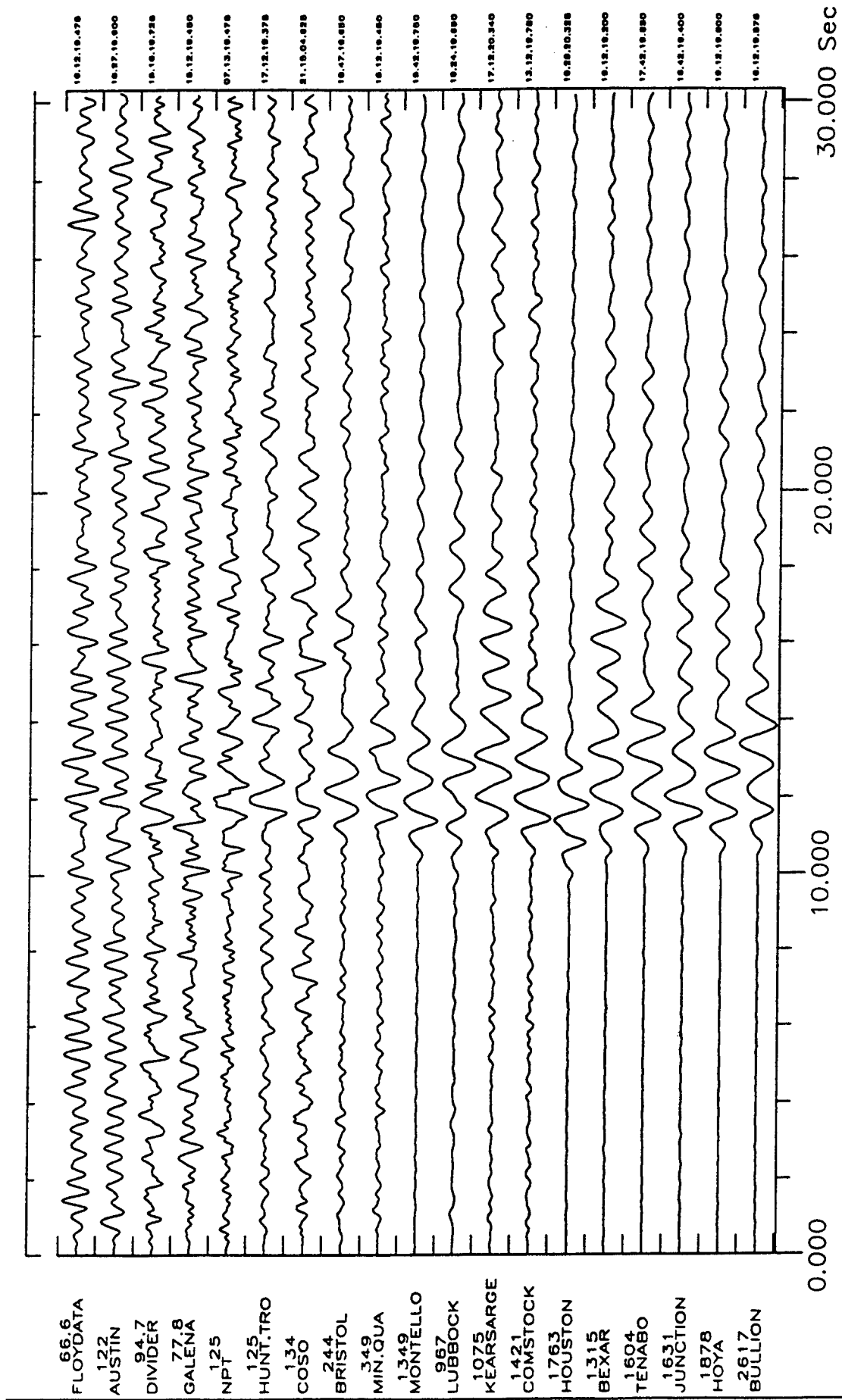
Figure 2-6: Same as Fig. 2-4, except filter: 1.0 - 3.0 Hz.

Figure 2-7: Correlation matrix of the events from Nevada test site (for event numbers, see Table 2-3).
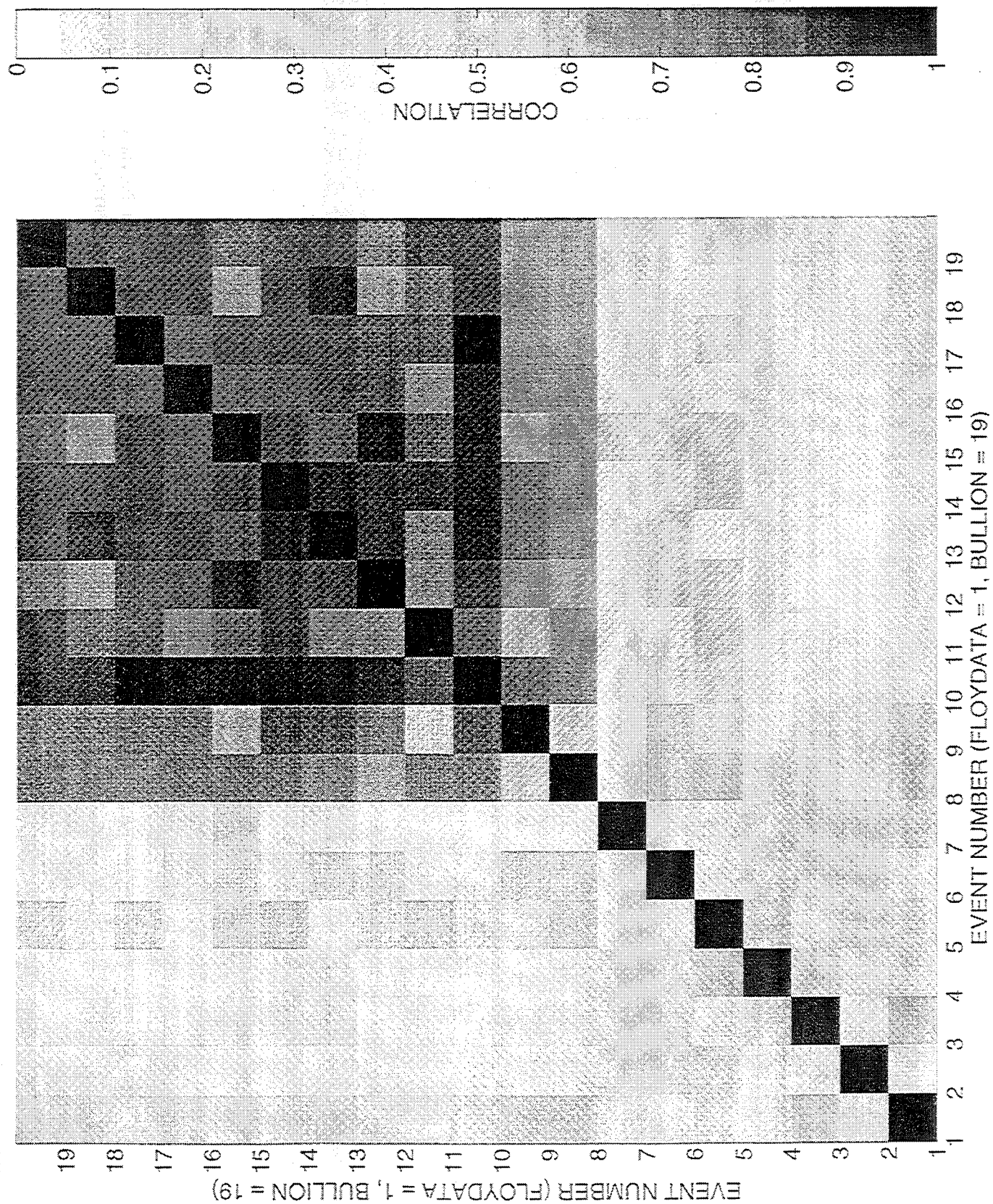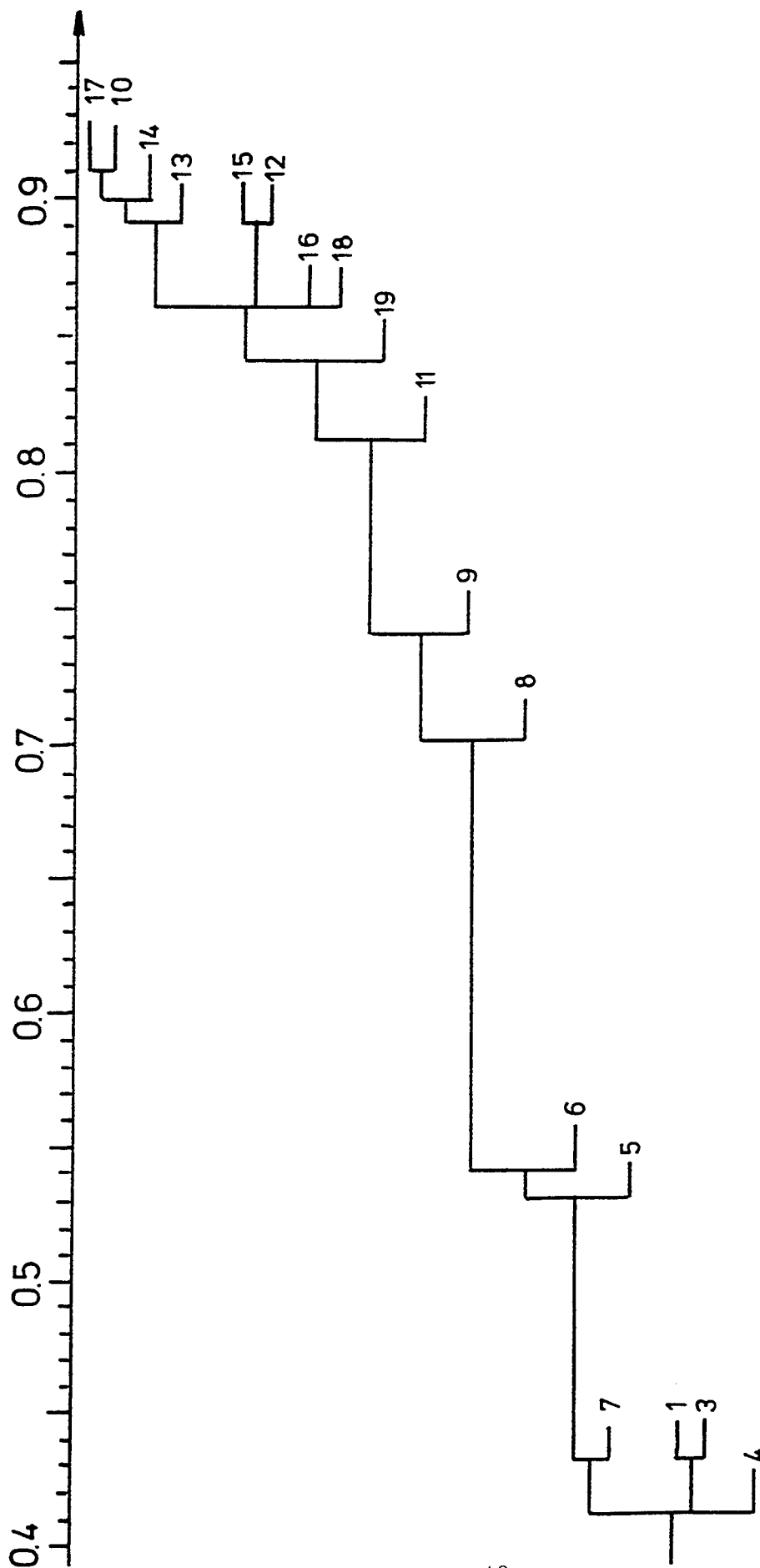
Figure 2-8: Single linkage clustering dendrogram of the events from Nevada test site (for event numbers, see Table 2-3). Note that the correlation coefficient is only 0.34 for event 2.
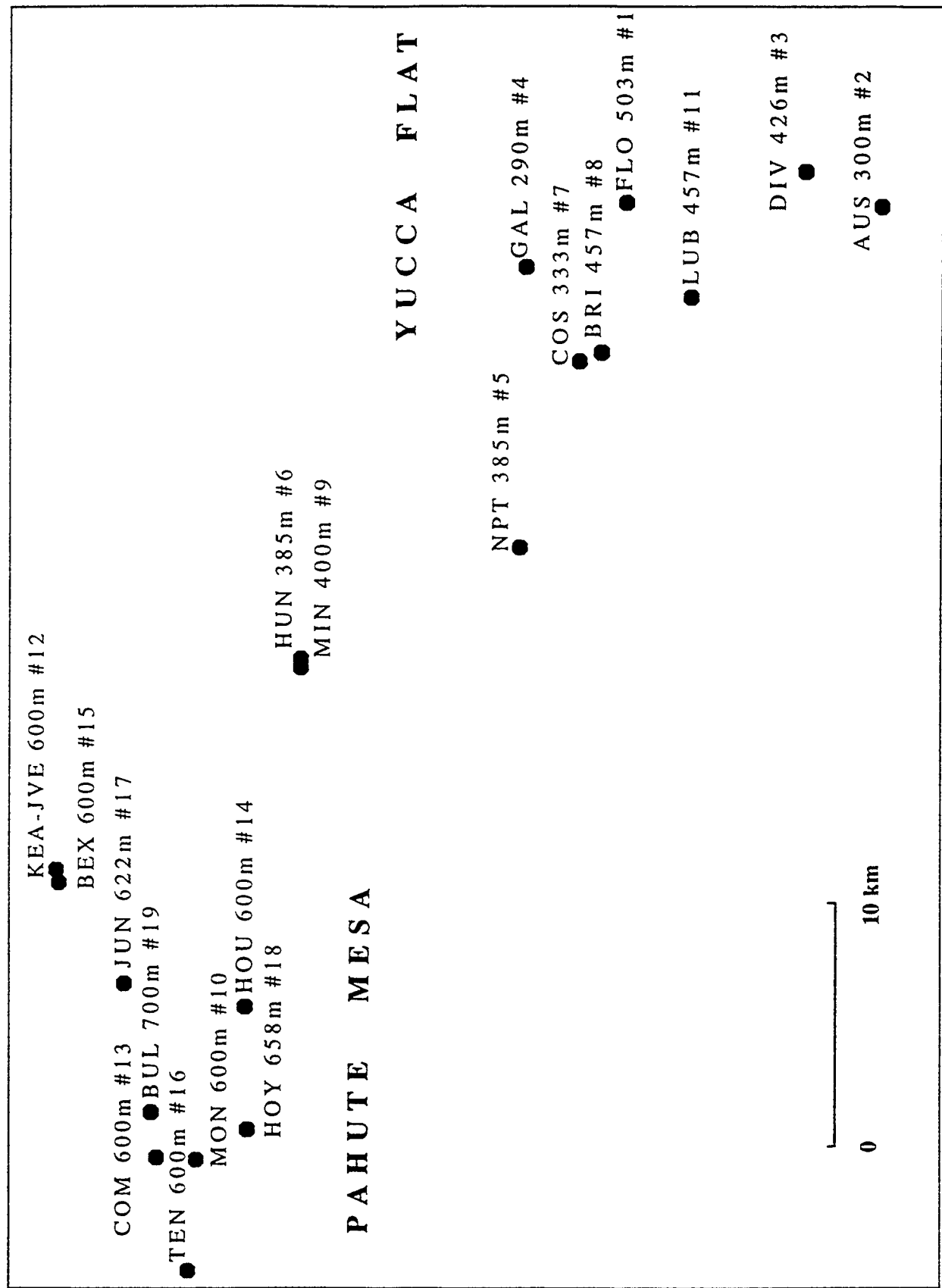
Figure 2-9: Map of event locations at Nevada test site (using DOE informations, NEIC).
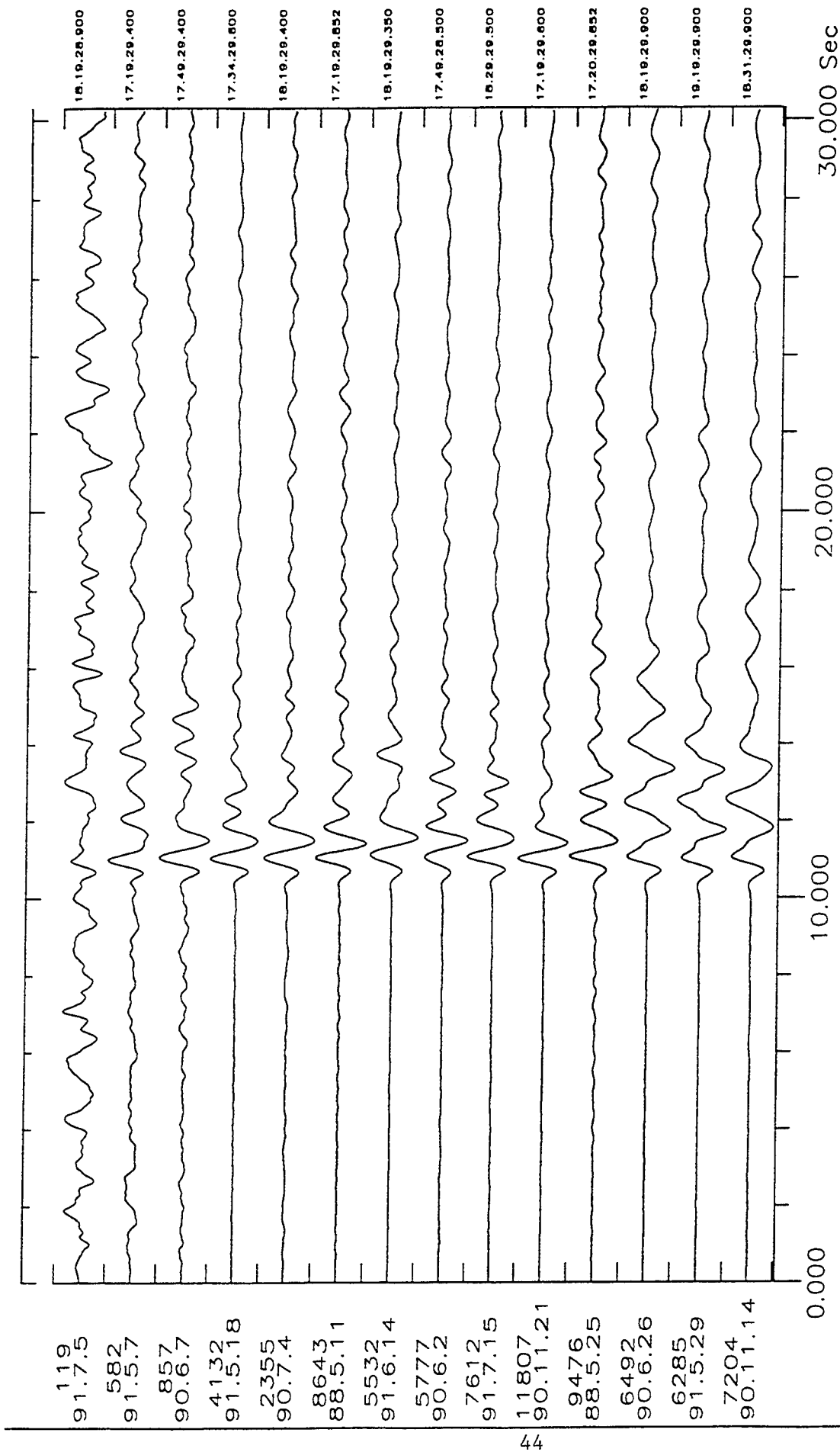
Figure 2-10: Optimum GERESS beams (filtered 0.5 - 2.5 Hz) of events at Tuamotu Archipelago in 1990-1991 (Tables 2-4 and 2-5). For the 2 events in 1988, single traces are shown. All events were sorted according to yield esti-mate. The trace of the event on Nov. 14, 1990 starts 10 seconds before the measured onset time, the other traces were aligned to its first minimum (the start time of each trace is indicated to the right).

44
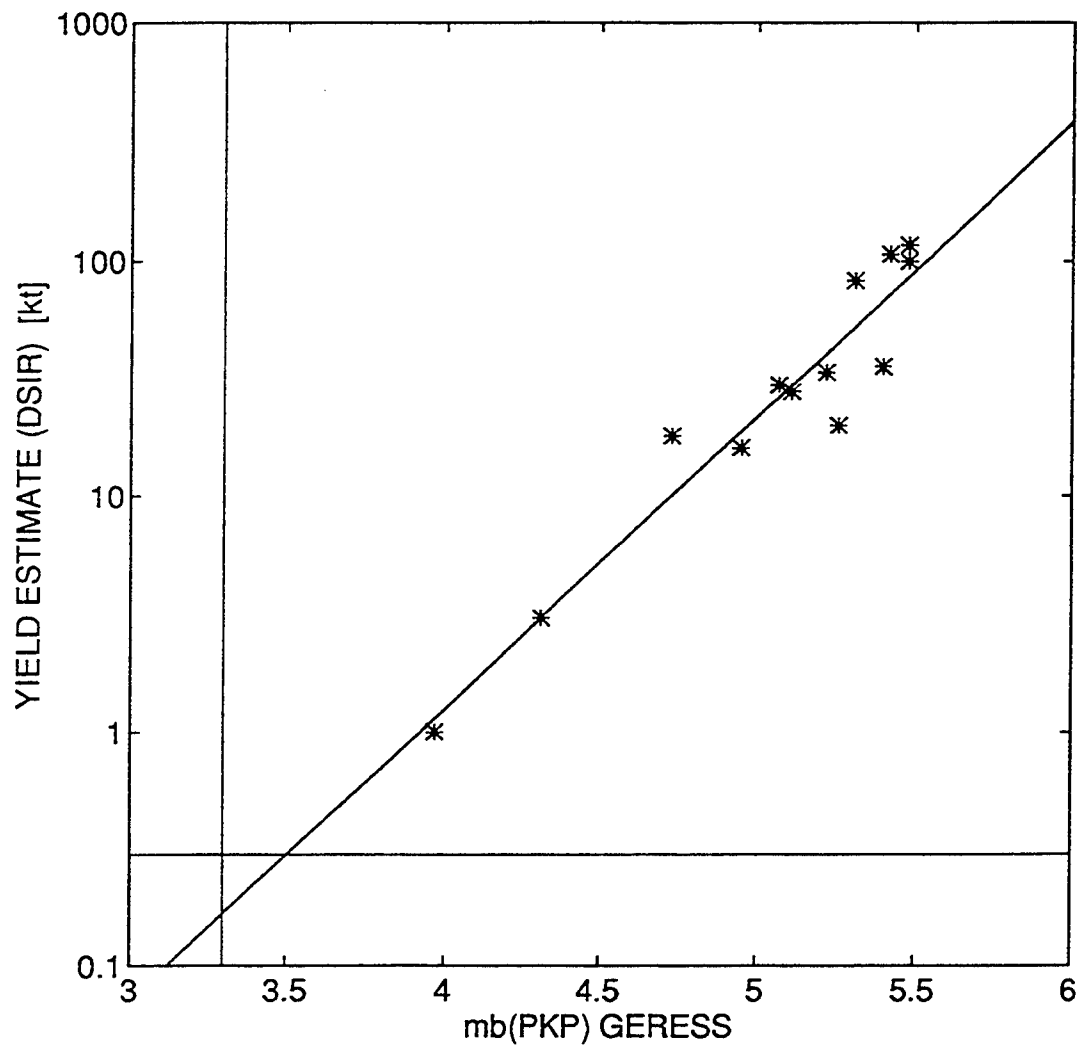
Figure 2-11: Relation of $m_b(\text{PKP}_{\text{GERESS}})$ versus estimated yield for events at Tuamotu Archipelago.
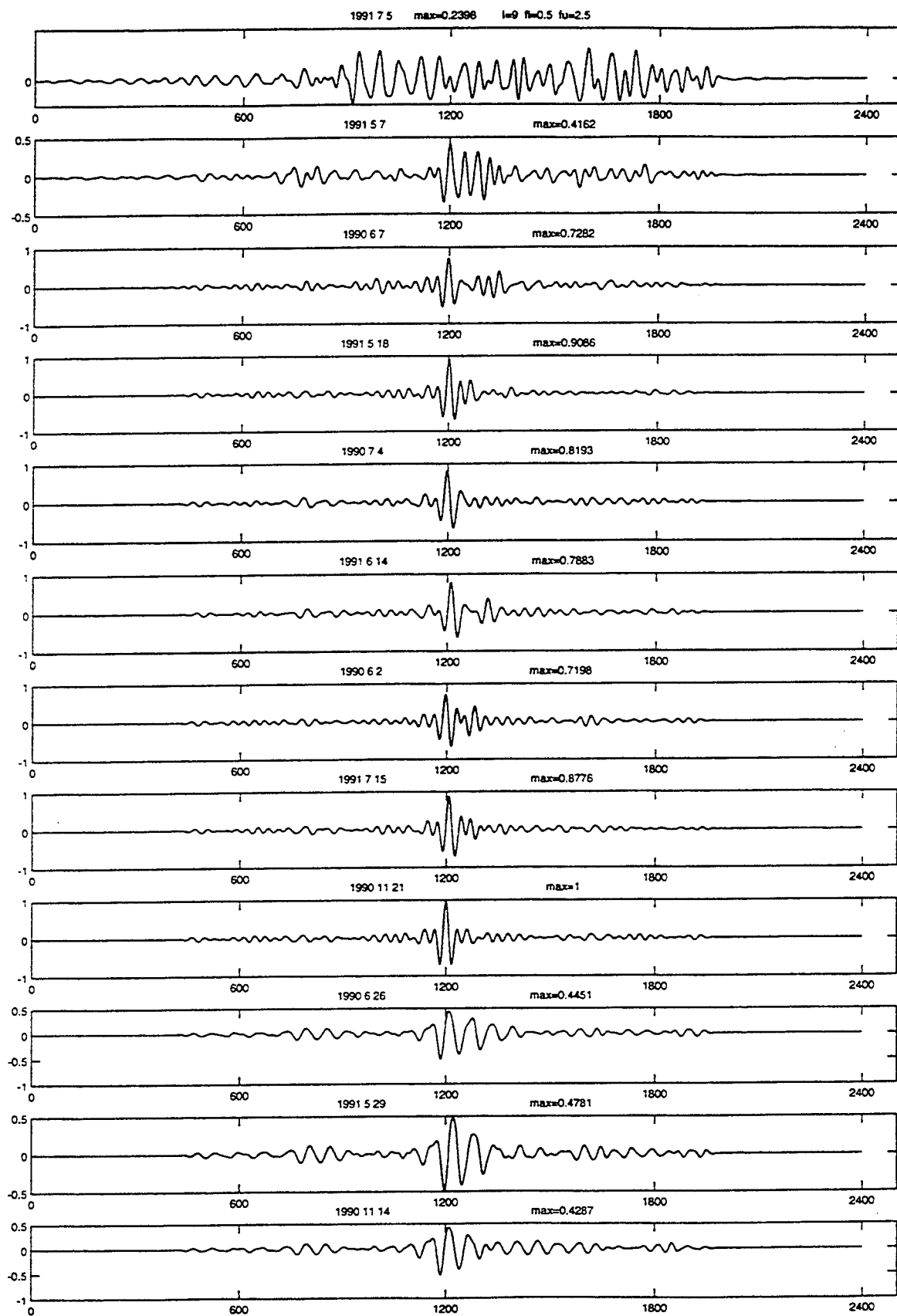
Figure 2-12: Cross-correlation sequence of the optimum beam for the event on
Nov. 21, 1990 in the Tuamotu Archipelago with the optimum beams of all
other events (1990-1991).

46

Figure 2-13: Correlation matrix of the events from Tuamotu Archipelago (for event numbers, see Table 2-5).
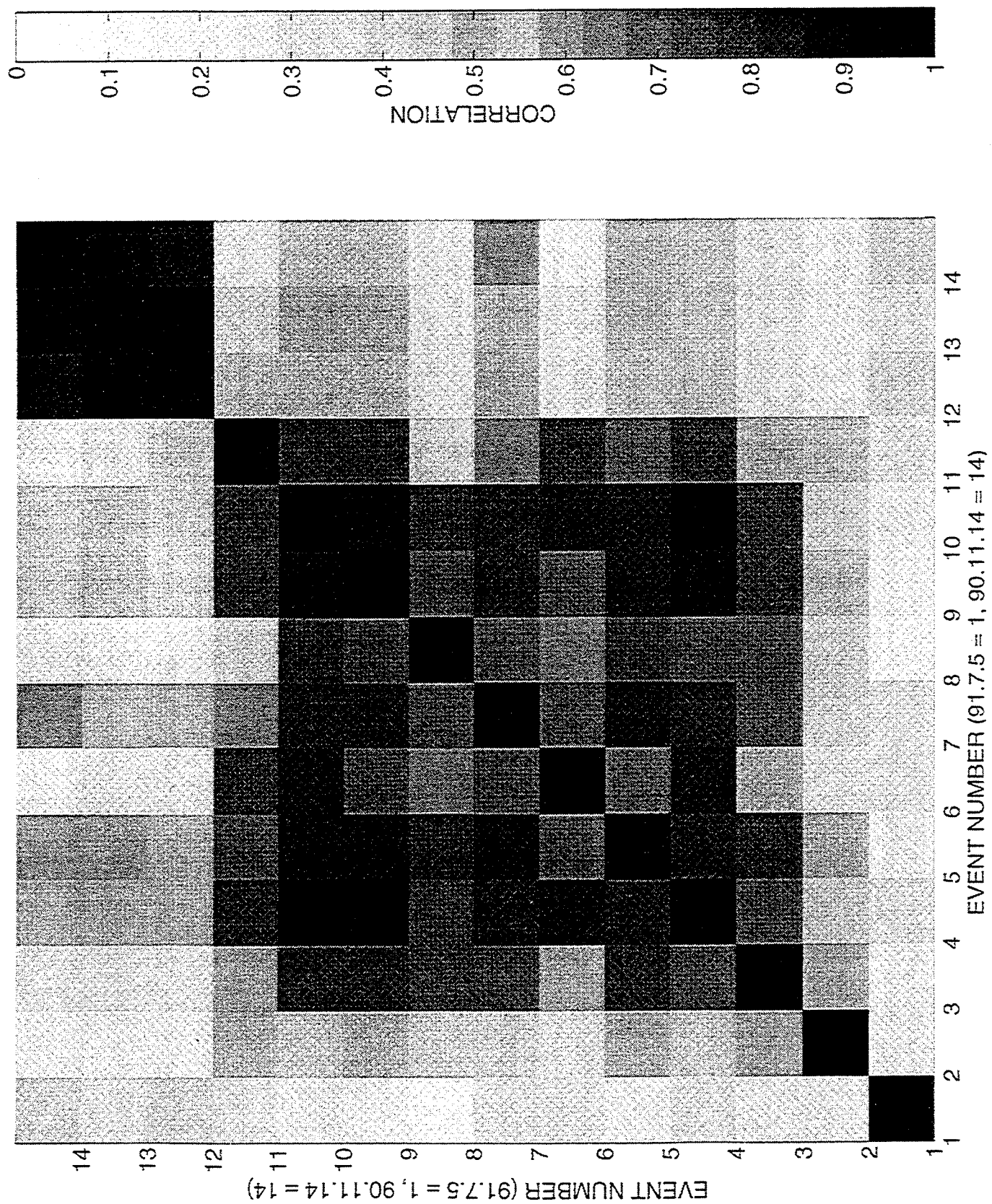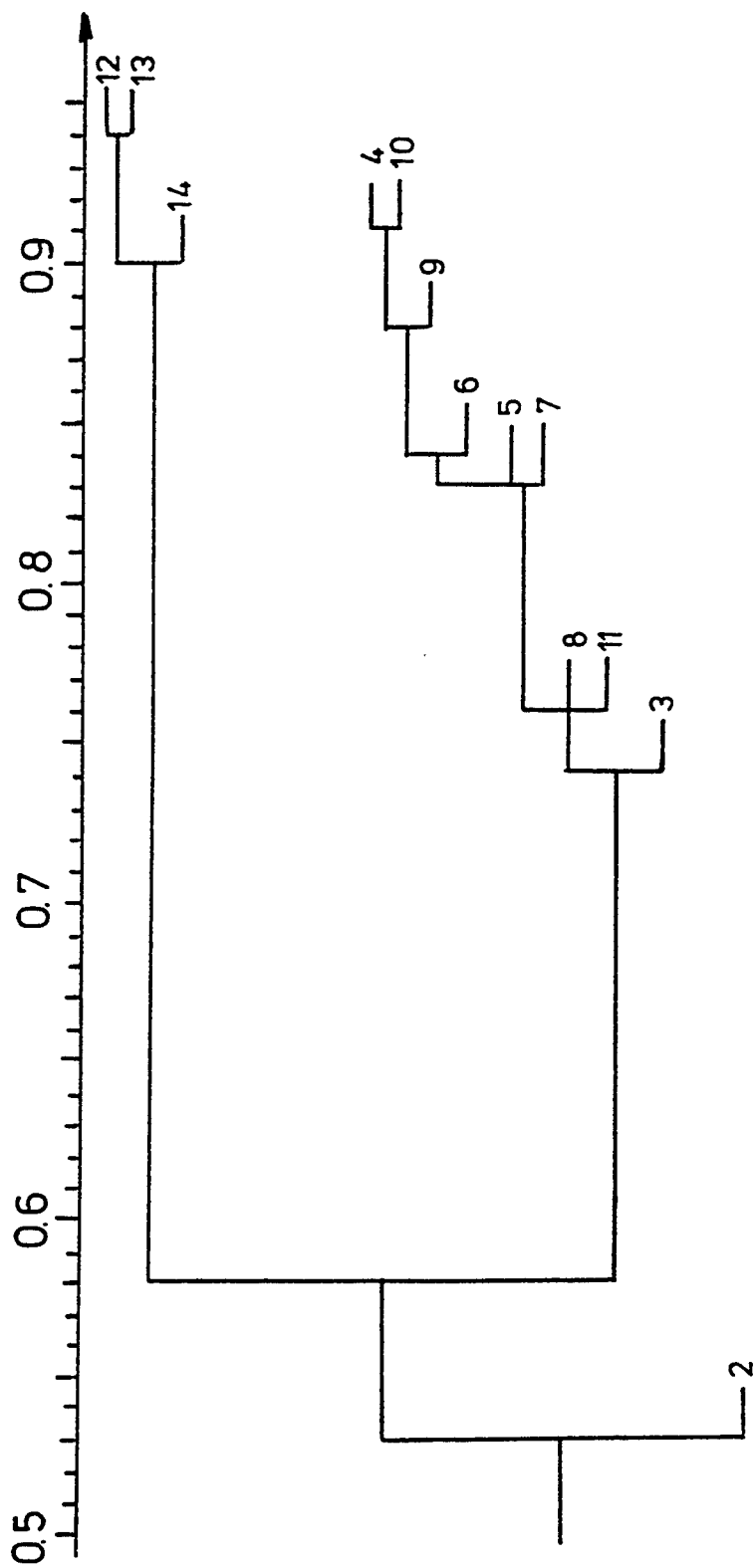
Figure 2-14: Single linkage clustering dendrogram of the events from Tuamotu Archipelago (for event numbers, see Table 2-5).

48
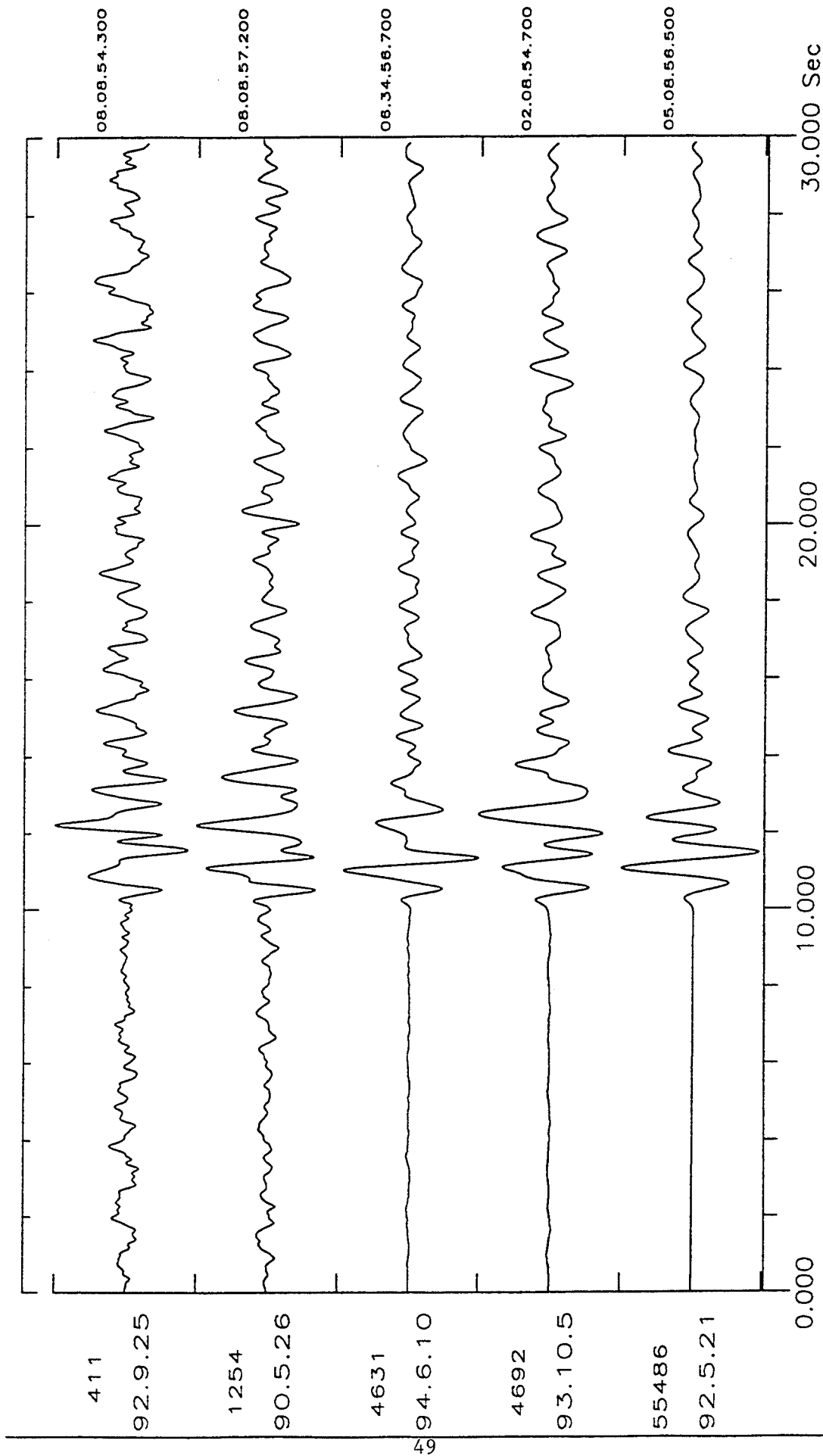
Figure 2-15: Optimum GERESS beams (filtered 0.5 - 2.5 Hz) of events at Lop Nor, sorted according to magnitude determined at GERESS (Table 2-7). The trace of the event in 1993 starts 10 seconds before the measured onset time, the other traces were aligned to its first maximum (the start time of each trace is indicated to the right).
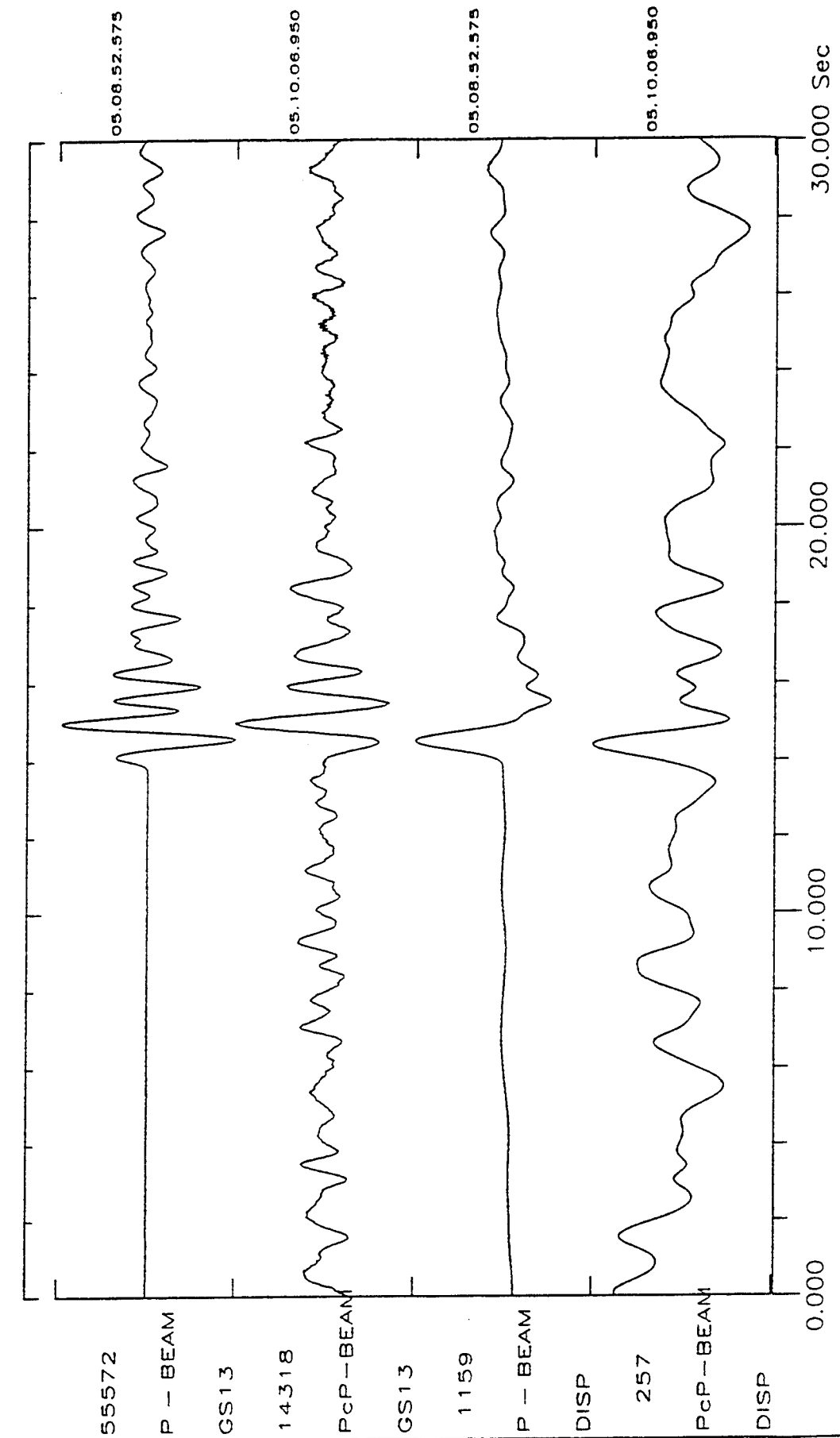
Figure 2-16: Unfiltered beams of P and PcP from the Lop Nor event on May 21, 1992 (top) and the corresponding true ground motion simulations (bottom).

50
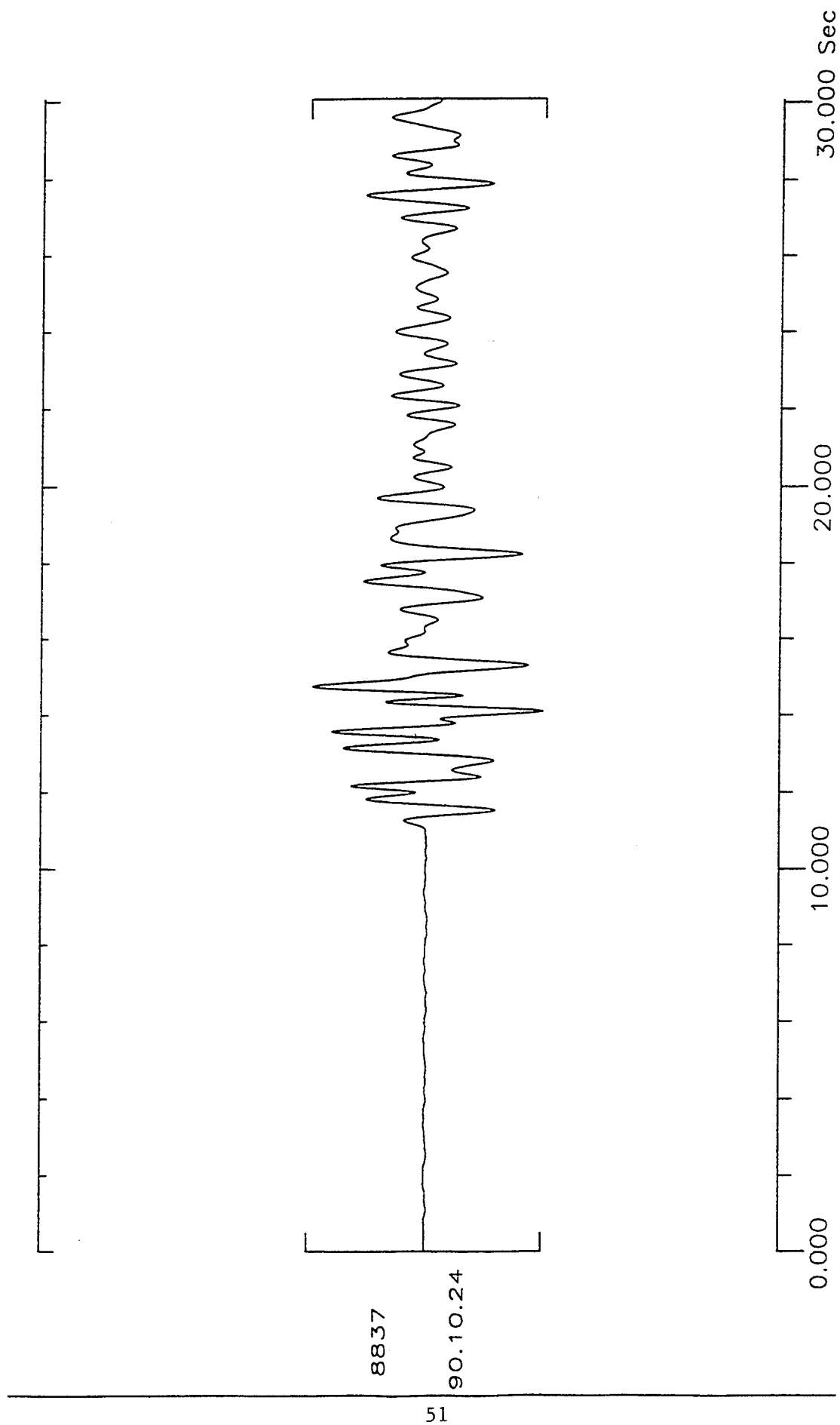
Figure 2-17: Optimum GERESS beam (filtered 0.5 - 2.5 Hz) of the 1990 event on Novaya Zemlya (Table 2-8). The trace starts at 15:04:04.0.

8837

90.10.24

0.000 10.000 20.000 30.000 Sec
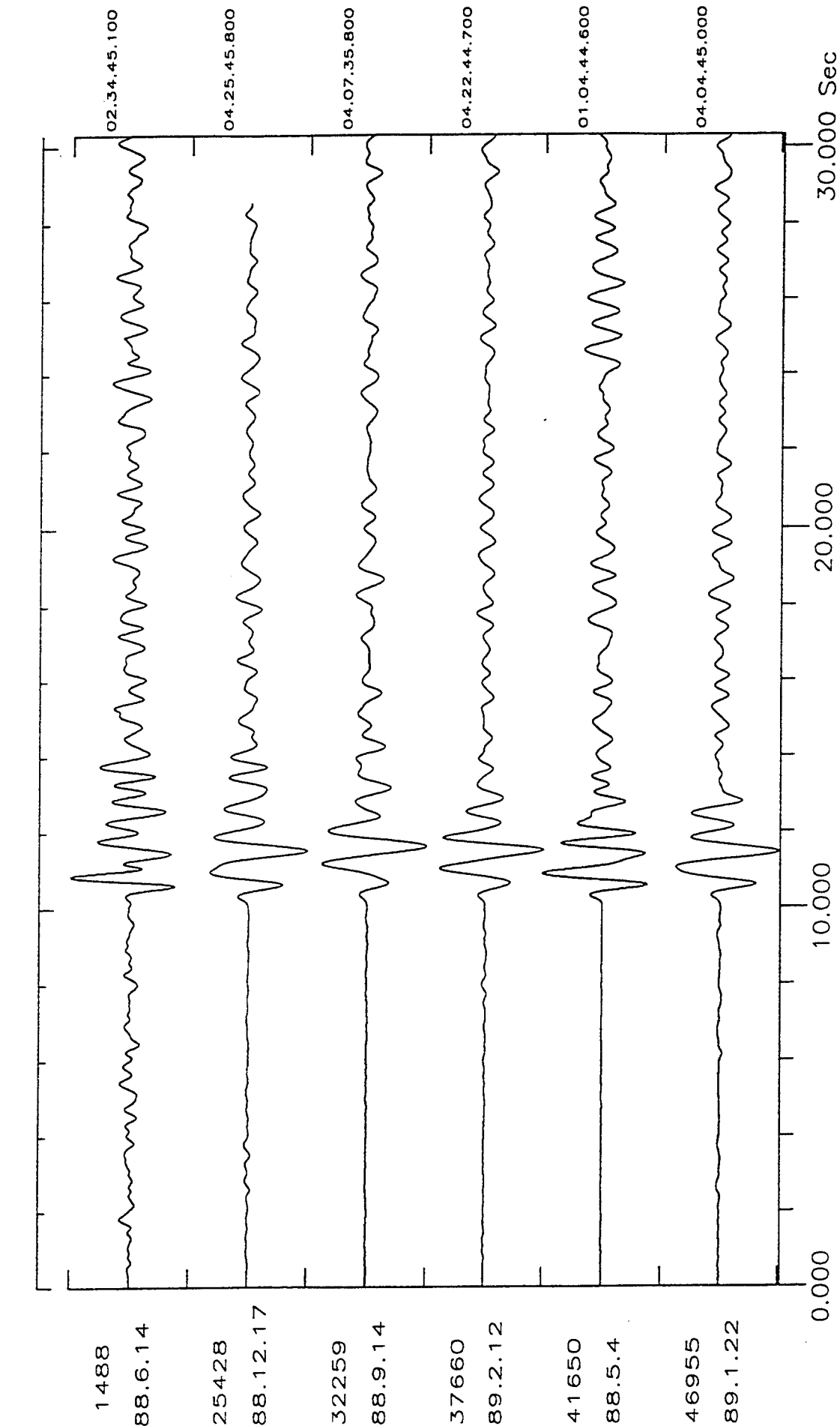
Figure 2-18: Single traces (events before Dec. 1988) and optimum beams of the GERESS test array (filtered 0.5 - 2.5 Hz) for events at Kazakhstan test site, sorted according to magnitude determined at the GERESS site (Table 2-9). The trace of the event on May 4, 1988 starts 10 seconds before the measured onset time, the other traces were aligned to its first maximum (the start time of each trace is indicated to the right).

52

3. P-WAVE ARRAY POLARIZATION ANALYSIS AND EFFECTIVE ANISOTROPY OF THE BRITTLE CRUST[*]

G. H.R. Bokelmann

3.0 ABSTRACT

P-wave polarization constrains local anisotropy in the vicinity of the receivers. Using three-component and array data from the regional GERESS array in Southeastern Germany, we measure polarization **a** and propagation vectors **s** for P-phases of 120 events. Angular deviations **a-s** between these normalized vectors often approach 10°, rendering them easily measurable. The effect of anisotropy can be distinguished from remote effects, since all remote effects such as source mislocation, distant lateral heterogeneity or distant anisotropy affect polarization and propagation vectors simultaneously. Averaging removes sensitivity to near-receiver heterogeneity, and local anisotropy is left as sole cause of the effects in **a-s**. This method hence gives local effective anisotropy in the near-receiver crust averaging over a depth interval of a wavelength ($\approx 6km$). We resolve strike and dip of the symetry plane and also two dimensionless numbers η and τ which give constraints on four of the elastic parameters. The optimum model (variance reduction 44%) has symetry plane orientation of strike 113° and dip 49° to the North, which corresponds closely to the consistently observed gneiss foliation direction in the area (120°, 50°-60°). Comparing η and τ with predictions from different physical models we find that the data are fit by a gneiss model assuming that the anisotropy is dominated by the mica, if 3% to 8% of the mica are well-aligned. This suggests that anisotropy in the region studied is dominated by the effect of local foliation rather than the regional stress field.
Key words: array seismology, wave propagation, polarization, anisotropy, inversion

3.1 INTRODUCTION

In the pioneering study of anisotropy in the Earth Hess (1964) showed that azimuthal travel time delays of oceanic P_n can be explained by aligned olivine crystals in the oceanic upper mantle. For such a phase, which travels subhorizontally on most of its path, Backus (1965) showed that azimuthal travel time variation is characterized by a rather simple trigonometric expression, given that anisotropy is weak. Fitting of such trigonometric terms has subsequently been used for teleseismic P-waves, f.e. in Dziewonski and

---

[*]submitted to Geophysical Journal International

Anderson (1983). Interpretation of such data, however, is complicated by the fact that lateral heterogeneity can also cause azimuthal variation. This trade-off is often difficult to resolve from travel time data alone. The second type of "classical" anisotropy studies is shear-wave splitting (Ando, Ishikawa and Yamazaki, 1983; Silver and Chan, 1991), a technique which uses the strong effect of anisotropy on waveforms of shear-waves due to different speed of the two orthogonally polarized shear-waves. The constraint on anisotropy is not unlike that of travel times. Both give integral constraints only, namely on bulk anisotropy along the wave path. Hence, for both methods a tradeoff exists between size of anisotropy and extent of anisotropic path. More importantly, an anisotropic region is difficult to localize using these data. For example, mantle anisotropy can be inferred from shear-wave splitting data only if observed effects are too large to be explained by crustal anisotropy alone. This is somewhat unsatisfying, and methods for independent determination of anisotropy in the crust under the receivers should be sought. This paper, in fact, demonstrates that beside active experiments an entirely independent constraint on near-receiver anisotropy is possible; in this case it follows from analysis of three-component array data.

Anisotropy studies using travel times and shear-wave splitting can be performed with single-station data, in the later case requiring a three-component instrument. For the present study of P-wave phases, we use array and three-component data from the GERESS array. These array data allow determination of the propagation vector $\mathbf{s} = \mathbf{k}/\omega$ of plane waves crossing the array. While this particular feature of beamforming is well-appreciated for signal enhancement, event detection and localization (Beauchamp, 1975), this particular strength has apparently not been used in anisotropy studies so far.

The propagation vector, given by $\mathbf{s} = \nabla t$, may be specified by azimuth θ_s and horizontal slowness $p = \sqrt{s_x^2 + s_y^2}$ or alternatively incidence angle $\phi_s = sin^{-1}(pv)$ with the local velocity v. On the other hand, three-component stations allow determination of the polarization vector $\mathbf{a}$, which gives the dominant direction of linear particle motion. $\mathbf{a}$ can be specified by azimuth θ_a and incidence angle ϕ_a. In the following we restrict our intention to normalized $\mathbf{s}$ and $\mathbf{a}$, namely to azimuth and incidence angles. This effectively ignores that the array also gives estimates of the true or apparent velocity. Neither of the two azimuth estimates θ_s and θ_a necessarily correspond to the azimuth of the receiver-source great circle, since heterogeneity, anisotropy and other effects may cause deviations. The same is true for the incidence angles. For known source location we get predictions (θ_p, ϕ_p) for a reference Earth model. Comparing (θ_s, ϕ_s) and (θ_a, ϕ_a) with the predictions gives rise to so-called mislocation diagrams. For the purpose of event localization the two data types and correspondingly their mislocation patterns are typically treated the same, where the azimuth is used for localization purposes, while the incidence angle serves for identification of the phase for regional events and epicentral distance in the case of teleseismic events.

Interestingly, source location procedures have so far disregarded that these

two observed quantities, namely propagation and polarization vectors, are principally different. While they coincide in an isotropic Earth, elastic anisotropy in the Earth would affect propagation and polarization vectors differently. For event localization, this means that there is a systematic bias between propagation and polarization vectors, which should be removed by taking local anisotropy into account. This systematic bias, however, is the prime quantity of interest in this study, since it offers us a new constraint on anisotropy in the vicinity of the receivers (in fact exclusively there). In this study we use polarization and propagation vectors exclusively. Travel time and amplitude information is not used, since that might obscure the near-receiver crustal anisotropy with information gathered somewhere along the ray paths.

3.2 OBSERVATIONS

3.2.1 GERESS Array

The GERman Experimental Seismic System GERESS (Harjes, 1990), shown in figure 3.1, is a regional seismological array with aperture of about 4 km consisting of 25 stations with 1 Hz vertical short-period instruments (Geotech GS-13) sampled at 40 Hz, with 4 of them also equipped with horizontal components (A2,D1,D4,D7; triangles). Additional three-component instruments at the C2 location are sampled at 120 Hz (Geotech GS-13) and 10 Hz (Geotech BB-13). For further descriptions of installation criteria, performance and operation see Harjes (1990) and Harjes et al. (1993). The array is located in Eastern Bavaria, Germany, in a hilly region on crystalline outcrop of the Bohemian massive. The topographic variation across the array is about 200 meters. A major advantage of data from the GERESS array is that there are no sediments under the stations, greatly improving the quality particularly of the polarization data. Otherwise P-S conversions at the crust-sediment boundary might disturb polarizations substantially.

3.2.2 Events

This study uses a set of 95 events recorded at GERESS array stations in the time interval between May 1990 and January 1993 (table 3.1). These events comprise the whole range from regional to teleseismic distance. The emphasis in this study is on first-arriving phases. Only the later-arriving phase PcP is included in three cases. Table 3.1 is part of a larger set of events. For the events not included in the table either the polarization or propagation vector had to be discarded, which was the case particularly often early in the experiment. In general, events were discarded if data from less than 3 three-component stations or 9 array stations were available. Out of 112 events with acceptable polarization data, 81 had data for all 6 three-component instruments present. Out of 108 events with acceptable propagation data, 88 had data from at least 20 array stations.

Next we discuss procedures of extracting backazimuth and incidence angle

information from three-component and array data.

3.2.3 Determination of Polarization Directions

For three-component data $\mathbf{u}^j = (u_i)^j$ with components $j = 1,2,3$, the covariance matrix at zero-lag is computed as

$$S_{jk} = \frac{1}{N} \sum_{i=1}^{N} u_i{}^j u_i{}^k \tag{1}$$

where N is the number of samples in the time window. Obviously, S is symmetric, so that its eigenvalues λ^j are real and nonnegative. We choose a set of 3 orthonormal eigenvectors $\mathbf{a}^j$. $\lambda^j \mathbf{a}^j$ (no summation) then gives the axis of the polarization ellipsoid (see f.e. Kanasewich, 1981). If the particle motion is linearly polarized, then $\lambda^2 = \lambda^3 = 0$. For elliptical particle motion (within a polarization plane), we have $\lambda^3 = 0$. In general, however, the particle motion is ellipsoidal due to presence of different types of noise. If we take components $(1,2,3)$ as (Vertical up, North, East), the incidence angle is $\Phi_a = cos^{-1}|u_1{}^1|$ and the backazimuth is

$$\phi_a = \begin{cases} tan^{-1}(\frac{a_3{}^1}{a_2{}^1}) & \text{for } a_1{}^1 < 0 \\ \pi + tan^{-1}(\frac{a_3{}^1}{a_2{}^1}) & \text{for } a_1{}^1 \geq 0 \end{cases}$$

A simple check of the quality of the measurement is given by the rectilinearity

$$1 - \frac{\lambda^2 + \lambda^3}{2\lambda^1} \tag{2}$$

which is equal to 1 for linear polarization and 0 in the worst case of "spherical" polarization, when all eigenvalues have the same size.

Figure 3.2 shows a seismogram example demonstrating a few characteristics of the eigenvector analysis. For this data example (year 1992 day 48 hour 19) with an epicentral distance of 385km and backazimuth of 235° a number of regional phases are visible. The main phases for this distance range are P_n, P_g, S_n and S_g. They are visible in the three-component seismogram on the top. The lower traces give polarization attributes computed using a gliding window with a length of 2 seconds: The root-mean-square amplitude of the three-component seismogram or "three-component size" (fourth trace) $\sqrt{\sum_j \lambda^j} = \sqrt{\sum_j S_{jj}}$ shows P_g, S_n and S_g clearly. The first-arriving P_n shows up with somewhat smaller three-component size, but with the highest rectilinearity (2), with close-to-ideal linear polarization. A line gives the critical rectilinearity level of 0.9. Only P_n and P_g exceed this level. Since the eigenvalues are related to energy, error bars can be obtained from the F-test (see Bokelmann, 1992). S_g shows up with higher rectilinearity than other S phases and also substantial three-component size. The horizontal-vertical ratio (H/V) $\sqrt{\frac{S_2 + S_3}{S_1}}$ and similarly the radial-transverse ratio (R/T)

computed from the elements of the covariance matrix are also indicative of the phase character. The values of H/V=1 and R/T=1 are shown by lines indicating polarization angles near 45°. For the S-phase train H/V shows very clear horizontally polarized phases S_n, S_g and L_g, which also show small values of R/T. This radial-transverse ratio for P phases shows clearly radially polarized energy. In summary, polarization is an important tool for phase identification. In the following we want to use polarization data for the set of P phases. Figure 3.2 shows that polarization attributes for P-phases are relatively slowly varying. In fact, they are also insensitive to the particular choice of window length. On the 6 three-component stations we observe for P_n a backazimuth of $\theta_a = 240.4° \pm 5.5°$ and an incidence angle of $\Phi_a = 44.9° \pm 4.2°$. These angle estimates correspond closely to values extracted manually from hodograms and are near predicted values from the IASP91 Earth model and source locations from table 3.1 ($\theta_p = 235.17°$ and $\Phi_p = 40.02°$).

Typically we have data from six three-component stations available. We computed standard errors simply from the empirical distribution of those values. The average uncertainty for all phases in the study is 3.5° for the incidence angle and 4.9° for the backazimuth, where we used only events with high Signal-to-noise ratio.

A slightly different approach was given by Jurkewicz (1988), who proposed averaging covariance matrices of individual three-component stations before performing the eigenvector analysis to stabilize the estimates.

Polarization analysis lends itself to very efficient semi-automatic processing. Caution is required, however, for phases closely spaced in time, particularly if their amplitudes differ substantially. For regional phases this case is not uncommon. Window lengths in this study are allowed to vary depending on data type and quality. The median window length is near 3.5 seconds. Similarly, corner frequencies of a zero-phase bandpass filter were allowed to vary within 0.6 to 4 Hz to adapt to the different wave types.

3.2.4 The Mislocation Hemisphere

Figure 3.3 shows part of the lower hemisphere (0° to 50°) of polarization anomalies, namely deviations of observed from predicted polarization, where predicted again refers to values computed from IASP91 model with source locations from table 3.1. Here the free-surface effect is taken into account, as will be discussed below. In such a display, the center corresponds to vertical incidence. The perimeter gives 50° incidence with North at the top. We choose this type of diagram to facilitate comparison with predicted polarization patterns from anisotropic models.

Multiple nuclear events from two source regions (Nevada, Tuamotu) give rather consistent deviations of polarization to Northern directions. Also other geographic regions with several nearby events give rise to consistent polarization effects. For steeply incident phases from the North there is a general deviation to more Northern directions, while the Southern part of figure 3.3 shows tangential deviations, apparently varying rapidly over

the lower hemisphere. For example polarization anomalies from Northern Italy and Switzerland show opposite tangential effects. However, based on polarization data alone, this behaviour can not be interpreted in terms of heterogeneity or anisotropy. Consistently occuring source mislocation effects for these regional distances might also cause such variation. While this may be a problem of either polarization vector data or propagation vector data taken by itself, the difference is insensitive to source location errors and neither to distant lateral heterogeneity. Instrument calibrations were performed daily. Substantial deviations from the nominal response were rare and the correction had a rather small effect on the lower hemisphere representation.

3.2.5 Free Surface

Conversion at the free surface perturbs the incidence angle of the polarization direction. The apparent incidence angle Φ'_a for a P-wave is given by

$$\Phi'_a = tan^{-1}(\frac{2sin(\Phi_a)\sqrt{A^2 - sin^2(\Phi_a)}}{A^2 - 2sin^2(\Phi_a)}) \tag{3}$$

with the velocity ratio $A = v_p/v_s$ (Aki and Richards, 1981). The dependence of Φ'_a on Φ is shown in figure 3.4 for a number of Poisson's ratios κ, which are related to the velocity ratio A by $\kappa = \frac{A^{-2}-0.5}{A^{-2}-1}$. The three values are $\kappa = 0.2$ ($A = 1.63$; dotted line) ,$\kappa = 0.25$ ($A = 1.73$; solid line) and $\kappa = 0.3$ ($A = 1.87$; broken line). Figure 3.4 shows that the free-surface effect causes incidence angle deviations of several degrees. The free-surface correction is particularly important for large incidence angles. Variation of κ from $\kappa = 0.25$ to 0.2 or 0.3 produces offsets within 5° in the incidence range of our study (4° to 40°). The deviation between the curves is within a few degrees. For the free-surface correction (figure 3.3) we used a crustal Poisson ratio of $\kappa = 0.25$. This corresponds closely to the upper crustal mean value observed in the KTB drill hole, which is located about 150km northwest (figure 3.1a) in a similar geological setting (figure 3.1). Without this correction, the lower hemisphere has a distinctly different appearance (figure 3.5) with a clear radial component. The mean of this radial component is 5.1° oriented outwards. Clearly, the free-surface correction is an important and observable effect, which must be taken into account. On the other hand, we have seen that there are clear effects in figure 3.3 beyond the simple effect of crustal Poisson ratio alone. For the Southern part of figure 3.3 the radial effect almost vanishes.

3.2.6 Array Measurements

Propagation directions (θ_s, Φ_s) can be extracted from array data either from travel times or from fk-analysis. Characteristics of this problem have been studied by Bokelmann (1993), where it was shown that small-array data like the ones in this paper can produce propagation vector data with reasonable uncertainty given that topography (figure 3.1) is taken into account. We obtain the mislocation pattern of figure 3.6. Conversion from slowness p to incidence angle $\Phi_a = sin^{-1}(pv)$ was done using the local velocity estimate of v=5.2 km/s obtained from 3D array analysis (Bokelmann, 1993). In that pa-

58

per, the reader also finds a discussion on the consistency of propagation vector estimates from examples of Nevada and Tuamotu nuclear events. These data are included in this data set. In figure 3.6 they show comparatively small deviation documenting consistency for the array data. Nevertheless these deviations showed up as statistically significant (Bokelmann, 1993). There are even larger anomalies in these data though. The Northern deviation for steeply incident phases from the North which was observed for polarization data (figure 3.3) is not apparent in the array data. Interestingly the pattern for Yugoslavia and Romania are very similar to observed polarization anomalies in figure 3.3 as well as the rapid variation of Switzerland and Northern Italy. This suggests that either lateral heterogeneity or source mislocation is affecting propagation and polarization directions.

For an epicentral distance of about 400km the mean tangential deviation between Switzerland and Northern Italian events would require a relative source mislocation of about 70km occuring consistently in the PDE solutions (Preliminary Determination of Epicenters) between the two source regions. While this is not impossible, lateral heterogeneity, the Alpine root, might also cause the azimuthal deviation, or respectively, the relative source mislocation. Both would simultaneously perturb propagation and polarization directions.

Nevertheless, the procedure of relative analysis of polarization and propagation data gives data which are independent of the source location and distant lateral heterogeneity. The relative data (polarization - propagation vectors) from the 94 events are shown in figure 3.7. However, Nevada, Tuamotu, and other regions still show up with consistent effects. Naturally, the random scatter is larger for these differences than for the individual data. For two events the difference data were clearly dominated by noise and had to be removed. It may seem surprising that source mislocation and lateral distant heterogeneity don't affect the relative data. In fact, the method doesn't require knowledge of source locations at all. The propagation vector is used to determine the location in the lower hemisphere. Measured from this direction, the polarization vector deviation indicated presence of anisotropy. This allows studying anisotropy under the receivers. Lateron, we use the data of figure 3.7 in an inversion for anisotropy. But first, we review wave propagation theory in anisotropic media.

3.3 REVIEW OF PROPAGATION IN ANISOTROPIC MEDIA

Here we wish to merely state a few features of particular importance for this study. Comprehensive treatment of the topic has been given f.e. by Crampin (1981).

In a general anisotropic medium, the solution for a propagating plane wave front follows from the Ansatz

$$\mathbf{u}(\mathbf{r}, t) = \mathbf{a}(\mathbf{r})f(t - \mathbf{n}\mathbf{r}/c) \tag{4}$$

where $\mathbf{a}(\mathbf{r})$ describes amplitude and polarization of the wave, while the time-

dependence is given by $f()$ depending on the phase velocity c. From the equation of motion, we get

$$m_{il}a_l = c^2 a_i \qquad (5)$$

with the Christoffel matrix

$$m_{il} = c_{ijkl}n_j n_k/\rho \qquad (6)$$

(6) has the form of an eigenvalue equation with the square of the phase velocity appearing as eigenvalue. Hence polarization vectors **a** serve as eigenvectors. Due to the symmetry of the elasticity tensor c_{ijkl}, we can always choose a set of 3 mutually perpendicular eigenvectors. Below we will give examples of c_{ijkl}.

The typical way to solve (6) is to specify a propagation direction **n** and solve for eigenvalue and eigenvector for each of the three polarizations (in the nondegenerate case). It is clear that in general propagation and polarization vectors don't coincide for waves propagating in anisotropic media. For isotropic media that was the case. Therefore we can use such deviations to determine effective medium anisotropy.

For the case of P-waves, we will discuss this discrepancy more closely below, since both of these directions can be observed using arrays and three-component stations.

The wavefront propagates in the normal direction with the phase velocity $c = |\nabla t|^{-1}$. ∇t is the propagation vector, which can be estimated from data of small arrays (see also Helbig, 1958).

The polarization vector **a** gives the direction of local particle motion. It is measured directly by polarization analysis. Neither of these two vector should be confused with the group velocity vector, which is the direction, in which energy propagates (Musgrave, 1970). Crampin, Stephen and Mc-Gonigle (1982) showed that for weak anisotropy the difference between polarization and group velocity directions are small. This is intuitively clear, since the energy should propagate in a direction near the particle motion.

While the angular deviation between phase and group velocity vectors received quite some interest in the literature (Crampin, 1981; Crampin et al., 1982), relation between phase velocity and polarization vectors has been discussed for model crystals (Crampin, 1978, 1981; Crampin et al., 1982), but due to a lack of appropriate data, there are only few applications to real data so far (White et al., 1983; Li, Leary and Aki, 1987; de Parscau, 1991a). However, deviations of polarization directions from propagation directions can be substantial as we will see below. In the following we want to illustrate this effect and lateron exploit it in an inversion for effectively anisotropic structure. It is important to note that the polarization depends only on local anisotropy. This is illustrated in figure 3.8.

In the context of anisotropy, P-wave polarizations have been studied for VSP borehole data by de Parscau (1991a) and Li, Leary and Aki (1987). However, with a 1D array in the borehole, there is no control over off-azimuth arrivals.

We have seen that our method of relative analysis is insensitive against distant heterogeneity. But how about near-receiver heterogeneity? Inspection of polarization hemispheres for individual three-component instruments showed some station-dependent scatter which is partly due to deviations of the instrument response from nominal values. Small-scale heterogeneity near the receivers may also cause waveform distortions. Hence, polarization data from single three-component stations have to be regarded with some caution. Such data carry information about the local conditions under the station. For our purpose we average over all three-component stations of the array, thereby obtaining average polarization attributes, where array stations are well-distributed over an aperture of 4 km. The effect of near-receiver small-scale heterogeneity is expected to be nearly uncorrelated from station to station and we expect the averaging procedure to be effective in averaging out most of its effect on the difference pattern. The effect from larger-scale heterogeneity on the other hand, is likely correlated from station to station. We obtain a net effect in the polarization vectors, but similarly in the propagation vectors. The difference should therefore again be approximately unaffected. This argument suggests that although scatter is invariably present in difference patterns like figure 3.7, the scatter is dominated by random fluctuation and not by biases from discrete local scatterers. A very important feature of the GERESS array is the absence of a seismologically significant near-surface low-velocity layer, what can be shown from inspection of the train of P-S conversions.

3.4 UPPER-CRUSTAL ANISOTROPY

Anisotropy in the vicinity of the receivers, however, does affect the relative data in figure 3.7. Which depth range is it sensitive to? We have seen that polarization is a local property. For seismological phases of finite wavelength this means that the depth range equivalent to about a wavelength should affect the observed polarization. For the typical dominant frequencies in this study we have wavelengths of about 6 km. Hence, we expect to estimate a spatial average of anisotropic properties of the top few kilometers in the upper crust. Since we average over all three-component stations in the array, we assume that discrete heterogeneity within the array can be ignored and allow for an anisotropic but homogeneous model.

In this context, there are several phenomena which may cause effective anisotropy. Intrinsic anisotropy of minerals, as well as small-scale structure possessing certain symetry lead to directional dependence of macroscopic elastic parameters and hence propagation velocity. Sedimentary layering, with a potentially prominent effect, is not present here. However, cracks, fractures and rock foliation (Babuska and Cara, 1991), if certain orientations prevail, can give rise to substantial effects. Since our data are sensitive to a spatial average over several kilometers, we expect macroscopic anisotropic

61

behaviour either if the anisotropy is locally very strong or if preferred orientation is spatially coherent over a depth range of several kilometers within the topmost part of the upper crust. The latter may for example be the case for cracks caused by the regional stress field. Note that our P-wave polarization data are sensitive only to the depth range where brittle deformation is expected.

General anisotropic model/hexagonal case

Since the cause of anisotropy is not known beforehand, it is preferable to find elastic constants under no restricting assumptions. In the following we will study the type of constraints P-wave polarization data pose on elastic constants. We will restrict our attention to the case of hexagonal symetry, since this is a viable model for most of the possible causes of effective anisotropy mentioned above. An exception may be more complex intrinsic anisotropy of individual crystals, which is not considered here. In the case of a hexagonal or transversely isotropic symetry, the elastic constant matrix c_{ijkl} has the simple shape

$$
c_{ijkl} = \begin{pmatrix}
c_{11} & c_{11} - 2c_{66} & c_{13} & & & \\
c_{11} - 2c_{66} & c_{11} & c_{13} & & & \\
c_{13} & c_{13} & c_{33} & & & \\
& & & c_{44} & & \\
& & & & c_{44} & \\
& & & & & c_{66}
\end{pmatrix} \tag{7}
$$

with 5 unknowns, assuming that the symetry axis is in x_3-direction. Given this particular symetry, velocity v and polarization direction of P-waves depend only on the angle χ between propagation direction and symetry axis x_3.

3.4.1 Modelling of P-Velocity and Polarization Patterns

White (1983) and de Parscau (1991b) give exact expressions for velocity

$$
\rho v^2 = \frac{1}{2}(c_{11} + c_{44})sin^2\chi + (c_{33} + c_{44})cos^2\chi +
$$

$$
\left[\left((c_{11} - c_{44})sin^2\chi - (c_{33} - c_{44})cos^2\chi \right)^2 + 4(c_{13} + c_{44})^2 cos^2\chi sin^2\chi \right]^{1/2} \tag{8}
$$

and polarization angle ξ measured from the symetry axis

$$
tan\xi = \frac{(c_{13} + c_{44})cos\chi sin\chi}{\rho v^2(\chi) - (c_{11}sin^2\chi + c_{44}cos^2\chi)} \tag{9}
$$

(8) and (9) depend only on the four elastic constants c_{11}, c_{13}, c_{33} and c_{44}. The last constant c_{66} in (7) can be determined only from quasi-transversely polarized shear waves. de Parscau (1991b) showed that (9) can be simplified to

$$
tan2\xi = \frac{\eta sin2\chi}{1 - (1 + \tau)sin^2\chi} \tag{10}
$$

using the two parameters

$$\eta = \frac{c_{13} + c_{44}}{c_{33} - c_{44}} \qquad (11)$$

and

$$\tau = \frac{c_{11} - c_{44}}{c_{33} - c_{44}} \qquad (12)$$

This shows that we will i.g. not be able to independently determine the four elastic constants c_{11}, c_{13}, c_{33} and c_{44} from P-polarization data. Instead, constraints on these constants must be derived from the η and τ using the nonlinear relations (11) and (12). In addition to η and τ, the orientation of the symetry axis is unknown. Therefore we have 2 additional unknowns representing strike and dip of the symetry axis. Both τ and η can be seen as measures of anisotropy. Since c_{11} and c_{33} give ρv^2 parallel and normal to the symetry planes, τ gives a measure of the velocity deviation between these special directions. η is more difficult to interpret, but it can be approximately related to the P-velocity anisotropy at small incidence angles nearly normal to the symetry planes (de Parscau, 1991b). For an isotropic medium we have $\eta = \tau = 1$.

A number of criteria on the elastic coefficients in (7) can be derived from requiring stability, namely the condition that deformation is associated with nonnegative internal energy. The requirement is that (7) is positive semidefinite (Backus, 1962). It follows that all diagonal elements are nonnegative. Furthermore, $c_{11} \geq c_{66}$, $c_{33}(c_{11} - c_{66}) \geq c_{13}^2$ In our context, bounds on elastic coefficients are important for finding bounds on the parameters η and τ and for rejecting physically impossible models. Postma's (1955) inequality

$$(c_{11} - c_{44})(c_{33} - c_{44}) \geq (c_{13} + c_{44})^2 \qquad (13)$$

shows that $\tau \geq 0$. Since τ gives a measure of the size of P-wave anisotropy, an upper bound may be given from an estimate of maximum possible anisotropy. The sign of $c_{13} + c_{44}$, the nominator of η is found to have substantial importance for the polarization behaviour. Cases with $c_{13} + c_{44} \leq 0$ are physically possible, but they are found only is very carefully planned laboratory experiments (Helbig and Schoenberg, 1988). In these cases, the polarization angle is found to rotate in a sense opposite to the propagation direction, in contrast to the normal case with rotation in the same sense. For real Earth studies it is reasonable to assume $c_{13} + c_{44} \geq 0$, which gives us a lower bound $\eta \geq 0$. An upper bound on η can be found by applying a requirement that c_{11}/c_{44} and c_{33}/c_{44} be within a certain range.

Now we will illustrate polarization behaviour for two special cases, namely $(\eta, \tau) = (1.43, 2.13)$ and $(0.82, 1.00)$. These cases correspond to elastic parameters for models HCD1 and HCS1 (Crampin, 1984), which give the effective anisotropy associated with a model of oriented cracks (Hudson, 1981) in the limiting cases of fluid-saturated and dry conditions. To derive this model of oriented cracks, Hudson (1980) used mean field theory (Keller, 1964) and

derived expressions valid to second order. In his perturbative treatment the stiffness matrix can be represented as

$$c_{ijkl} = c_{ijkl}{}^0 + c_{ijkl}{}^1 + c_{ijkl}{}^2 \tag{14}$$

for long wavelengths, where the zero-order term gives the isotropic reference model specified by the Lamé parameters λ and μ

$$c_{ijkl}{}^0 = \lambda \delta_{ij} \delta_{kl} + \mu (\delta_{ik} \delta_{jl} + \delta_{il} \delta_{jk}) \tag{15}$$

The first and second-order perturbation terms can be interpreted as first-order effect of the cracks and crack-crack interaction. For the crack density $\epsilon = Na^3/V$ (N/V=number of cracks per volume, a=mean crack radius) they are

$$c_{ijkl}{}^1 = -\frac{\epsilon}{\mu} \begin{pmatrix} \lambda^2 & \lambda^2 & \lambda(\lambda + 2\mu) & & & \\ \lambda^2 & \lambda^2 & \lambda(\lambda + 2\mu) & & & \\ \lambda(\lambda + 2\mu) & \lambda(\lambda + 2\mu) & (\lambda + 2\mu)^2 & & & \\ & & & \mu^2 & & \\ & & & & \mu^2 & \\ & & & & & 0. \end{pmatrix} \mathbf{D} \tag{16}$$

and

$$c_{ijkl}{}^2 = \frac{\epsilon^2}{15} \begin{pmatrix} \lambda^2 q/(\lambda + 2\mu) & \lambda^2 q/(\lambda + 2\mu) & \lambda q & & & \\ \lambda^2 q/(\lambda + 2\mu) & \lambda^2 q/(\lambda + 2\mu) & \lambda q & & & \\ \lambda q & \lambda q & (\lambda + 2\mu)q & & & \\ & & & x & & \\ & & & & x & \\ & & & & & 0. \end{pmatrix} \mathbf{D}^2 \tag{17}$$

with $q = 15(\frac{\lambda}{\mu})^2 + 28(\frac{\lambda}{\mu}) + 28$ and $x = 2\mu \frac{3\lambda + 8\mu}{\lambda + 2\mu}$. Here the cracks are aligned perpendicular to x_3. $\mathbf{D}$ is the diagonal matrix with trace

$$trace(\mathbf{D}) = (u_{11}, u_{11}, u_{11}, u_{33}, u_{33}, 0) \tag{18}$$

u_{km} depends on conditions on the crack face. The dependence of c_{ijkl} on the crack parameters is only through $\mathbf{D}$ and is further given by

$$u_{11} = \frac{4}{3} \frac{(\lambda + 2\mu)}{(\lambda + \mu)}/(1 + k) \tag{19}$$

and

$$u_{33} = \frac{16}{3} \frac{(\lambda + 2\mu)}{(3\lambda + 4\mu)}/(1 + m) \tag{20}$$

with k and m given as

$$k = (\frac{\lambda' + 2\mu'}{\pi d \mu})/\frac{(\lambda + 2\mu)}{(\lambda + \mu)} \tag{21}$$

64

and

$$m = \frac{4\mu'}{\pi d\mu}\frac{(\lambda + 2\mu)}{(3\lambda + 4\mu)} \tag{22}$$

The ϵ-range of interest in this study is between 0 and 0.1 . For such low values of ϵ, the second-order approximation is considered uncritical (Crampin, 1981). d is the (large) aspect ratio of the cracks. λ' and μ' are the Lamé-parameters within the cracks. The two extreme cases with particular physical significance are 1) $\mu' = \lambda' = 0$ and 2) $\mu' = 0$ with nonzero λ'.

The first case models dry cracks (HCD1), with free surfaces at the crack faces. In this case k and m vanish. The polarization pattern is determined solely by $(\eta, \tau) = (1.43, 2.13)$. P-wave phase velocities and polarizations for this model of vertical East-West oriented cracks are shown in figure 3.9 in lower hemisphere representations, where for display purposes the symetry axis is shown pointing upwards in the paper plane. We choose the unconstrained absolute levels of c_{11}, c_{44} and c_{66} to conform to model HCD1 (background velocity $v_P = 5.8 km/sec$, $v_S = 3.349 km/sec$, density $\rho = 2.6 km/sec$).

This choice affects only the P-velocity pattern, but not the polarization pattern, which depends only on η and τ. Propagation in the plane of aligned cracks gives high velocity and the P-wave anisotropy for this ideal model is 24%. The right-hand side shows polarization anomalies, namely deviations of the polarization from propagation directions. In general the polarization direction deviates into the direction to larger phase velocity, diverging at the symmetry axis and converging to the symmetry plane.

For the second case (model HCS1), which models saturated cracks, we obtain figure 3.10. The parameters are the same as in figure 3.9, but with aspect ratio d=0.0001 and λ'=2.25 GPa. The polarization pattern is then given by η=0.82 and τ=1. Note that this velocity pattern differs substantially from the dry-crack model: The symmetry axis has also fast velocity. This gives rise to τ=1. Clearly, τ is very sensitive in distinguishing dry crack conditions from saturated ones. The difference between minimum and maximum velocity with 3.5% anisotropy is substantially smaller than for the dry-crack model. The maximum velocity achieved is somewhat higher than for the dry-crack model though. Polarization anomalies are smaller but give complexer pattern.

3.5 MODEL FITTING

Observed polarization anomalies can be related to the parameters η and τ describing the anisotropy. The inverse problem requires solving the eigenvalue problem (6). In this paper, this is done by nonlinear parameter fitting. As shown above, parameters in the inversion are η and τ, but also two angles $\tilde{\theta}$ and $\tilde{\Phi}$ describing azimuth and dip of the symmetry axis. In general, we will not be able to determine the 4 elastic constants independently. Instead

we may obtain two nonlinear constraints on these parameters from η and τ, which we may supplement with a priori information. In our case, such information is given by reasonable assumptions about the reference velocity. In the following we will use reference velocities used in the above examples HCD1 and HCS1. This enables us to also display velocity patterns for the inversion results.

For each event we have an observation of polarization direction $\begin{pmatrix} \theta_a \\ \Phi_a \end{pmatrix}$ and propagation direction $\begin{pmatrix} \theta_s \\ \Phi_s \end{pmatrix}$. We wish to compare these angular differences $\begin{pmatrix} \Delta\theta \\ \Delta\Phi \end{pmatrix} = \begin{pmatrix} \theta_a - \theta_s \\ \Phi_a - \Phi_s \end{pmatrix}$ with predictions from models depending on the parameters ($\tilde{\theta}$, $\tilde{\Phi}$, η, τ), which we call $\begin{pmatrix} \Delta\theta_i'(\eta,\tau,\tilde{\theta},\tilde{\Phi}) \\ \Delta\Phi_i'(\eta,\tau,\tilde{\theta},\tilde{\Phi}) \end{pmatrix}$ for the i-th event. We obtain the best fitting model by inspecting the misfit on the sphere

$$S(\tilde{\theta},\tilde{\Phi},\eta,\tau) = \frac{1}{N}\sum_{i=1}^{N}\left[cos^{-1}\left(cos(\Delta\Phi_i - \Delta\theta_i')cos(\Delta\theta_i - \Delta\Phi_i')\right)\right]^2 \quad (23)$$

which is the analogon of the standard sum-of-squares misfit criterion on the sphere.

The models HCD1 and HCS1 have shown that the polarization pattern may vary considerably, depending on the choice of η and τ. We start the discussion of inversion results by studying the dependence of the misfit on symetry axis orientation for these two special cases. η and τ are fixed to (1.43, 2.13) in the first case of dry cracks and (0.82, 1.) in the case of saturated cracks. We are left with fitting $\tilde{\theta}$ and $\tilde{\Phi}$. The nonlinear search may use a rotation of the elastic constant matrix

$$c_{ijkl} = \eta_{ip}\eta_{jq}\eta_{kr}\eta_{ls}c_{pqrs} \quad (24)$$

with the rotation matrix η. While this allows for all types of symetry, we may more efficiently use (9) in our case of hexagonal symetry. Results for the dry-crack case are given in figure 3.11 showing the achieved misfit S given in degree^2 by (23) depending on the orientation of the symmetry axis, namely its location in the lower hemisphere. Axes orientations with small misfit are near the circumference. The smallest achieved misfit is 135 degree^2, which is substantially larger than the starting misfit of 68.8751 degree^2. The simple dry-crack model is clearly incompatible with the data. On the other hand, the saturated-crack model (figure 3.12) gives reasonable variance reduction of about 41%. Figure 3.12a shows that small misfits are achieved for symmetry axis locations in two regions in the Southwest and Northeast. Only the Southwestern region gives rise to statistically significant solutions. The lowest contour shows the confidence region where the critical misfit level is computed from the f-distribution as

$$S_{crit} = S_{opt}[1 + \frac{k}{N-k}f_{k,N-k}(1-\alpha)] \quad (25)$$

66

(Jenkins and Watts, 1969), where S_{opt} is the minimum misfit and k=4 the number of parameters. Higher contours give 2 and 4 times the separation of the critical level ($1 - \alpha = 0.95\%$ confidence level) from the minimum level. The optimum model has a symmetry axis orientation of azimuth $\tilde{\theta} = 208°$ and dip $\tilde{\Phi} = 36°$. The symmetry plane is oriented normal to the symmetry axis, and has strike 118° and dip 54° to the North. The optimum model corresponding to the global minimum in the Southwest is shown in figure 3.12b by its velocity and polarization pattern. To be directly comparable with the data, only the partial lower hemisphere from 0° to 55° is shown. Beside the symmetry plane, also the symmetry axis shows up with fast velocity in the lower part of the figure. The polarization deviations on the right-hand side of figure 3.12b are given for 0°, 10°, ..., 50° incidence and may be compared with the data in figure 3.7. The major features of the data set are explained by the model.

The results for assumed dry and saturated-crack model are quite different. The saturated-crack model gave reasonable fit to the data and a strike angle of the high-velocity plane of 118°, while the dry-crack was in clear conflict with the data.

Now we perform the more general nonlinear search for the parameter set $(\tilde{\theta}, \tilde{\Phi}, \eta, \tau)$, which unlike the previous example does not assume a particular physical fracture model. With 4 parameters and the given bounds on η and τ this search is not particularly compute-intensive, but guarantees the globally optimal solution, given that the bounds are appropriate and the sampling is sufficiently fine. The misfit pattern in figure 3.13a is not unlike the one for the saturated crack model. However, the optimum in the Southwest is more pronounced now and the variance reduction is three percent larger, now about 44%. The resulting parameters are $\tilde{\theta} = 203.3°$, $\tilde{\Phi} = 41.05°$, $\eta = 0.887$ and $\tau = 1.09$. The maximum P-velocity difference of the model is about 4.7%. The change in orientation from the fit of model HCS1 by a few degrees is insignificant considering the large confidence region in figure 3.12a. In the general model the confidence region is substantially smaller. For the polarizations, the main difference is the behaviour in the South-Western part, where the general model predicts a somewhat smaller effect. This corresponds to the smaller velocity contrast in that region. The high-velocity symetry plane strikes with about 113° and dips with about 49° to the Northeast.

In the search we varied η and τ independently. But can they be resolved independently by the data constraints or are they subject to a major tradeoff? Figure 3.14 shows the misfit around the optimum model keeping the symetry axis orientation fixed and varying η and τ. The lowest contour again shows the confidence region of admissible η and τ, which extends for η from 0.76 to 1.07 and for τ from 1. to 1.2 . The isotropic case at $\eta = 1$ and $\tau = 1$ is well outside the highest contour for four times the critical misfit separation.

The strong ascent for λ' near 0 strongly discriminates against the dry crack model.

3.6 WHAT CAUSES THE EFFECTIVE ANISOTROPY?

In principle, intrinsic anisotropy as well as macroscopic effects from oriented cracks, fractures or layering can cause anisotropy of this size. To understand the nature of this anisotropy, it is of large value to consider geological evidence for the region. The array is located on outcrop of granite and gneiss. While the granite apparently has no preferred alignment, the gneiss shows strong foliation with consistent orientations. The strike is approximately 120°and the dip 50-60°(Ott, pers.comm.). This closely coincides with the orientation of the high-velocity planes for the best-fitting model from the unconstrained inversion (figure 3.13) suggesting that rock foliation is the major cause of anisotropy in this case. The size of the anisotropy suggests that the foliation direction is spatially consistent over some distance, perhaps several kilometers. In fact, surface geology does suggest that this is indeed the case (Ott, pers.comm.). Rock foliation as a cause of effective anisotropy has been discussed before (f.e. Lüschen et al., 1991).

But is rock foliation the only factor involved and how does the overall anisotropy relate to intrinsic properties of minerals? Gneisses typically contain large amounts of mica, a mineral giving rise to very large anisotropy. Since these mineral are usually quite well-oriented (Wang et al., 1975), we may expect major effect on the observed anisotropy. In fact, mica orientations are typically dominant in forming macroscopic gneiss foliation planes (Suppe, 1985). Pure mica, however, does not explain the observed effect. Aleksandrov and Ryzhova (1961) give elastic constants for muscovite, for which we compute $\eta = 0.625$ and $\tau = 3.88$. The latter value is clearly incompatible with our results. More realistic models would include structural complexity, the occurence of several types of intrinsic anisotropy, and fractures or cracks in the subsurface. In fact, we have physical models at our disposition predicting some of these effects. For a medium consisting of anisotropic layers, Schoenberg and Douma (1988) give expressions for averaging elastic constants to obtain effective elastic constants in the long-wavelength assumption. For such a medium, also effective parameters $\bar{\eta}$ and $\bar{\tau}$ are composed of the averaged elastic constants as

$$\bar{\eta} = \frac{\bar{c}_{13} + \bar{c}_{44}}{\bar{c}_{33} - \bar{c}_{44}} \tag{26}$$

$$\bar{\tau} = \frac{\bar{c}_{11} - \bar{c}_{44}}{\bar{c}_{33} - \bar{c}_{44}} \tag{27}$$

using

$$\bar{c}_{11} = < c_{11} > - < c_{13}^2/c_{33} > + < c_{13}/c_{33} >^2 / < 1/c_{33} > \tag{28}$$

$$\bar{c}_{13} = < c_{13}/c_{33} > / < 1/c_{33} > \tag{29}$$

$$\bar{c}_{33} = 1/ < 1/c_{33} > \tag{30}$$

$$\bar{c}_{44} = 1/ < 1/c_{44} > \qquad (31)$$

where $<>$ denotes the thickness-weighted average of the respective quantity. If we take the simple approach of assuming that due to their large effect only mica contribute to the bulk anisotropy, we may simply compute η and τ for different percentages of mica content. For a mica fraction of 30% mica after Wang et al. (1975) and 70% other material assumed to be isotropic we obtain $\eta = 0.816$ and $\tau = 1.74$. While this is far outside the confidence region of the observation, values for 3% to 8% mica content fall within the confidence region (figure 3.14). These are low values compared with mica contents in typical gneisses (Wang et al., 1975). We have to keep in mind though that certainly not all of the mica minerals are fully aligned. Other constituents may also play a minor role in defining the bulk anisotropy.

Satisfying the polarization data, this gneiss model is also a plausible explanation in conjunction with the geological data. Another possible model, however, is that of cracks or fractures aligned in the direction of planes of weakness which we coincide with the gneiss foliation. Fitting a model of aligned cracks after Hudson (1981) had given essentially the same orientation. Resulting parameters were strike 114° and dip 50° for the symetry planes. We also obtained a crack density of $\epsilon = 0.09$ and two Lamé parameters of the crack material $\lambda' = 0.049$ GPa and $\mu' = 0.0$ GPa. The associated error bars discriminate clearly against the dry-crack case, where $\lambda' = 0.GPa$. Such dry cracks give rise to large values of τ, which we have previously argued, are in conflict with the data. Based on the achieved misfit, the model of cracks opening along the foliation planes can not be ruled out.

It appears difficult to distinguish between models of intrinsic anisotropy and cracks or fractures. In this case, one should consider all possible models. In fact, the occurence of cracks along planes of weakness given by foliation planes is not unlikely. For small pressures in the laboratory, it is very common to observe opening of cracks along the foliation direction. This can be demonstrated f.e. with the data of Wang et al. (1975). From their data we obtain values of $\tau \approx 1.25$ at 1kbar pressure and much larger values up to 10 at lower pressure. Opening of cracks can be caused by the local stress field. Values for the strike of the maximum horizontal stress direction σ_H in the area are around 149° in the KTB borehole (Brudy, Fuchs and Zoback, 1993), but there are also values in the range of 115° (f.e. Falkenberg granite, Rummel et al., 1983). These values are not far from the foliation strike. Hence crack opening along the foliation direction is not unlikely, particularly if the fluid pressure were high. However, we note that anisotropy in our data set appears to be due to foliation rather than vertical cracks perpendicular to the smallest horizontal stress direction. On the other hand, the regional stress field may have an effect due to opening of cracks preferentially parallel to the planes of weakness, which are given by the gneiss foliation planes.

Perhaps, more insight can be gained if also shear waves are used. Figure 3.15 gives the prediction of the shear wave velocities for the optimum model. However, unambiguous determination of upper crustal anisotropy requires in-

cidence angles within the shear wave window and sources close enough to the receivers to not be sensitive to more distant anisotropy. These conditions are difficult to meet for our region. In contrast, for the study of local anisotropy P-wave polarization data may be used from local, regional and teleseismic events, if the 3-component array meets the measurement requirements.

ACKNOWLEDGEMENTS

REFERENCES

Aki, K., Richards, P.G., 1983, *Quantitative Seismology, theory and methods*, vol. I, Freeman, San Francisco

Aleksandrov, K.S., Ryzhova, T.V., 1961, The elastic properties of rock-forming minerals, II: layered silicates, *Izv. Acad. Sci. USSR, Geoph. Ser.*, 2. 186-189.

Anderson, D.L., Minster, B., Cole, D., 1974. The effect of oriented cracks on seismic velocities, *Journal of Geophysical Research*, **79**, 4011-4015.

Ando, M., Ishikawa, Y., Yamazaki, F., 1983. Shear wave polarization anisotropy in the upper mantle beneath Honshu, Japan, *Journal of Geophysical Research* **88**, B7, 5850-5864.

Babuska, V., Cara, M., 1991. Seismic anisotropy in the Earth, Kluwer Academic Publishers, Doordrecht.

Backus, G.E., 1962, Long-wave elastic anisotropy produced by horizontal layering, *Journal of Geophysical Research*, 67, 11, 4427-4440.

Backus, G.E., 1965. Possible forms of seismic anisotropy of the uppermost mantle under oceans, *Journal of Geophysical Research* **70**, 14, 3429-3439.

Beauchamp, K.G., (ed.), 1975. *Exploitation of seismograph networks*, No-

ordhoff, Leiden, Proceedings of the Nato Advanced Study Institute, Sandefjord, Norway.

Bokelmann, G.H.R., 1992. Upper and lower mantle small-scale heterogeneity studied by systematic analysis of portable broadband waveforms and traveltimes, *PhD Thesis*, Princeton University, Princeton, NJ, USA.

Bokelmann, G.H.R., 1993. Significant azimuth and slowness deviations from the GERESS regional array, *submitted to Bulletin of the Seismological Society of America.*

Brudy, M., K. Fuchs, M.D. Zoback, 1993. Stress orientation profile to 6 km depth in the KTB main borehole, *KTB Report 93-2.*

Crampin, S., 1978. Seismic-wave propagation through a cracked solid: polarization as a possible dilatancy diagnostic, *Geophysical Journal of the Royal Astronomical Society* **53**, 467-496.

Crampin, S., 1981. A review of wave motion in anisotropic and cracked elastic-media, *Wave Motion* **3**, 343-391.

Crampin, S., 1984. Effective anisotropic elastic constants for wave propagation through cracked solids, *Geophysical Journal of the Royal Astronomical Society* **76**, 135-145.

Crampin, S., Stephen, R.A., McGonigle, R., 1982. The polarization of P-waves in anisotropic media, *Geophysical Journal of the Royal Astronomical Society* **68**, 477-485.

de Parscau, J., 1991a. P- and SV-wave transversely isotropic phase velocities analysis from VSP data, *Geophysical Journal International* **107**, 629-638.

de Parscau, J., 1991b. Relationship between phase velocities and polarization in transversely isotropic media, *Geophysics* **56**, 10, 1578-1583.

Dziewonski, A.M., Anderson, D.L., 1983. Traveltimes and station corrections for P waves at teleseismic distances, *Journal of Geophysical Research* **88**, 3295-3314.

Garbin, H.D., Knopoff, L., 1975. Elastic moduli of a medium with liquid-filled cracks, *Quarterly Journal of applied Mathematics*, **33**, 301-303.

Harjes, H.P. 1990. Design and siting of a new regional array in central Europe, *Bulletin of the Seismological Society of America* **80**, B, 1801-1817.

Harjes, H.P., Jost, M.L., Schweitzer, J., Gestermann, N. 1993. Automatic

seismogram analysis at GERESS, *Computers&Geosciences*, **19**, 2, 157-166.

Helbig, K., 1958, Elastische Wellen in anisotropen Medien, *Gerlands Beiträge zur Geophysik*, **67**, 177-211.

Helbig, K., Schoenberg, M., 1988, Anomalous polarization of elastic waves in transversely isotropic media, *Journal of the Acoustical Society of America* **81**, 1235-1245.

Hess, H., 1964. Seismic anisotropy under the uppermost mantle under oceans, *Nature* **203**, 629-631.

Hudson, J.A., 1980. Overall properties of a cracked solid, *Mathematical Proceedings of the Cambridge Philosophical Society*, **88**, 371-384.

Hudson, J.A., 1981. Wave speeds and attenuation of elastic waves in material containing cracks, *Geophysical Journal of the Royal Astronomical Society* **64**, 133-150.

Jenkins, G.M., Watts, D.G., 1969. *Spectral analysis and its applications*, Holden-Day, San Francisco.

Jurkewicz, A., 1988. Polarization analysis of three-component array data, *Bulletin of the Seismological Society of America*, **78**, 5, 1725-1743.

Kanasewich, E.R., 1981, *Time sequence analysis in geophysics*, University of Alberta Press.

Keller, J.B., 1964. Stochastic equations and wave propagation in random media, *Proceeding of the Symposium on Applied Mathematics* **16**, 145-170.

Li. Y.-G., Leary, P.C., Aki, K., 1987. Observation and modeling of fault-zone fracture seismic anisotropy - II. P-wave polarization anomalies, *Geophysical Journal of the Royal Astronomical Society*, **91**, 485-492.

Lüschen, E., Söllner, W., Hohradt, A., Rabbel, W., 1991. Integrated P- and S-wave borehole experiments at the KTB-deep drilling site in the Oberpfalz area, in: R. Meissner, L. Brown, W. Franke, H.J. Dürbaum, F. Seifert (eds.), *Continental Lithosphere: Deep Seismic Reflections*, American Geophysical Union, Geodynamics Series 22, 121-133.

Musgrave, M.J.P., 1970. *Crystal Acoustics*, Holden-Day, San Francisco.

Postma, G.W., 1955, Wave propagation in a stratified medium, *Geophysics*, **20**, 780-806.

Rummel, F., Baumgärtner, J., Alheid, H.J., 1983. Stress measurements along the eastern boundary of the SW-German block, in: *Proceedings of the Workshop on Fracturing Stress Measurements*, National Academic Press, Washington, DC, p.3-17.

Schoenberg, M., Douma, J., 1988, Elastic wave propagation in media with parallel fractures and aligned cracks, *Geophysical Prospecting* 36, 571-590.

Silver, P.G., Chan, W.W., 1991. Shear wave splitting and subcontinental mantle deformation, *Journal of Geophysical Research*, 96, B10, 16429-16454.

Suppe, J., 1985, *Principles of structural geology*, Prentice-Hall, NJ.

Wang, C.-Y., Lin, W., Wenk, H.-R., 1975, The effects of water and pressure on velocities of elastic waves in a foliated rock, *Journal of Geophysical Research* 80, 1065-1069.

White, J.E., 1983. *Underground sound, application of seismic waves*, Elsevier, Amsterdam.

White, J.E., Martineau-Nicoletis, L., Monash, C., 1983, Measured anisotropy in Pierre Shale, *Geophysical Prospecting*, 31, 709-725.

TABLE 3.1: Events Used in this Study
(Location and time from PDE Monthly Bulletin, if not stated otherwise)

Year, Day, Hour, Min, Sec.	Latitude	Longitude	Depth	Phase
1990 123 01 03 38	43.315	19.890	5.	Pn
1990 240 20 21 22	36.267	27.218	39.9	Pn
1990 246 10 48 33	45.915	15.873	20.	Pn
1990 253 12 17 36	70.770	-13.803	10.	P
1990 258 23 07 43	64.655	-17.617	10.	P
1990 285 17 30 00	37.250	-116.490	0.	P
1990 297 15 04 14	73.360	54.670	0.	P
1990 318 18 11 58	-22.258	-138.805	0.	PKP
1990 325 16 59 58	-21.9	-138.980	0.	PKP
1990 331 04 37 58	43.853	16.633	24.	Pn
1990 331 04 51 36	43.895	16.641	10.	Pn
1990 347 00 24 26	37.3	15.438	11.1	Pn
1990 348 03 21 27	39.347	15.355	276.	Pn
1990 350 15 45 41	41.361	43.715	33.	P
1990 355 13 12 53	-18.891	-177.971	457.	PKP
1991 038 07 12 48	47.590	15.503	10.	Pn
1991 042 15 43 44	44.871	6.704	14.	Pn
1991 059 15 29 42	51.690	16.360	0.	Pn
1991 074 03 24 09	34.343	26.389	7.1	Pn
1991 078 02 51 26	39.260	20.429	10.	Pn
1991 094 19 00 00	37.296	-116.313	0.	P,PcP
1991 100 01 08 40	37.359	36.221	10.	P
1991 111 08 51 56	37.972	19.952	39.8	Pn
1991 116 22 35 11	43.446	16.244	12.	Pn
1991 119 09 12 48	42.453	43.673	17.2	P
1991 119 18 30 42	42.503	43.899	14.3	P
1991 120 03 40 36	51.690	16.206	10.	Pn
1991 122 10 15 17	47.929	16.209	10.	Pn
1991 123 23 41 02	42.647	43.263	10.8	P
1991 136 02 06 17	52.309	7.649	52.4	Pn
1991 138 17 14 59	-21.832	-139.014	0.	PKP
1991 143 19 42 56	51.416	15.850	10.	Pn
1991 149 18 59 58	-22.256	-138.794	0.	PKP
1991 149 20 24 40	45.016	8.213	10.	Pn
1991 154 10 22 40	40.048	42.859	27.8	P
1991 165 17 59 58	-21.944	-138.988	0.	PKP
1991 166 00 59 20	42.461	44.009	9.4	P
1991 185 06 26 32	42.387	44.116	20.4	P
1991 191 23 57 20	51.424	16.217	0.	Pn
1991 196 18 09 58	-21.877	-138.963	0.	PKP
1991 200 01 19 52	45.344	21.123	10.	Pn

1991 200 01 27 32	45.312	21.053	10.	Pn
1991 222 05 23 48	51.428	16.242	0.	Pn
1991 252 18 36 52	51.414	16.220	0.	Pn
1991 257 19 00 00	37.226	-116.428	0.	P,PcP
1991 279 01 46 48	41.096	43.409	18.3	P
1991 281 03 31 16	45.587	149.049	146.	P
1991 291 19 12 00	37.063	-116.045	0.	P,PcP
1991 301 00 21 32	44.265	21.456	67.	Pn
1991 303 16 24 21	45.029	9.937	10.7	Pn
1991 304 09 31 17	45.011	10.059	10.	Pn
1991 324 01 54 17	46.778	9.519	10.	Pn
1991 325 02 16 32	45.491	21.176	27.	Pn
1991 326 07 40 01	45.019	9.985	11.	Pn
1991 327 01 06 31	51.428	16.243	0.	Pn
1991 332 17 19 56	36.924	49.603	15.7	P
1991 336 08 49 40	45.498	21.115	9.	Pn
1991 336 09 04 43	45.437	21.247	10.	Pn
1991 337 16 58 23	44.994	9.965	14.	Pn
1991 338 13 31 31	44.978	9.932	19.6	Pn
1991 351 06 38 17	47.393	151.499	157.	P
1991 353 03 12 22	45.907	21.569	10.	Pn
1991 353 18 55 17	28.102	57.304	27.	P
1991 354 02 06 05	24.720	93.103	41.	P
1991 356 08 43 13	45.533	151.021	25.	P
1992 001 10 12 20	44.984	9.962	23.1	Pn
1992 002 19 41 45	5.638	-73.832	134.	P
1992 014 12 22 22	51.534	16.181	10.	Pn
1992 023 06 27 39	38.356	20.307	10.	Pn
1992 033 00 31 30	-51.547	139.704	10.	PKP
1992 048 00 01 57	79.191	124.482	10.	P
1992 048 19 23 14	46.761	9.505	10.	Pn
1992 052 20 50 32	45.463	14.328	11.	Pn
1992 062 12 29 40	52.915	159.886	39.	P
1992 065 14 39 10	52.9	159.619	45.	P
1992 067 01 53 38	10.210	-84.323	79.	P
1992 073 17 18 43	40.2	39.500	27.2	P
1992 103 08 19 30	43.964	13.022	10.	Pn
1992 104 01 20 01	51.157	5.815	15.	Pn
1992 112 22 28 06	43.264	17.961	33.	Pn
1992 126 16 48 03	43.286	17.471	10.	Pn
1992 129 06 44 39	47.248	9.584	10.	Pn
1992 129 07 51 25	47.233	9.564	10.	Pn
1992 130 05 37 58	49.953	7.409	10.	Pn
1992 136 00 43 42	47.239	9.543	5.	Pn
1992 140 14 25 04	49.105	6.623	18.	Pn

1992 142 04 59 57	41.591	88.805	0.	P
1992 148 18 14 00	44.406	11.737	10.	Pn
1992 149 09 52 42*	44.150	11.466	5.	Pn
1992 149 12 26 02*	43.966	11.977	13.6	Pn
1992 286 13 09 56	29.888	31.223	24.7	P
1992 297 23 19 47	42.503	45.073	33.	P
1992 323 21 10 41	38.300	22.428	10.	Pn
1992 326 05 07 23	35.931	22.443	70.2	P
1993 027 23 41 00	35.963	22.511	62.8	Pn

* Location and time information from ROM

a)
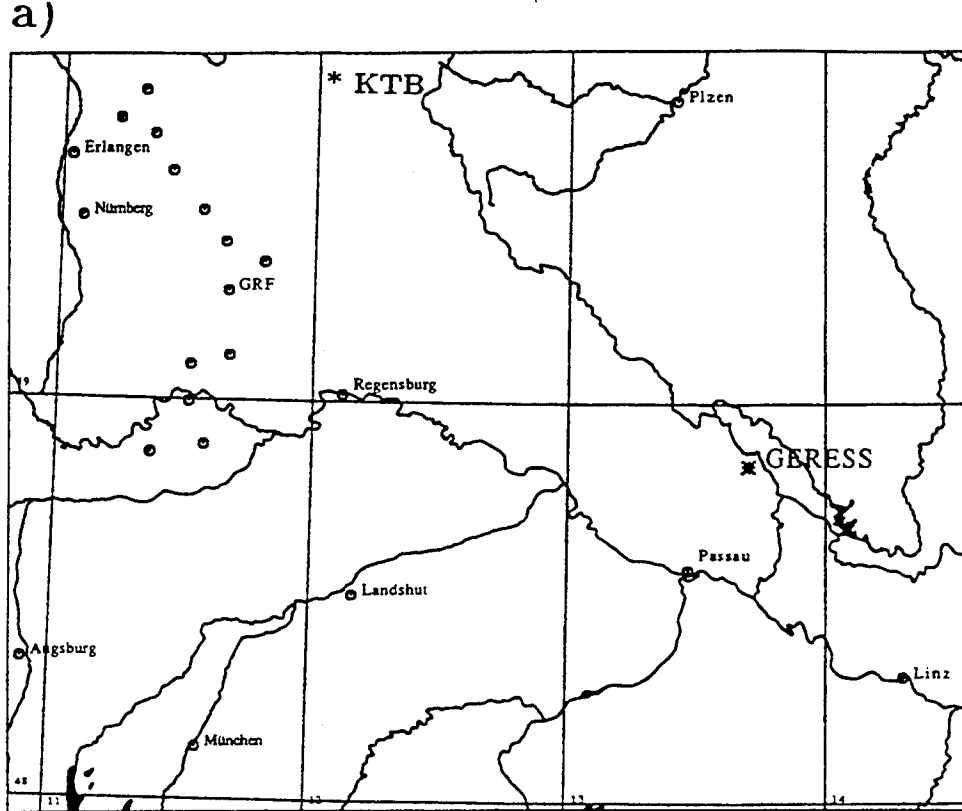
b) GERESS Array Configuration
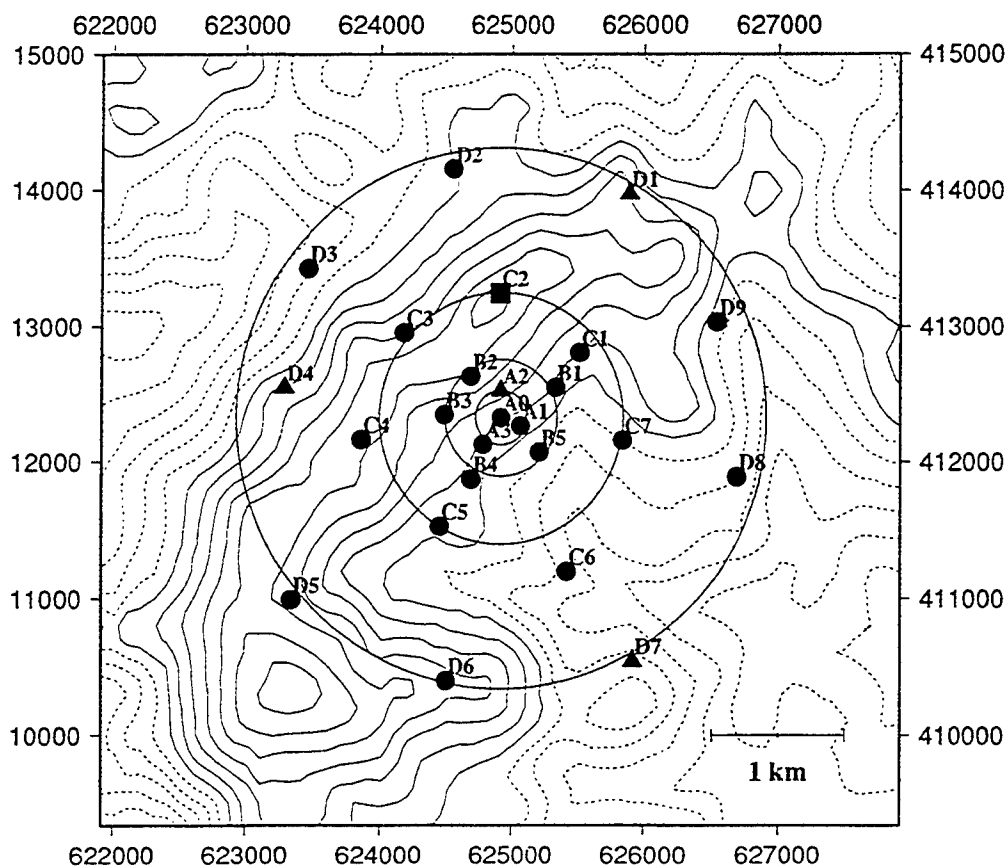
Figure 3.1. a) Geographic location of the GERESS array in Southeastern Germany. b) Array locations in Gauss-Krüger coordinates. Data from 25 vertical-component shortperiod instruments and three-component instruments (triangles and rectangles) are used in this paper. The topographic variation across the array is about 200 meters.
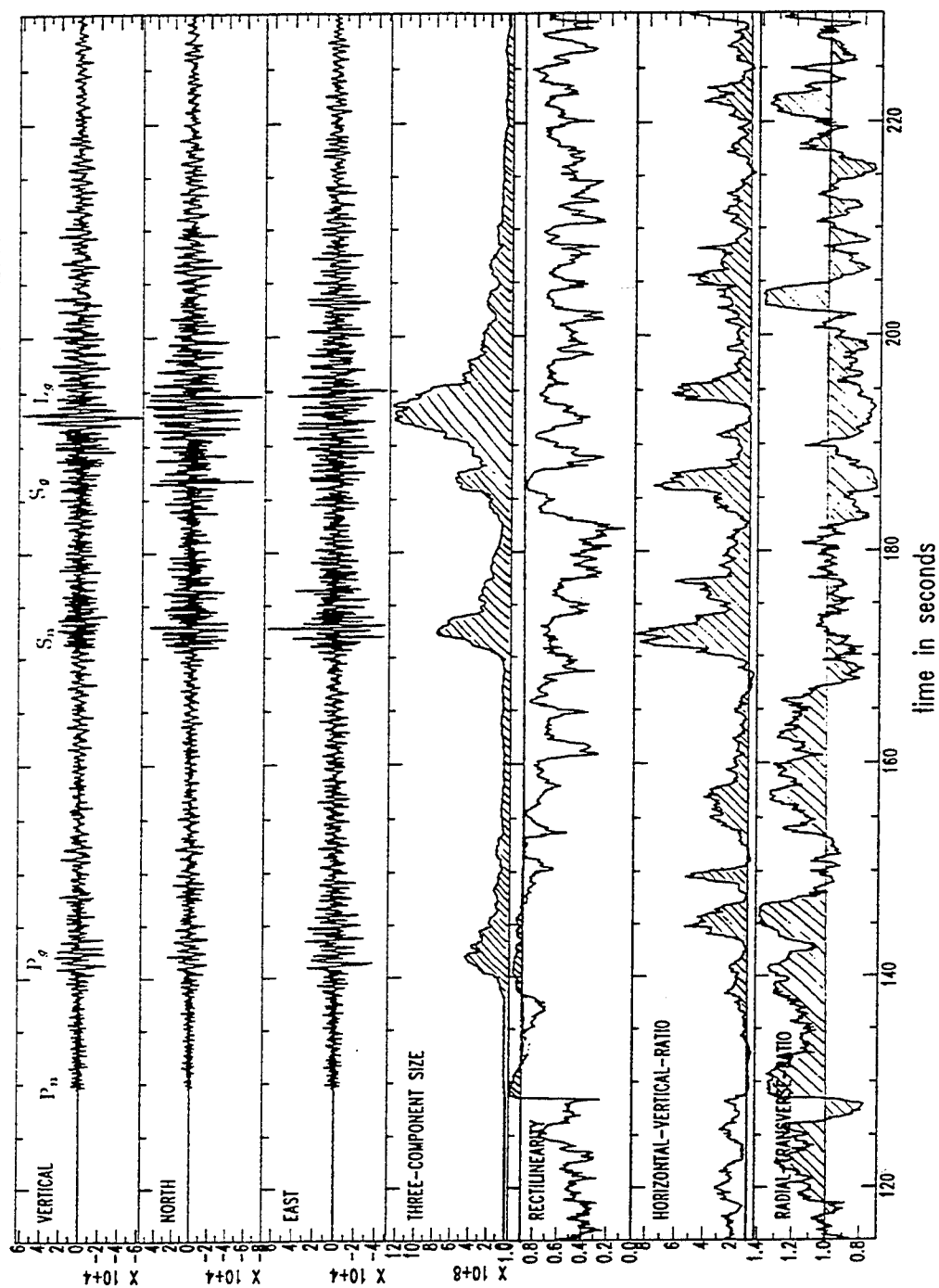
Figure 3.2: Polarization attributes of three-component data indicative for body wave phases. The three-component amplitude, the root-mean-square amplitude of the three-component seismogram shows the main phases clearly. Rectilinearity and component ratios allow determination of the wave type.

Observed Polarization Deviations

(lower hemisphere projection: 0 - 50 deg)
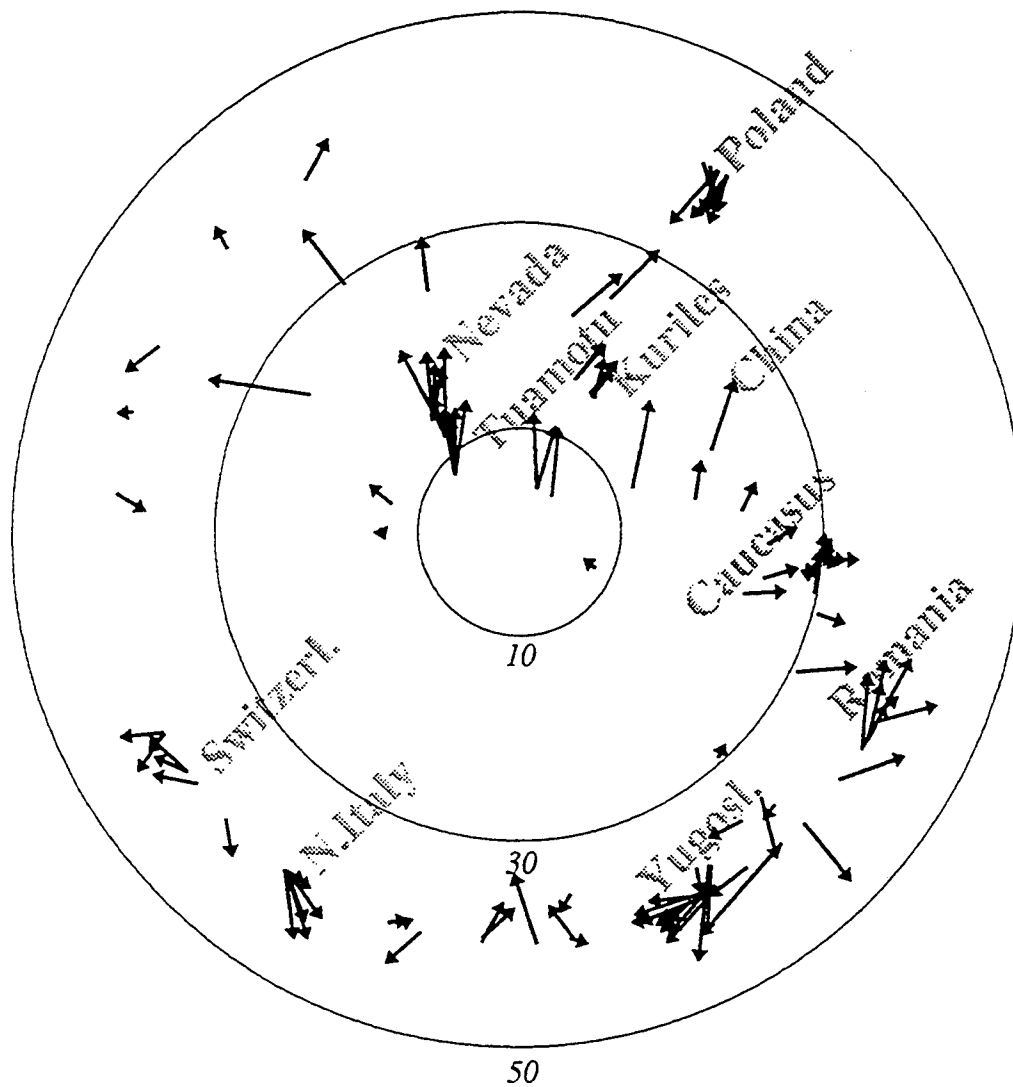
Figure 3.3: Lower hemisphere under the GERESS array (to 50° incidence) showing event polarization anomalies averaged over all three-component instruments. Lower hemisphere locations of first arriving phases for a few geographic regions are shown. Note the consistent deviation to Northern directions for phases steeply incident from North.

Free-Surface Effect on Polarization Inc.Angle
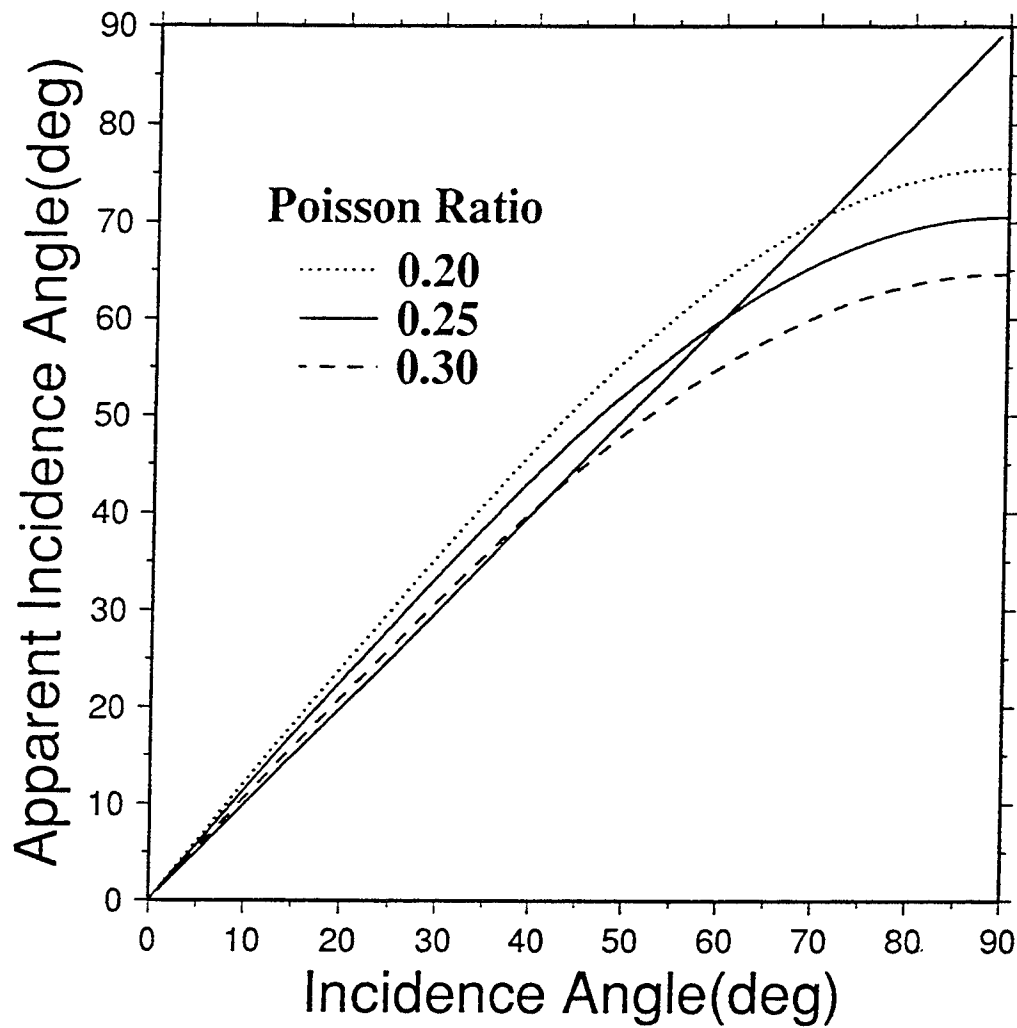
Figure 3.4: Free-surface effect on polarization incidence angles for a set of Poisson ratios.

Observed Polarization Deviations

(without free-surface correction)
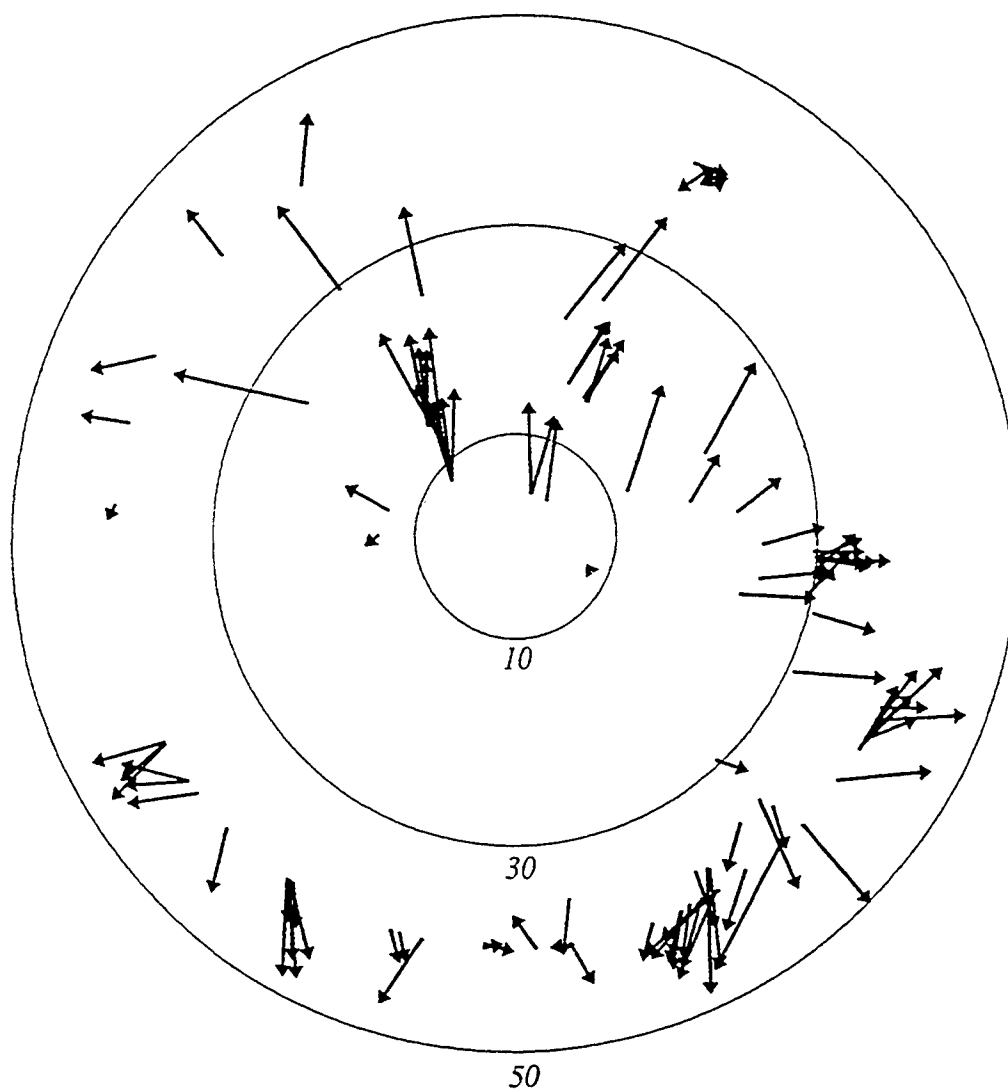
Figure 3.5: Lower hemisphere representation of polarization anomalies (without free-surface correction). Compared with figure 3.3 there is a clear radial component with a mean of 5.1°. Clearly, the free-surface effect gives rise to an observable effect which must be corrected.

Observed Propagation Deviations
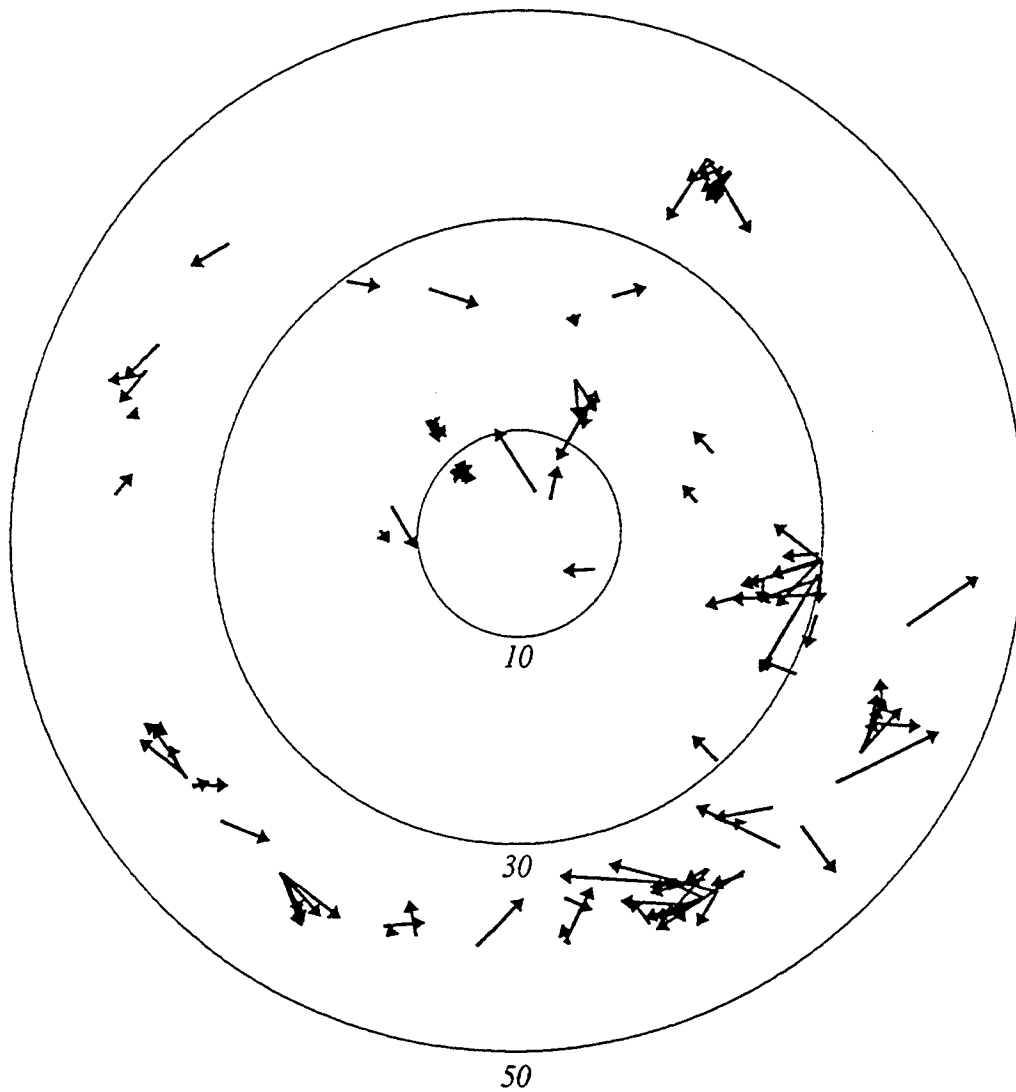
Figure 3.6: Propagation vector anomalies from array data analysis shown on the lower hemisphere (0° to 50°).

Difference Vectors (Polarization - Propagation)
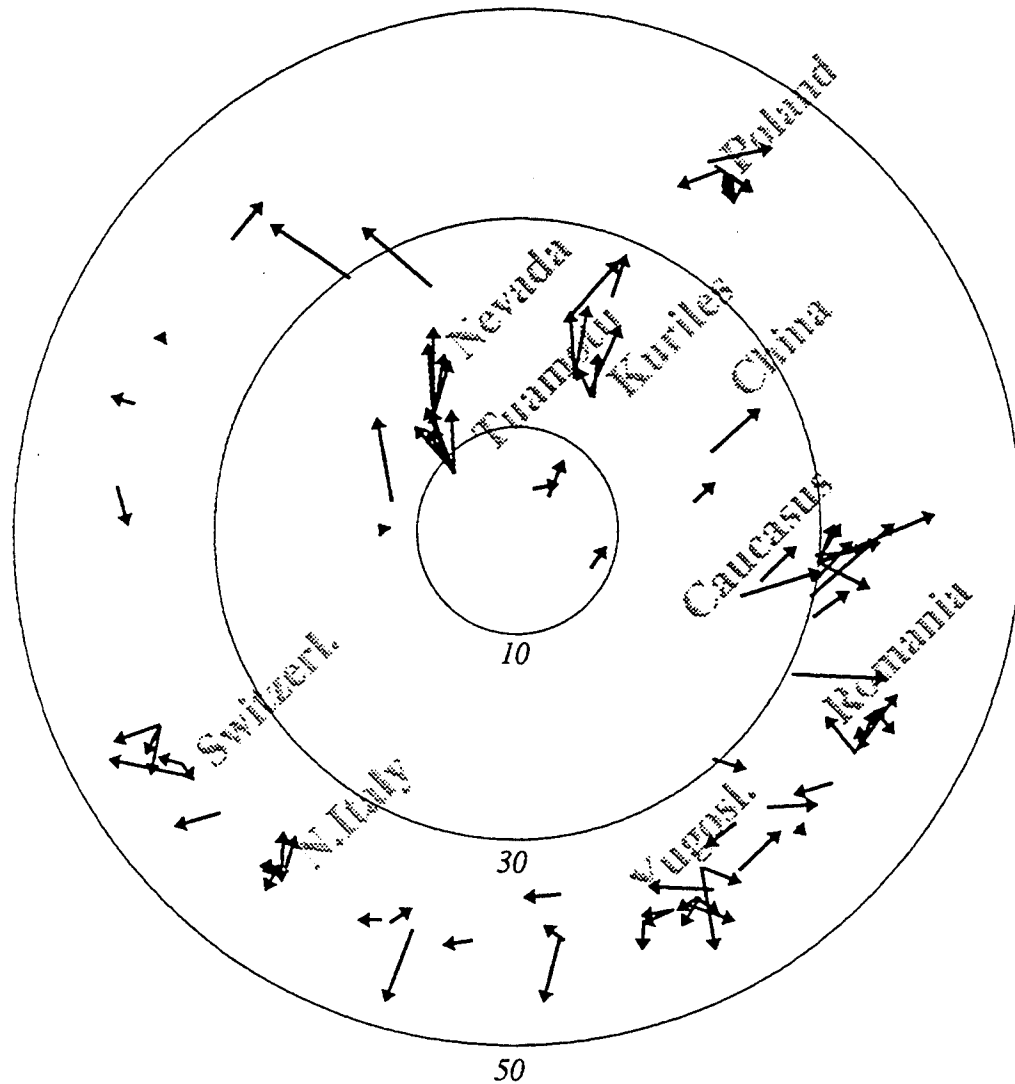
Figure 3.7: Difference of polarization and propagation vectors shown on the lower hemisphere (0° to 50°). These are the data for the inversion procedure in the later part of this paper.

array of 3-component stations

predicted propagation direction

$\hat{s}$ = propagation direction

$\hat{a}$ = polarization direction

$\Delta\Phi$

wavefront
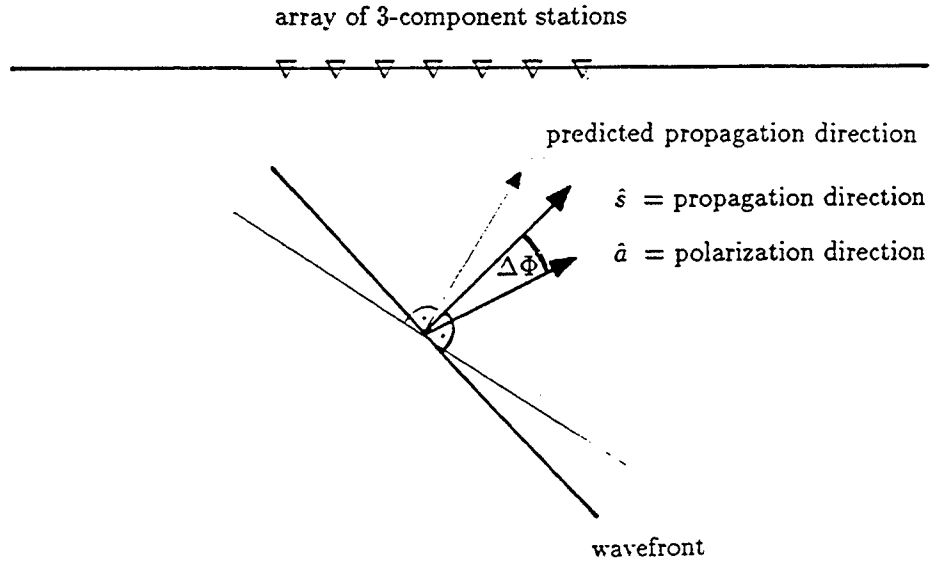
Figure 3.8: Illustration of plane P-wave propagation in the crust under the three-component receiver array. In an anisotropic medium, the polarization directions generally deviate from the propagation directions. This deviation, here shown for the incidence angle $\delta\Phi$, is used to infer effective crustal anisotropy. Note that the propagation direction typically deviates from the predicted propagation direction, due to source mislocation and distant heterogeneity. With observations of polarization and propagation directions distant effects can be excluded. Local disturbances of the wavefront are downweighted by averaging over all three-component stations.

The Dry Crack Model (Lower Hemisphere Projections)

Deviation of Polarization from Propagation Directions

5.667
5.493
5.320
5.146
4.973
4.800
4.626
4.453
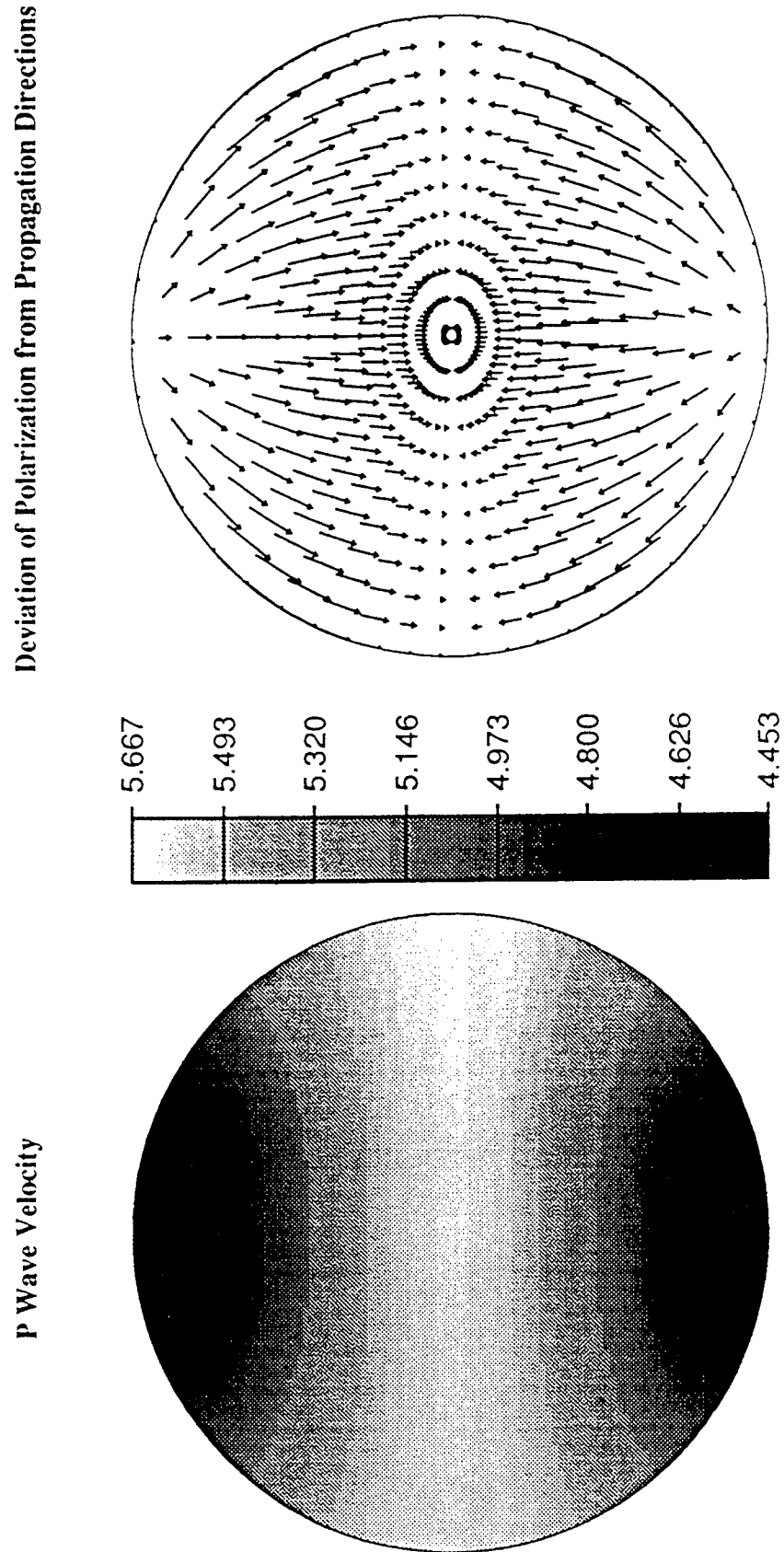
P Wave Velocity

Figure 3.9: Lower hemisphere representation of P-wave velocity and polarization anomalies for $(\eta, \tau) = (1.43, 2.13)$ corresponding to the cry-crack model HCD1 of Crampin (1984).

The Saturated Crack Model (Lower Hemisphere Projections)

Deviation of Polarization from Propagation Directions

P Wave Velocity

5.800
5.771
5.742
5.713
5.685
5.656
5.627
5.598
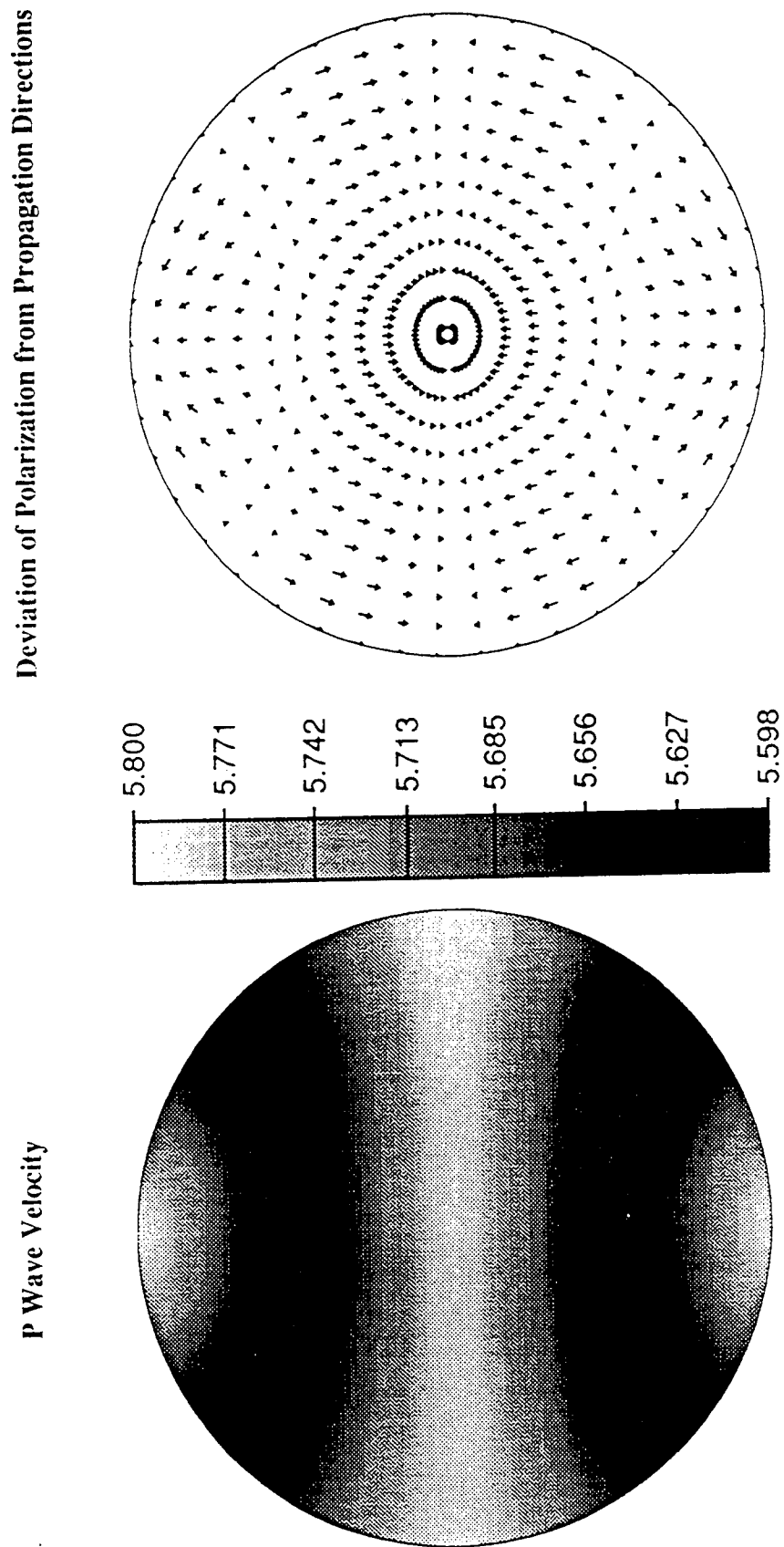
Figure 3.10: Lower hemisphere representation of P-wave velocity and polarization anomalies for $(\eta, \tau) = (0.82, 1.00)$ corresponding to the saturated-crack model HCS1 of Crampin (1984).
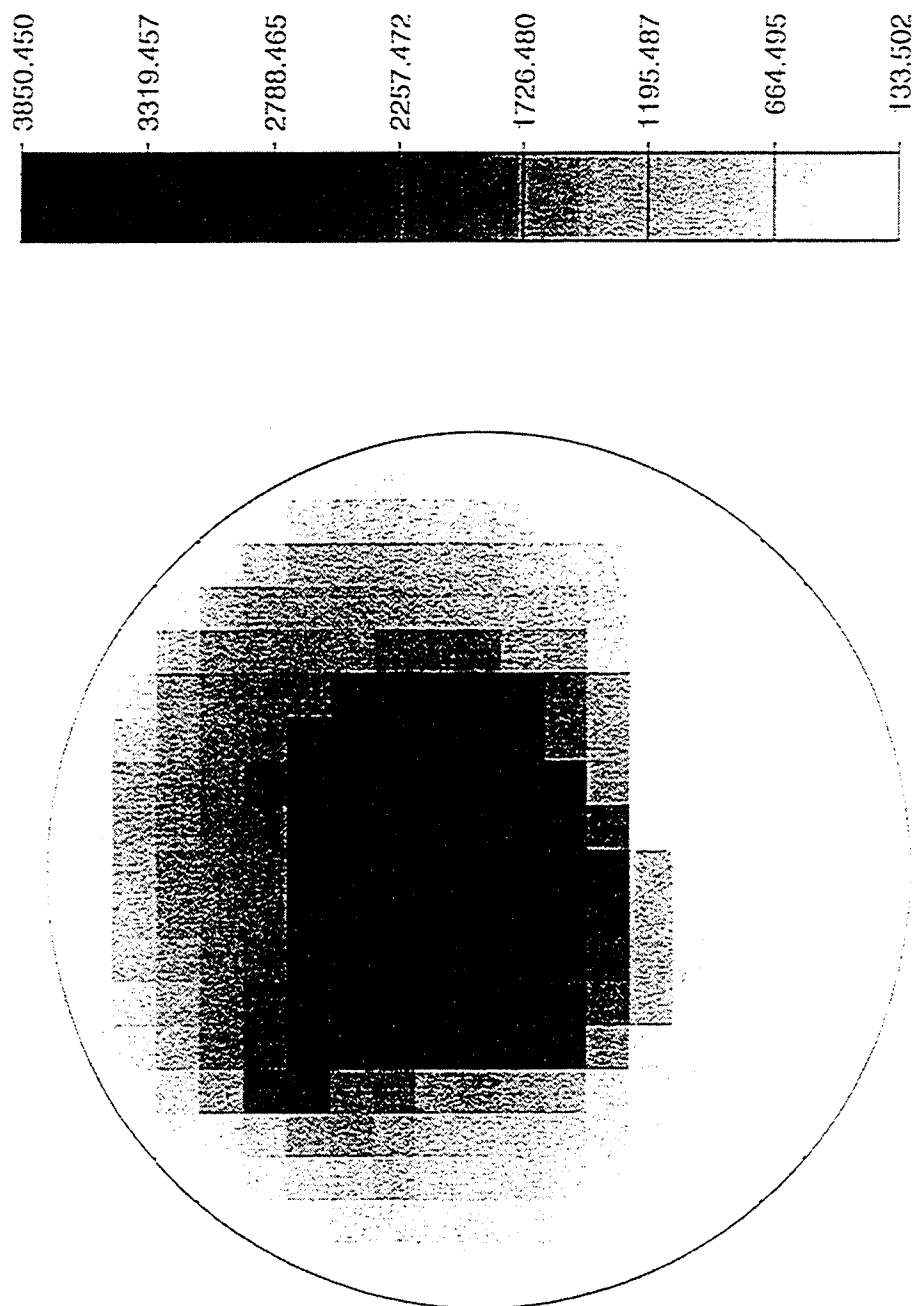
Figure 3.11: Fitting of the dry-crack model. Misfit on the sphere (23) is shown in degree^2, depending on the symmetry axis orientation. Smaller misfits are found near for axes located near the horizontal plane. This dry-crack model doesn't improve the misfit and hence can't explain the data.

Misfit depending on Symetry Axis Orientation
Theta=208.0 Phi=36.0 Eta=0.82 Tau=1.0 S=40.9453
(lower hemisphere projection)

a)
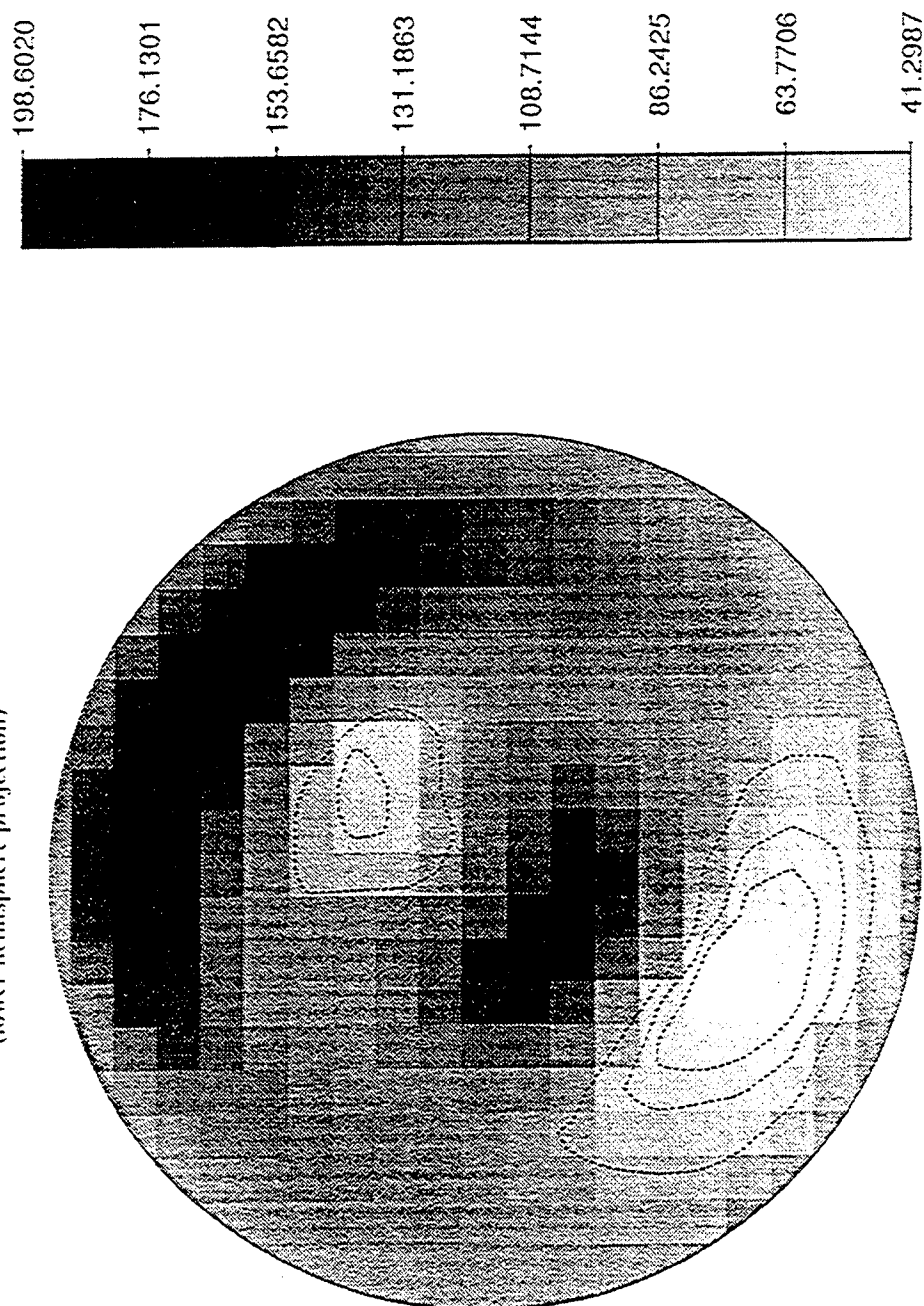
Figure 3.12: Fitting of the saturated-crack model: a) misfit in degree^2 depending on symetry axis orientation from 0°to 90°incidence, b) best-fitting model shown in a partial lower hemisphere display (0°to 55°incidence). The symmetry axis has strike 208° and dip 36° to the South. The lowest contour line gives the critical level. Polarization deviations are given for 0°, 10°,..., 50°incidence.

The Optimum Saturated Crack Model

b)

P Wave Velocity
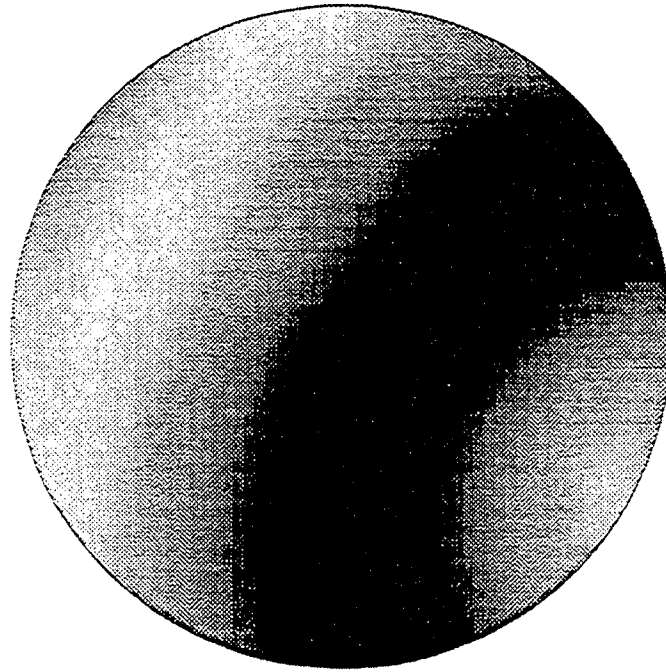
Deviation of Polarization from Propagation Directions

5.799
5.771
5.742
5.714
5.685
5.657
5.629
5.600
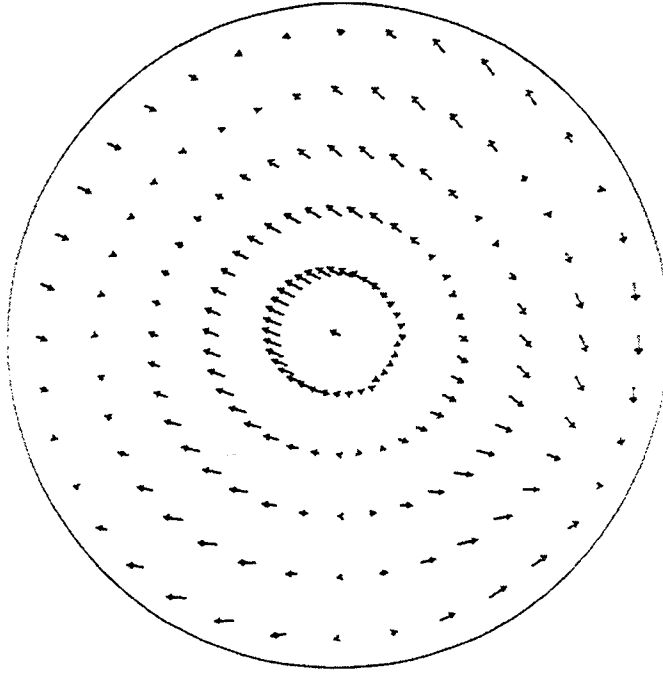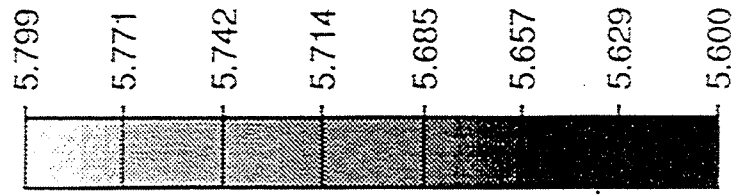
Misfit depending on Symetry Axis Orientation

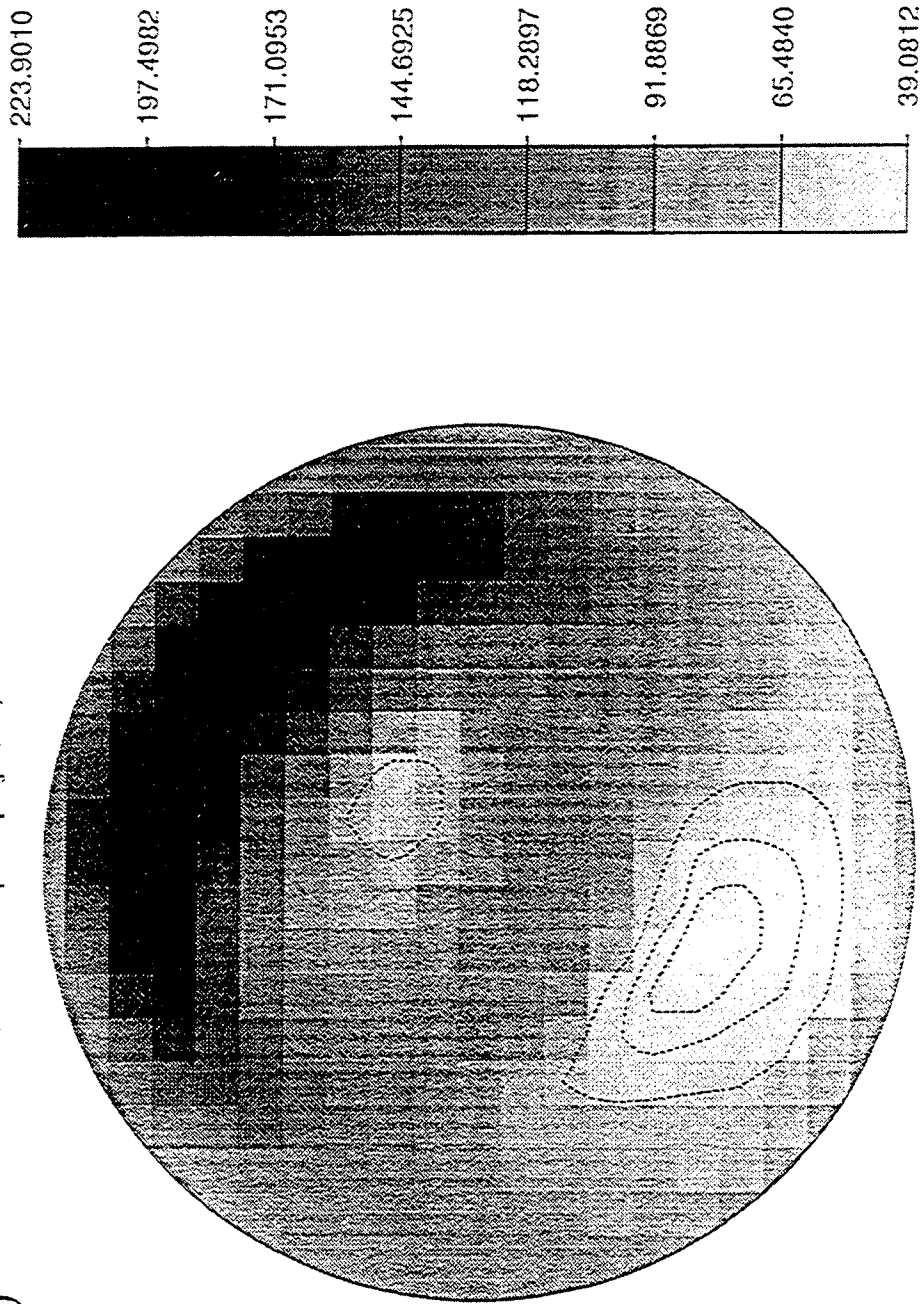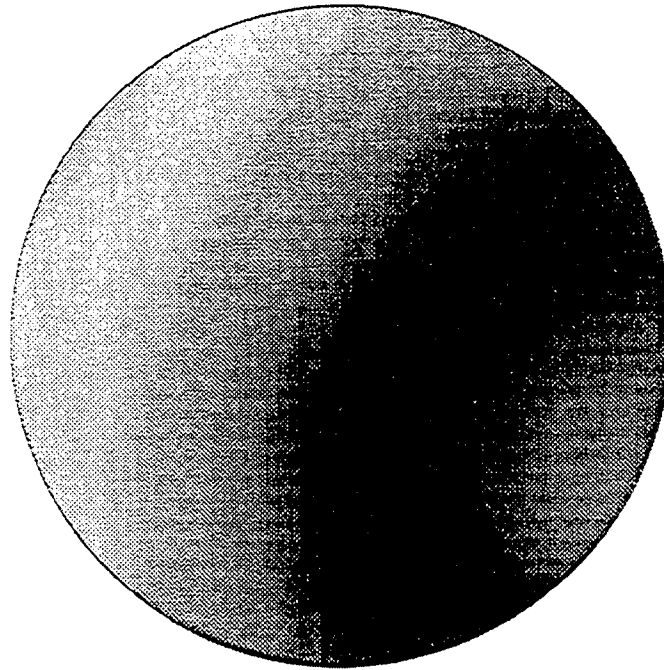Theta=203.3 Phi=41.05 Eta=0.887 Tau=1.09 S=38.8202

(lower hemisphere projection)

223.9010

197.4982

171.0953

144.6925

118.2897

91.8869

65.4840

39.0812

a)

Figure 3.13: Result of the general nonlinear search: a) misfit (0°to 90°incidence), b) optimum model in the partial lower hemisphere display (0°to 55°). With the symetry axis at 203.3°and 41.05°, the (high-velocity) symmetry plane has strike of about 113° and dips with about 58° to the North. The optimum set of parameters is $\eta = 0.887$ and $\tau = 1.09$.
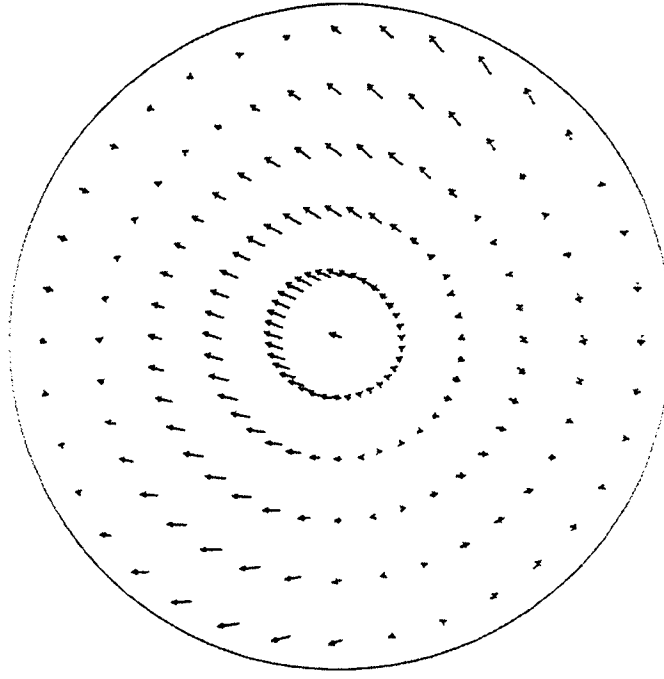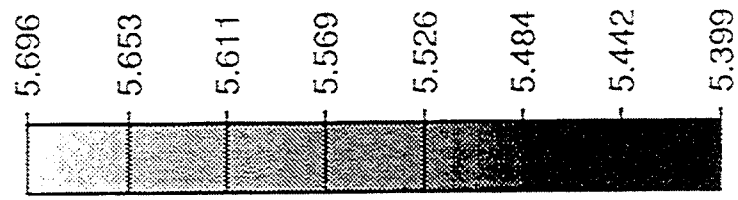
Optimum Model

Deviation of Polarization from Propagation Directions

5.696
5.653
5.611
5.569
5.526
5.484
5.442
5.399

P Wave Velocity

b)

Misfit depending on Eta and Tau

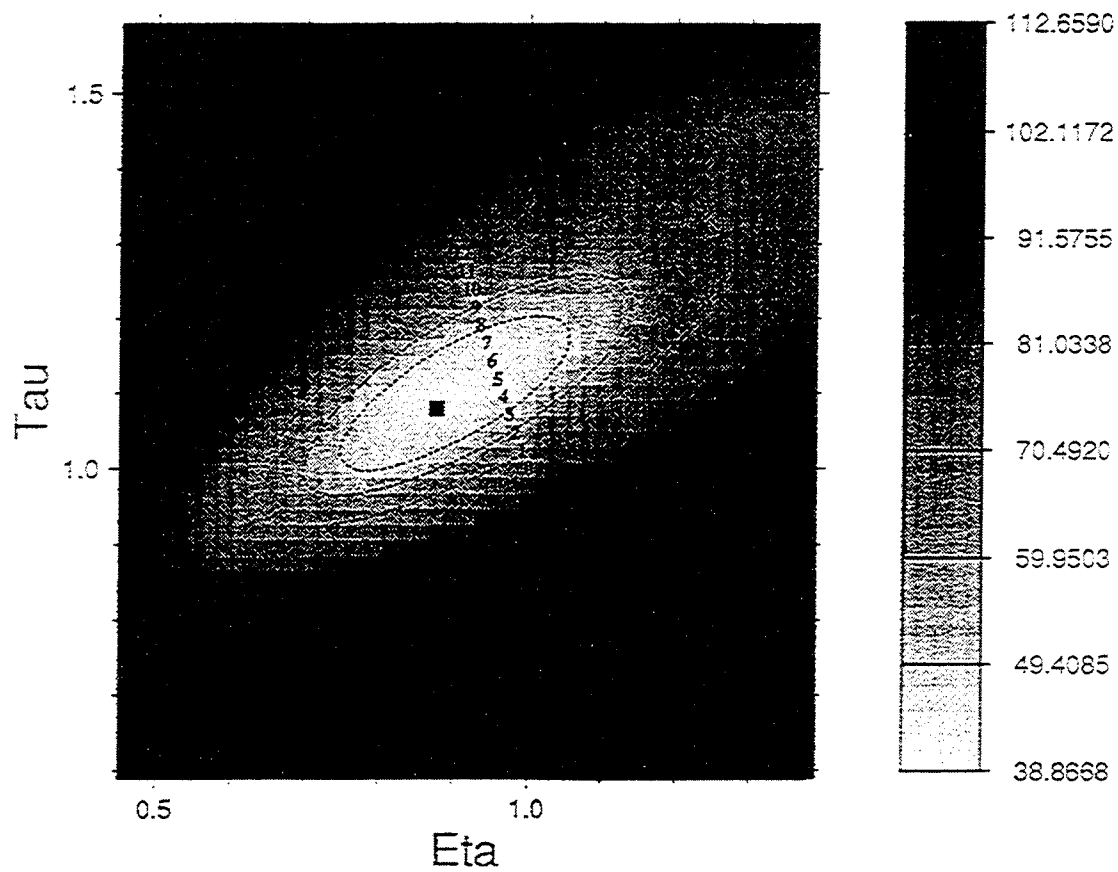Theta=203.300 Phi=41.0500 eta=0.887000 tau=1.09000 S=38.8202

Figure 3.14: Misfit around the optimum model (black square) keeping the orientation fixed. The lowest contour line shows the confidence region around the best fitting model. Numbers 0 to 13 refer to percentages of mica content in a gneiss model (see text).

Shear-Wave Velocities for the Optimum Model

qSR Wave Velocity

3.288
3.238
3.189
3.139
3.089
3.039
2.989
2.940

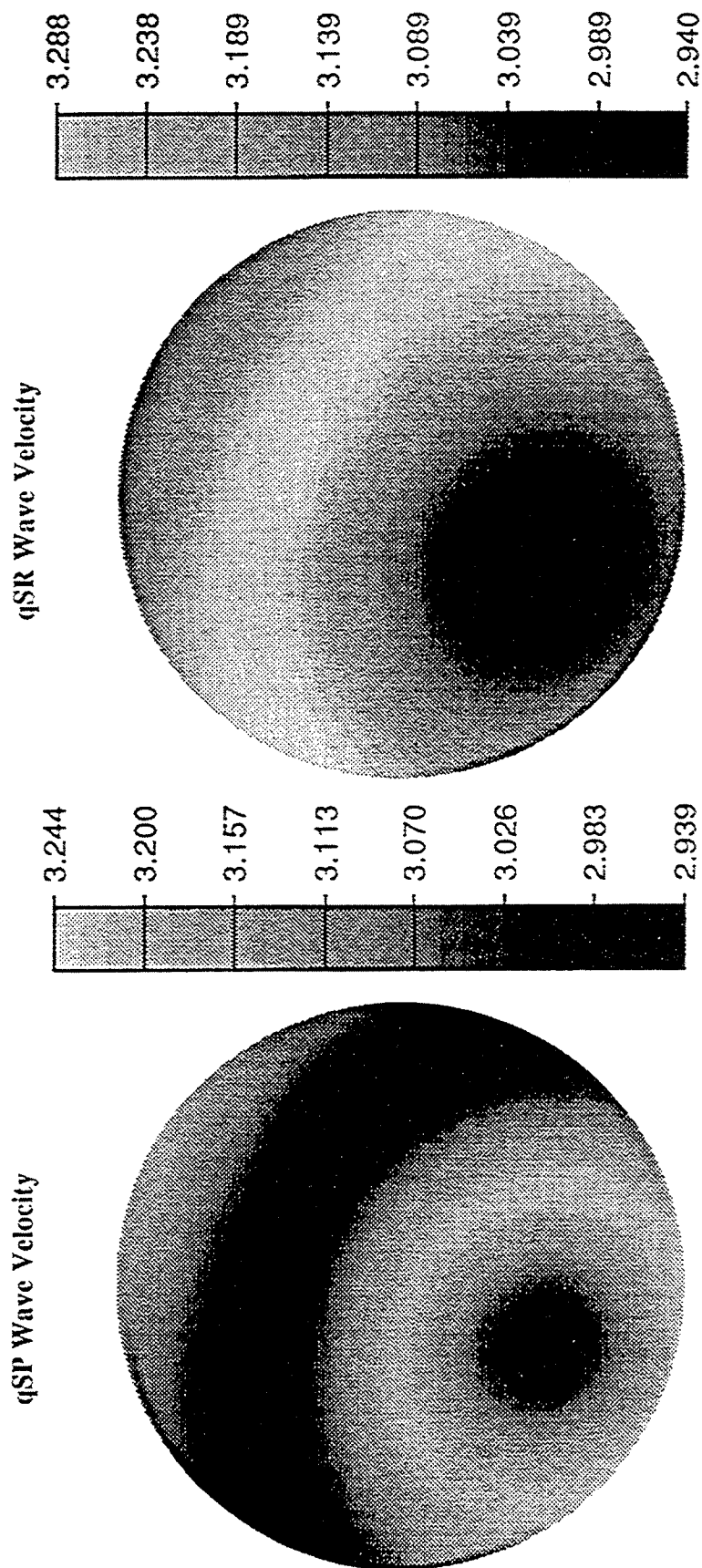qSP Wave Velocity

3.244
3.200
3.157
3.113
3.070
3.026
2.983
2.939

Figure 3.15: Prediction of shear wave velocities for the optimum model on the full lower hemisphere (0° to 90°). qSP is polarized parallel to the symetry plane and qSR perpendicular.

Prof. Thomas Ahrens
Seismological Lab, 252-21
Division of Geological & Planetary Sciences
California Institute of Technology
Pasadena, CA 91125

Prof. Keiiti Aki
Center for Earth Sciences
University of Southern California
University Park
Los Angeles, CA 90089-0741

Prof. Shelton Alexander
Geosciences Department
403 Deike Building
The Pennsylvania State University
University Park, PA 16802

Dr. Thomas C. Bache, Jr.
Science Applications Int'l Corp.
10260 Campus Point Drive
San Diego, CA 92121 (2 copies)

Prof. Muawia Barazangi
Cornell University
Institute for the Study of the Continent
3126 SNEE Hall
Ithaca, NY 14853

Dr. Douglas R. Baumgardt
ENSCO, Inc
5400 Port Royal Road
Springfield, VA 22151-2388

Dr. T.J. Bennett
S-CUBED
A Division of Maxwell Laboratories
11800 Sunrise Valley Drive, Suite 1212
Reston, VA 22091

Dr. Robert Blandford
AFTAC/TT, Center for Seismic Studies
1300 North 17th Street
Suite 1450
Arlington, VA 22209-2308

Dr. Steven Bratt
ARPA/NMRO
3701 North Fairfax Drive
Arlington, VA 22203-1714

Dale Breding
U.S. Department of Energy
Recipient, IS-20, GA-033
Office of Arms Control
Washington, DC 20585

Dr. Jerry Carter
Center for Seismic Studies
1300 North 17th Street
Suite 1450
Arlington, VA 22209-2308

Mr Robert Cockerham
Arms Control & Disarmament Agency
320 21st Street North West
Room 5741
Washington, DC 20451,

Dr. Zoltan Der
ENSCO, Inc.
5400 Port Royal Road
Springfield, VA 22151-2388

Dr. Stanley K. Dickinson
AFOSR/NM
110 Duncan Avenue
Suite B115
Bolling AFB, DC

Dr Petr Firbas
Institute of Physics of the Earth
Masaryk University Brno
Jecna 29a
612 46 Brno, Czech Republic

Dr. Mark D. Fisk
Mission Research Corporation
735 State Street
P.O. Drawer 719
Santa Barbara, CA 93102

Dr. Cliff Frolich
Institute of Geophysics
8701 North Mopac
Austin, TX 78759

Dr. Holly Given
IGPP, A-025
Scripps Institute of Oceanography
University of California, San Diego
La Jolla, CA 92093

Dr. Jeffrey W. Given
SAIC
10260 Campus Point Drive
San Diego, CA 92121

Dr. Dale Glover
Defense Intelligence Agency
ATTN: ODT-1B
Washington, DC 20301

1

Dr. Keith L. McLaughlin
S-CUBED
A Division of Maxwell Laboratory
P.O. Box 1620
La Jolla, CA 92038-1620

Prof. Bernard Minster
IGPP, A-025
Scripps Institute of Oceanography
University of California, San Diego
La Jolla, CA 92093

Prof. Brian J. Mitchell
Department of Earth & Atmospheric Sciences
St. Louis University
St. Louis, MO 63156

Mr. Jack Murphy
S-CUBED
A Division of Maxwell Laboratory
11800 Sunrise Valley Drive, Suite 1212
Reston, VA 22091 (2 Copies)

Dr. Keith K. Nakanishi
Lawrence Livermore National Laboratory
L-025
P.O. Box 808
Livermore, CA 94550

Prof. John A. Orcutt
IGPP, A-025
Scripps Institute of Oceanography
University of California, San Diego
La Jolla, CA 92093

Dr. Howard Patton
Lawrence Livermore National Laboratory
L-025
P.O. Box 808
Livermore, CA 94550

Dr. Frank Pilotte
HQ AFTAC/TT
1030 South Highway A1A
Patrick AFB, FL 32925-3002

Dr. Jay J. Pulli
Radix Systems, Inc.
201 Perry Parkway
Gaithersburg, MD 20877

Prof. Paul G. Richards
Lamont-Doherty Earth Observatory
 of Columbia University
Palisades, NY 10964

Mr. Wilmer Rivers
Multimax Inc.
1441 McCormick Drive
Landover, MD 20785

Dr. Alan S. Ryall, Jr.
Lawrence Livermore National Laboratory
L-025
P.O. Box 808
Livermore, CA 94550

Dr.Chandan K. Saikia
Woodward Clyde- Consultants
566 El Dorado Street
Pasadena, CA 91101

Mr. Dogan Seber
Cornell University
Inst. for the Study of the Continent
3130 SNEE Hall
Ithaca, NY 14853-1504

Secretary of the Air Force
(SAFRD)
Washington, DC 20330

Office of the Secretary of Defense
DDR&E
Washington, DC 20330

Thomas J. Sereno, Jr.
Science Application Int'l Corp.
10260 Campus Point Drive
San Diego, CA 92121

Dr. Michael Shore
Defense Nuclear Agency/SPSS
6801 Telegraph Road
Alexandria, VA 22310

Prof. David G. Simpson
IRIS, Inc.
1616 North Fort Myer Drive
Suite 1050
Arlington, VA 22209

Dr. Jeffrey Stevens
S-CUBED
A Division of Maxwell Laboratory
P.O. Box 1620
La Jolla, CA 92038-1620

Prof. Brian Stump
Los Alamos National Laboratory
EES-3
Mail Stop C-335
Los Alamos, NM 87545

Prof. Tuncay Taymaz
Istanbul Technical University
Dept. of Geophysical Engineering
Mining Faculty
Maslak-80626, Istanbul Turkey

Prof. M. Nafi Toksoz
Earth Resources Lab
Massachusetts Institute of Technology
42 Carleton Street
Cambridge, MA 02142

Dr. Larry Turnbull
CIA-OSWR/NED
Washington, DC 20505

Dr. Karl Veith
EG&G
5211 Auth Road
Suite 240
Suitland, MD 20746

Prof. Terry C. Wallace
Department of Geosciences
Building #77
University of Arizona
Tuscon, AZ 85721

Dr. William Wortman
Mission Research Corporation
8560 Cinderbed Road
Suite 700
Newington, VA 22122

ARPA, OASB/Library
3701 North Fairfax Drive
Arlington, VA 22203-1714

HQ DNA
ATTN: Technical Library
Washington, DC 20305

Defense Technical Information Center
Cameron Station
Alexandria, VA 22314 (2 Copies)

TACTEC
Battelle Memorial Institute
505 King Avenue
Columbus, OH 43201 (Final Report)

Phillips Laboratory
ATTN: GPE
29 Randolph Road
Hanscom AFB, MA 01731-3010

Phillips Laboratory
ATTN: TSML
5 Wright Street
Hanscom AFB, MA 01731-3004

Phillips Laboratory
ATTN: PL/SUL
3550 Aberdeen Ave SE
Kirtland, NM 87117-5776 (2 copies)

Dr. Michel Campillo
Observatoire de Grenoble
I.R.I.G.M.-B.P. 53
38041 Grenoble, FRANCE

Dr. Kin Yip Chun
Geophysics Division
Physics Department
University of Toronto
Ontario, CANADA

Prof. Hans-Peter Harjes
Institute for Geophysic
Ruhr University/Bochum
P.O. Box 102148
4630 Bochum 1, GERMANY

Prof. Eystein Husebye
NTNF/NORSAR
P.O. Box 51
N-2007 Kjeller, NORWAY

David Jepsen
Acting Head, Nuclear Monitoring Section
Bureau of Mineral Resources
Geology and Geophysics
G.P.O. Box 378, Canberra, AUSTRALIA

Ms. Eva Johannisson
Senior Research Officer
FOA
S-172 90 Sundbyberg, SWEDEN

4

Dr. Peter Marshall
Procurement Executive
Ministry of Defense
Blacknest, Brimpton
Reading FG7-FRS, UNITED KINGDOM

Dr. Bernard Massinon, Dr. Pierre Mechler
Societe Radiomana
27 rue Claude Bernard
75005 Paris, FRANCE (2 Copies)

Dr. Svein Mykkeltveit
NTNT/NORSAR
P.O. Box 51
N-2007 Kjeller, NORWAY (3 Copies)

Dr. Jorg Schlittenhardt
Federal Institute for Geosciences & Nat'l Res.
Postfach 510153
D-30631 Hannover , GERMANY

Dr. Johannes Schweitzer
Institute of Geophysics
Ruhr University/Bochum
P.O. Box 1102148
4360 Bochum 1, GERMANY

Trust & Verify
VERTIC
Carrara House
20 Embankment Place
London WC2N 6NN, ENGLAND